Development and Comparison of Processing Routes for the Manufacture of Oxide Dispersion Strengthened Steels



Zuliang Hong

St Anne's College

University of Oxford

A thesis presented for the degree of

Doctor of Philosophy

Michaelmas Term 2017

Abstract

Ferritic oxide dispersion strengthened (ODS) steels reinforced by evenly and densely distributed Y, Ti and O enriched nano-sized precipitates (NP) have emerged as one of the most promising structural materials candidates for next generation (Generation IV) nuclear fission and future nuclear fusion concepts, since they can both withstand more intensive neutron irradiation, and maintain strength and creep properties at higher operating temperatures than current standards.

The conventional processing route for ODS steels is a two-step powder metallurgy process, consisting of mechanical alloying (MA) of an Fe based matrix and a normally nano-sized Y_2O_3 powder followed by consolidation into bulk. However, major disadvantages such as prolonged processing time, small batch size, tendency for contamination and high inherent cost of feedstock powders have prevented industrial application of the MA based route.

This thesis has explored two alternative processing routes for ODS steels. In the first approach, Y_2O_3 was replaced with Fe_3Y during MA, followed by hot isostatic pressing (HIP) consolidation. The use of Fe_3Y did not disrupt the standard MA process for powders, while the consolidated alloy possessed a narrower grain size distribution, higher room temperature ductility and slightly better high temperature microhardness compared with a reference alloy produced using Y_2O_3.

In the second approach, the whole MA process was replaced with melt spinning of an Fe-5Y or Fe-1Y-1Ti (wt%) alloy. Relatively uniform spatial distribution of Y and Ti was achieved in the melt spun ribbons. The process demonstrated consistent yield (> 60% by weight), fast processing time (< 10 s), good scalability (up to > 100 g feedstock material) and repeatability across equipment in three different institutes. Internal

oxidation investigations also validated the potential of forming < 20 nm Y oxides in the ribbons.

The Fe-1Y-1Ti melt spun ribbon was then pulverised and consolidated into bulk by field assisted sintering (FAST). Simultaneous internal oxidation was achieved with the addition of nano-sized Fe_3O_4 powder, and successfully generated a high number density of sub-micron Y and/or Ti enriched oxides. Further formation of oxides took place during annealing, resulting in an approximate 20% increase in hardness at temperatures below 300 °C. However, the use of Fe_3O_4 powder reduced sinterability of the ribbons and undermined density of the alloy, which lead to mechanically incoherent prior ribbon boundaries and a significant property drop above 400 °C.

Acknowledgements

I would like to offer my gratitude to the many people who have provided assistance and support to my DPhil directly and indirectly.

First and foremost, this work would never have been possible without the contribution of my supervisors, particularly Prof Patrick Grant, for his patient guidance and crucial advices throughout my DPhil; and Dr Hongtao Zhang, for teaching me how to make steels and many useful skills in research.

I would like to acknowledge Prof Jiao Zhang and Mr Andreas Schmidt for affording me the opportunities of important collaborations that proved to be critical for my research.

I would like to thank the technicians and support scientists at Department of Materials, Gabriella, Chris, Neil, Phil, Jennifer, Gareth, Robin and Trevor for their training, help and suggestions.

I would like to thank the Oxford ODS community, past and current member of the PSG research group, Mike, Yina, Maria, Alasdair, Sarah, Edd, Atsushi, Amogh, Enzo, Dmitry, Flynn, Chaopeng, Chun, Yunqi, Qin, Sanbin, Shunli, Shikang and Lukas for many fruitful discussions, encouragement and exciting basketball games.

I would also like to extend my appreciation to my friends, particularly Yang, Chuang, Yilun, Yuchen, Weiyue, Xiaochen, Yucheng, Yeli, Yakun, Qingji and many others for an active and cheerful life here at Oxford.

Finally, I would like to offer my special thanks to my father and mother for their enduring support and many useful advices during the ups and downs over the years.

Contents

1 Introduction 1

2 Literature review 4

2.1 Introduction 4

2.2 Materials requirements 4

2.2.1 Primary radiation damage 5

2.2.2 Low activation alloying elements 8

2.2.3 Radiation damage resistance 9

2.2.4 Strengthening mechanism 11

2.3 Oxide dispersion strengthened steels 16

2.3.1 Alloying composition 17

2.3.2 Microstructure 19

2.3.3 Performance 21

2.4 Processing of oxide dispersion strengthened steels 23

2.4.1 Mechanical alloying 25

2.4.2 The formation mechanisms of Y-Ti-O enriched nano-sized particles 30

2.5 Alternative processing routes for ODS steels 31

2.5.1 Reactive mechanical alloying 32

2.5.2 Liquid metal processing 36

2.6 Research objectives 43

3 Processing 45

3.1 Introduction 45

3.2 Mechanical alloying based processing 46

3.2.1 Chemical composition 46

3.2.2 Raw materials 48

3.2.3 Mechanical alloying 49

3.2.4 Hot isostatic pressing 51

3.3 Melt spinning based processing 52

3.3.1 Chemical composition 52

3.3.2 Raw materials and master alloy production 54

3.3.3 Melt spinning 55

3.3.4 Internal oxidation 58

3.3.5 Ribbon pulverization 59

3.3.6 Field assisted sintering 60

4 Characterisation 64

4.1 Scanning electron microscopy 64

4.1.1 Imaging 64

4.1.2 Energy dispersive X-ray spectroscopy 65

4.1.3 Electron backscatter diffraction 65

4.1.4 Electron probe microanalysis 66

4.2 Transmission electron microscopy 67

4.3 X-ray diffraction 69

4.4 Powder size distribution 70

4.5 Vickers microhardness 70

4.6 Four-point bending 71

Contents

5 Mechanical alloying based processing 74

5.1 Introduction 74

5.2 Mechanical alloyed powder 75

5.2.1 Particle size distribution and morphology 75

5.2.2 Microhardness 78

5.2.3 XRD 79

5.2.4 TEM 80

5.2.5 EPMA 82

5.3 Consolidation 92

5.3.1 XRD 92

5.3.2 EBSD 93

5.3.3 Four-point bending 98

5.3.4 Hot microhardness 99

5.4 Summary 100

6 Melt spun ribbon processing 103

6.1 Introduction 103

6.2 MS01 (Fe-5Y) ribbon 105

6.2.1 Melt spun ribbons 105

6.2.2 Internal oxidation 106

6.3 MS02 (Fe-1Y-1Ti) ribbon 113

6.3.1 Master alloy 113

6.3.2 Melt spun ribbon 114

6.3.3 Vacuum annealing 115

6.4 MS03 (Fe-1Y-1Ti) ribbon 118
6.4.1 Master alloy 119
6.4.2 Melt spun ribbon 120
6.5 MS04 (Fe-1Y-1Ti) ribbon 122
6.5.1 Master alloy 123
6.5.2 Melt spun ribbon 124
6.6 Summary 126
7 Bulk alloy production 127
7.1 Introduction 127
7.2 Alloy BA01 127
7.3 Alloy BA02 132
7.4 Alloy BA03 137
7.5 Hot microhardness 142
7.6 Summary 144
8 Conclusion and future work 145
8.1 Mechanical alloying based processing 145
8.2 Melt spun ribbon production 146
8.3 Bulk alloy production from melt spun ribbon 147
8.4 Future work 148
9 Bibliography 150

Common symbols and abbreviations

APT – atom probe tomography

bcc – body centred cubic

BF – bright field

BSE – backscattered electron

DBTT – ductile brittle transition temperature

DF – dark field

dpa – displacement per atom

EBSD – electron backscatter diffraction

EDX – energy dispersive X-ray spectroscopy

EPMA – electron probe microanalysis

FAST – field assisted sintering technique

FIB – focused ion beam

fcc – face centred cubic

HAADF – high angle angular dark field

HIP – hot isostatic pressing

HRTEM – high resolution transmission electron microscopy

IPF – inverse pole figure

MA – mechanical alloying

NP – nano-sized particle

ODS – oxide dispersion strengthened

PRA – primary recoiling atom

SE – secondary electron

SEM – scanning electron microscopy

SIA – self-interstitial atom

SPS – spark plasma sintering

STEM – scanning transmission electron microscopy

TEM – transmission electron microscopy

$\mathbf{T_M}$ – thermal melting temperature

WDX – wavelength dispersive X-ray spectroscopy

XRD – X-ray diffraction

1 Introduction

Nuclear fission power has been playing an indispensable role in global electricity generation since its commercial application from the mid-1950s and is characterised by its high capacity factor, energy density and low carbon emission [1,2]. More than 450 reactors in over 30 countries currently generate about 10% of the world's electricity supply [3]. Although the tsunami-induced accident at Fukushima Daiichi, Japan in 2011 has raised public concerns and uncertainties around nuclear power, it is believed that nuclear will continue to be a crucial power source in the future because of 1) steadily increasing demand on base load power generation; 2) pressing needs for reduction in carbon emission; and 3) government considerations on energy security [1,2,4]. As shown in Figure 1, the share of nuclear fission power in global electricity generation is projected to remain stable at the current fraction, with its total capacity doubling from 2012 to 2040 [1].

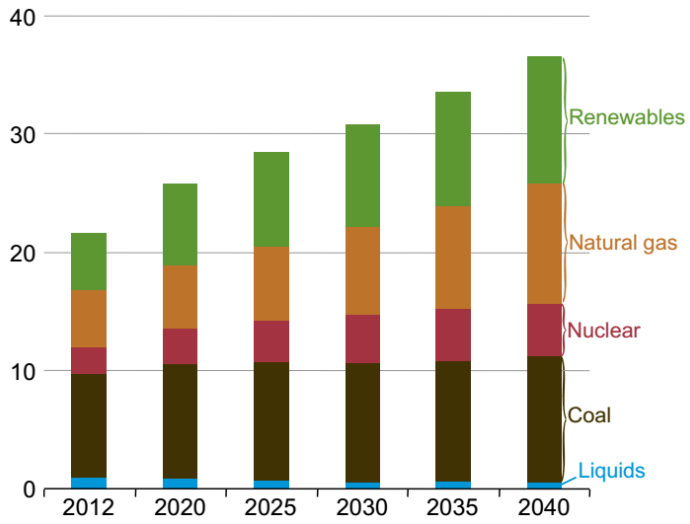

Figure 1: World net electricity generation by fuel type, 2012 – 2040 (trillion kWh) [1]

The development of more efficient yet safer next generation (Generation IV) nuclear fission concepts, as well as the progressive advances in research of nuclear fusion power secures the important position of nuclear power in the future global energy portfolio 3. However, these developments have also brought up complex new

challenges for the structural materials that are applied in critical components such as the pressure vessel in fission reactors and the first blanket wall in fusion plants [2,4–6]. They are supposed to withstand more intensive neutron irradiation, while maintaining strength and creep resistance at higher operating temperatures than current standards [2,4–6].

Ferritic oxide dispersion strengthened (ODS) steels reinforced by evenly and densely distributed Y, Ti and O enriched nano-sized precipitates have emerged as one of the most promising materials candidates for such applications [7]. The widely practiced conventional processing route for ODS steels is a two-step powder metallurgy process, consisting of mechanical alloying (MA) of an Fe based matrix and a normally nano-sized Y_2O_3 powder followed by consolidation into bulk materials [7–12]. However, major disadvantages such as prolonged processing time, small batch size, tendency for contamination associated with high specific area of the powder, high inherent cost of feedstock powders, *etc.* have prevented technological implementation of the MA based route at any useful scale [6,13–18].

This thesis aims to explore two alternative processing routes for the manufacture of ODS steels, which are (1) an ‘evolutionary’ approach that replaces Y_2O_3 with an Fe-Y intermetallic during MA, followed by conventional consolidation into bulk; and (2) a ‘revolutionary’ approach that replaces the whole MA step with melt spinning of a dilute Fe-Y/Fe-Y-Ti intermetallic, followed by simultaneous consolidation into bulk and internal oxidation of Y and/or Ti into oxides. Any benefits in mechanical properties and/or production throughput of the two alternative approaches are then assessed with any property compromises.

The structure of the thesis is as follows:

Chapter 2 reviews the literature relating to materials requirements for future nuclear applications, characteristics of ODS steels, their processing route and potential alternative manufacturing strategies.

Chapter 3 describes the chemical composition and nature of raw materials, key equipment and their operating parameters for the manufacture and heat treatment of model alloys produced using the two alternative processing routes.

Chapter 4 describes characterisation techniques and equipment used to analyse the model alloys in their powder, ribbon and bulk forms.

Chapter 5 presents a comparative investigation between an Fe-Y intermetallic containing model alloy produced using the 'evolutionary' approach and a conventional Y_2O_3 containing alloy, both in their powder and consolidated states.

Chapter 6 presents results of melt spun ribbon production, as the first step of the 'revolutionary' approach, using dilute Fe-Y and Fe-Y-Ti intermetallics, and internal oxidation investigation of the ribbons.

Chapter 7 presents results of simultaneous consolidation and internal oxidation of a Fe-Y-Ti melt spun ribbon, as the second step of the 'revolutionary' approach, and microhardness investigation of the alloys.

Chapter 8 summarises the key results and insights, along with suggestions for future work.

2 Literature review

2.1 Introduction

This chapter reviews the literature relating to materials requirements for future nuclear applications, characteristics of ODS steels, their conventional processing route and potential alternative manufacturing strategies.

2.2 Materials requirements

The structural materials for next generation fission and fusion reactors will be subject to a new combination of property challenges due to the aggressive operating conditions. For example, the structural material for the first blanket wall of a future fusion reactor must withstand irradiation of high energy neutrons (14.1 MeV) produced by the deuterium-tritium fusion reaction, while maintaining mechanical properties under a sustained heat flux (1 – 10 MW/m) from the fusion constraining plasma [4,7,19]. Although structural materials of next generation fission reactors do not need to resist neutron flux at the same level of energy and intensity, they must still withstand highly demanding environment involving cyclic fatigue, creep fatigue and corrosion with a heat flux of about 1 MW/m [4,19].

Among the various property requirements, the most fundamental is a combination of outstanding radiation damage resistance and high temperature mechanical properties [2,4,7]. As illustrated in Figure 2.1, the structural materials for the future fusion reactors are expected to withstand operating temperatures of 300 – 1000 °C while receiving a life-time (5 – 10 years) irradiation dose of 150 – 200 displacements per atom (dpa) [7]. The operating temperatures for structural materials of some of the next generation fission reactors such as very high temperature reactor may even exceed 1000 °C, while other concepts like molten salt reactor (MSR) and sodium fast reactor (SFR) require irradiation damage resistance at a dose of approximately 150 dpa over a life span of about 40 years [2,7].

Overall, these operating conditions are more demanding than current generation fission reactors, which has therefore stimulated investigations to develop a new generation of suitable structural materials.

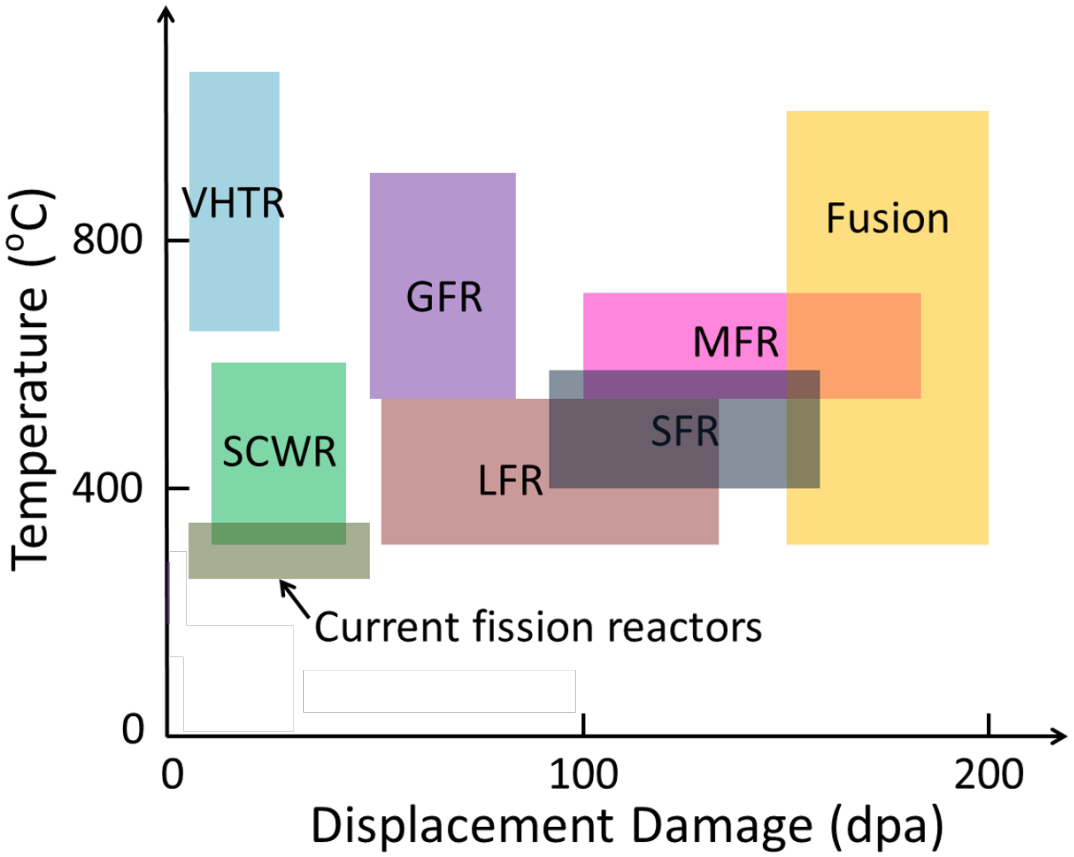

Figure 2.1: Overview of operating temperatures and life time displacement damage dose for structural materials in current and proposed fission and fusion reactors. The proposed next generation fission systems are very high temperature reactor (VHTR), super critical water reactor (SCWR), lead fast reactor (LFR), gas fast reactor (GFR), sodium fast reactor (SFR), and molten salt reactor (MSR) [4].

2.2.1 Primary radiation damage

Structural materials are generally damaged by irradiation of neutrons in two major ways: generation of primary recoiling atoms (PRAs) and transmutation products [7,20].

2.2.1.1 Primary recoiling atoms

The PRA is produced by a collision between a neutron (above several hundred keV) and the nucleus of an atom from the structural material. The energised PRA is

displaced from its lattice site, leaving behind a vacancy, while creating a self-interstitial defect when the atom eventually rests in the lattice [7,20]. The average number of times an atom is displaced from its normal lattice site by the atomic collision processes is referred to as displacement per atom (dpa), which is the unit to measure irradiation damage in materials [20].

Before dissipation of the acquired kinetic energy, the PRAs may have obtained sufficient energy to displace other atoms, and in turn generate a branching cascade of recoiling atoms, which appears together with a high concentration of vacancy and SIA point defects [20]. Although vacancies and self-interstitial atoms (SIAs) undergo dynamic recombination and annihilation, accumulation of defects happens at high neutron flux, energy and irradiation time, which causes microstructural change and may degrade the properties of structural materials [19,21,22].

One of the property degradations caused by PRAs is radiation hardening and embrittlement. This appears at relatively low temperatures (< 0.4 T_M where T_M refers to the melting temperature in Kelvin) and low doses (0.001 to 0.1 dpa) [4,23]. The loss of ductility and fracture toughness is mainly due to strong hindrance of dislocation movement by concentrated vacancy and SIA defects formed within the cascades, which reduces at increased temperatures due to enhanced diffusion [23].

At intermediate temperatures (0.3 – 0.6 T_M) and higher irradiation doses (> 10 dpa), radiation induced segregation and precipitation can lead to localized corrosion and mechanical property degradation such as grain boundary embrittlement [4,24], while accumulation of vacancies on preferential sites such as grain boundaries can lead to formation and growth of voids [4,25], which is especially detrimental since it is very difficult to accommodate volumetric expansion of structural materials in excess of 5% in any engineering design [26]. Similar reasons also cause unacceptable irradiation creep at temperatures < 0.45 T_M and irradiation doses > 10 dpa [25].

2.2.1.2 Transmutations

Apart from the PRA induced defects within the lattice structure, the high energy neutrons also causes transmutation of some alloying elements, which can create He and H via (neutron, α-particle) and (neutron, proton) type reactions, respectively [19,20].

Although both H and He are generally insoluble in a metallic matrix, H is relatively easy to diffuse out of the material because of its small physical size and high mobility, especially at high service temperatures. On the other hand, the larger He is more likely to be trapped at lattice vacancies [20]. At high temperatures (> 0.5 T_M) and irradiation doses (> 10 dpa), the entrapped He can migrate and accumulate at preferential sites such as the grain boundaries, forming cavities, and subsequently reducing ductility and fracture toughness of the material via an increased tendency to intergranular fracture [7,20]. This He induced embrittlement typically appears when the He concentration within the material is above 10 – 100 atomic ppm, and the effects may be exacerbated with increasing temperature and applied stress [4]. Since He concentration has been estimated to be 3 – 10 atomic ppm for the next generation fast neutron fission reactors and a substantial 1500 atomic ppm for the future fusion reactors, transmutation damage is undoubtedly a serious threat to viable structural materials [22,27].

The major radiation damage threats discussed above are summarised in Table 2.1.

Table 2.1: Summary of major radiation damage threats to structural materials [4]

Radiation damage threats	Temperature (T_M)	Irradiation dose (dpa)
Radiation embrittlement	< 0.4	> 0.1
Radiation induced precipitation	0.3 – 0.6	> 10
Irradiation creep	< 0.45	> 10
Volumetric swelling	0.3 - 0.6	> 10
He embrittlement	> 0.5	> 10

2.2.2 Low activation alloying elements

As discussed in section 2.2.1.2, energetic neutrons can induce transmutation reactions. In addition to the generation of H and He, the reactions may also produce different isotopes of the alloying elements, some of which may be radioactive. Although fusion is often portrayed as a 'safe' nuclear power with low levels of radiation, it seems likely that fusion reactors will nonetheless become highly activated given the current materials available and predicted duty cycle. To minimise long-term environmental impact, a key materials requirement is therefore the use of low activation alloying elements that might limit generation of radioactive isotopes with extensive half-life decay period [4,19].

Table 2.2 summarises the classification of induced activity of some of the common alloying elements where steels are to be considered, suggesting only very limited use of high activation elements including N, Al and Ni, and restriction of those elements with lower induced activity than the moderate activation of Fe [27,28]. In order to maintain performance, strategies such as strict control on N composition, and replacement of some of the common alloying constituents Mo, Nb and Ni by W, V and Mn have been adopted [7,27].

Combining the low activation prerequisite with other property requirements, three major contenders have emerged for future fission and fusion structural materials, which are ferritic/martensitic steels, refractory (W and V) alloys and SiC/SiC composites [4,7,19]. Among them, the ferritic/martensitic low activation steels have been considered the most developed for large scale primary structures, and will be discussed in more detail in this review [4,29].

Table 2.2: Classification of induced activity of elements based on half-life decay [29]

Classification of induced activity	Common Alloying elements
Very low activation (decay in 2 weeks)	Li, Be, B, C, O, Mg, Si, P, S
Low activation (decay in 5 years)	Ti, V, Cr, Zr, W, Pb, Y
Moderate activation (decay in 30 years)	Mn, Fe, Zn, Hf
High activation (decay in more than 100 years)	N, Al, Ni, Cu, Nb, Mo, Sn

2.2.3 Radiation damage resistance

Since little can be done to avoid the generation of primary radiation damage, radiation damage resistance of structural materials is generally achieved by promoting recombination of point defects and trying to distribute the inevitable He bubbles to a very fine, less damaging scale [4,19].

2.2.3.1 Crystal structure

Body centred cubic (bcc) alloys, including ferritic/martensitic steels, refractory vanadium and tungsten alloys generally exhibit significantly lower radiation effects, such as volumetric swelling, than face centred cubic (fcc) alloys such as austenitic steels [23,25,30].

As shown in Figure 2.2, after ion irradiation to 50 dpa at 650 °C, bubble-like cavities were evident in Type 316LN austenitic steels, while there were no obvious voids in the 9Cr2WVTa (wt%) ferritic/martensitic steel irradiated under the same conditions [30].

The reduced irradiation damage in the bcc alloys is caused by a lower dislocation bias (preference for trapping interstitial atoms than vacancies [31]) and higher diffusion rate of point defects compared with other crystal structures [20,26]. These characteristics not

only reduce the hindrance of point defect movement, but also promote the diffusion of vacancies and SIAs, which ultimately encourages their recombination and annihilation rather than accumulation in high densities that deteriorate ductility, fracture toughness and creep strength [22,30].

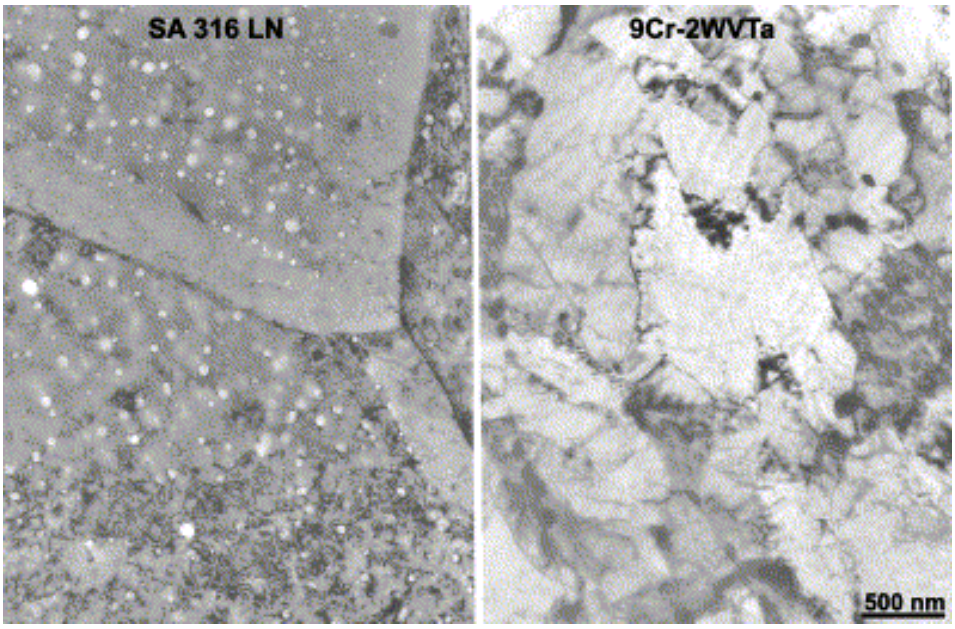

Figure 2.2: Comparison of microstructures of Type 316 LN austenitic stainless steel (left) and 9Cr2WVTa ferritic/martensitic steel (right) after ion irradiation at 650 °C to 50 dpa and 260 atomic ppm He [30].

2.2.3.2 Nano-sized particles

Another effective method to improve radiation damage resistance for structural materials is the introduction of uniformly distributed nano-sized particles (NPs) [4,19,21,32].

As shown in Figure 2.3, a high density of evenly distributed NPs within the metallic matrix provides a sink for irradiation induced vacancies and SIAs, and subsequently promotes recombination and annihilation of these point defects [4,20,26]. Also, the NPs act as nucleation sites for He, which helps trap and retain He within the grains in the form of nano-sized bubbles [4,20,26,27]. The dynamic competition between NPs and grain boundaries as preferential segregation sites for point defects and He bubbles reduces the number and size of more detrimental cavities and bubbles on grain boundaries,

and therefore enhances radiation damage resistance in terms of ductility, fracture toughness and high temperature creep strength [20].

The NP size is critical to provide appropriate radiation damage resistance. For example, a 2 – 5 nm NP strengthened ferritic steel maintained high strength (~ 1500 MPa) and good fracture toughness (~ 175 $\mathrm{MPa}\sqrt{\mathrm{m}}$) after neutron irradiation to 1.5 dpa at 300 °C, while a reference ferritic steel reinforced by 10 – 50 nm oxides suffered severe embrittlement after irradiation under the same conditions [21,33].

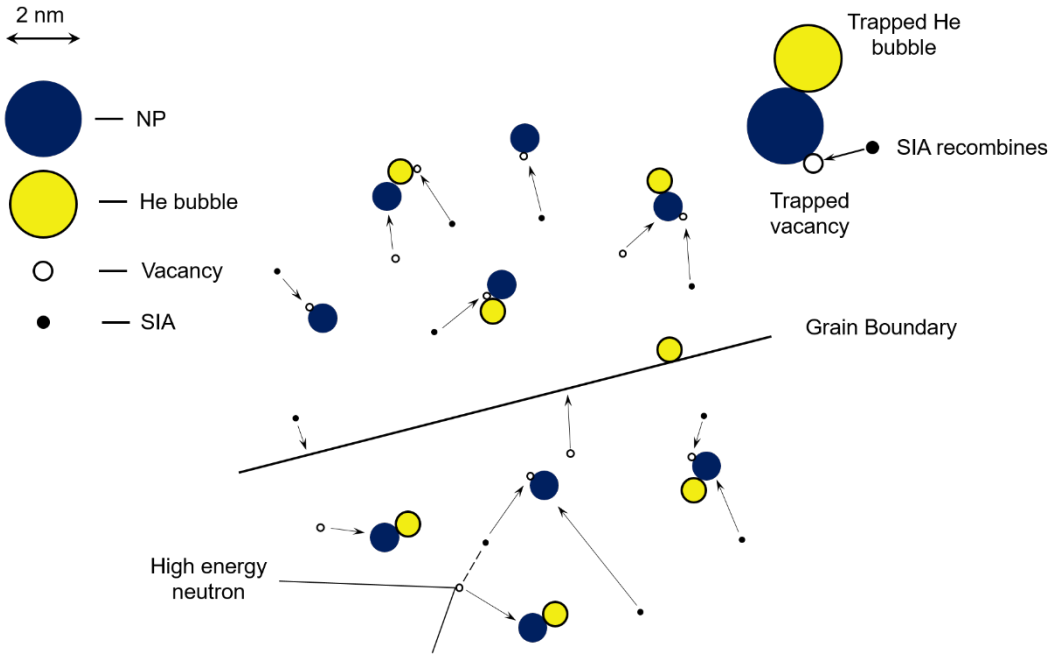

Figure 2.3: Schematic illustration showing mechanisms of radiation damage resistance provided by NPs [29].

2.2.4 Strengthening mechanism

The strengthening of metallic materials is generally achieved through various interactions with dislocations that impedes their movement. The five common strengthening mechanisms for metallic materials are summarised in Table 2.3 [34–36]. Leaving the efficiency of different dislocation interactions on one side, the effectiveness of each type of strengthening mechanism is largely dependent on operating temperature of the materials [29,37].

2 Literature review

Since the structural materials for key components of future fission and fusion reactors should operate at temperatures above ~ 0.5 T_M (melting temperature) for Fe based alloys, work hardening, grain size refinement and solid solution strengthening cannot be applied [4,7,29]. For work hardening, the increased dislocation density in the material that impedes further dislocation motion will be rapidly reduced at temperatures above ~ 0.3 T_M [37]. For solid solution strengthening, the lattice strain created by solute atoms gradually loses pinning effects on dislocation motion due to non-conservative dislocation movement at high temperatures [37]. As for the grain size refinement, the high densities of grain boundary areas will facilitate excessive thermal creep at high temperatures [37].

Although precipitation and dispersion strengthening both impede dislocation movement by 2nd phase particles, the latter one is more suitable at high temperatures, since an insoluble phase is more thermodynamically stable than a phase precipitated from a super-saturated matrix [29,37]. Dispersion strengthening particles are less prone to coarsening and over-aging at temperatures closer to the melting point, which provides more design flexibility and margin for high temperature applications.

Therefore, the dispersion strengthening mechanism has been adopted, and shown, to be the most suitable strengthening strategy for Fe based structural materials for future fission and fusion applications.

Table 2.3: Summary of strengthening mechanisms [29]

Strengthening mechanism	Maximum Effective Temperature (T_M)	Comment
Work hardening	~0.3	Dislocation – dislocation interaction
Grain size refinement	~0.3	Grain boundary – dislocation interaction
Solid solution strengthening	~0.4	Lattice strain field – dislocation interaction
Precipitation strengthening	~0.6	Metastable 2nd phase particle – dislocation interaction
Dispersion strengthening	~0.9	Insoluble 2nd phase particle – dislocation interaction

2.2.4.1 Dispersion strengthening

Depending on different types of interactions between dislocations and the insoluble 2nd phase particles, dispersion strengthening can be generally categorized into two types, strengthening by impenetrable or penetrable particles [34,36].

Figure 2.4 illustrates the strengthening provided by impenetrable, or non-shearable particles. When a dislocation line moves into an array of particles, it is impeded and forced to bend under repulsive stress provided by the particles [34,36]. Further bowing around the particles eventually results in formation of dislocation loops, as the dislocation line eventually passes by. Bowing of the dislocation line and loop formation both consume energy which results in strengthening of the material. The shear stress increase ($\Delta\tau$) required to bypass the array of particles can be estimated as:

$$\Delta\tau = \frac{Gb}{d}$$

where G is shear modulus of the material; b is the Burgers vector; and d is the inter-particle spacing [34,36]. Therefore for impenetrable particles, the strengthening effect ($\Delta\tau$)

is increased with reducing spacing between particles. In addition, the strengthening effect increases with decreasing particle size, and increasing volume fraction [34,36].

On the other hand, although less relevant for ODS steels due to the strengthening ceramic particles being generally impenetrable [38,39], the strengthening mechanism provided by penetrable, or shearable, particles is shown in Figure 2.5. When encountering the particles, the dislocation line cuts through by shear of one Burgers vector before passing through [34,36]. Since energy of the dislocation line is consumed to generate new interfaces at the sheared particles, the dislocation motion is hindered, and the material is strengthened [34,36].

$\Delta\tau$ in this case can be estimated from:

$$\Delta\tau = \frac{2r\sigma}{bd}$$

where r is particle radius; σ is interfacial energy between particle and matrix; b is Burgers vector; and d is the inter-particle spacing [34,36]. The decrease of inter-particle spacing again increases the strengthening effect. Meanwhile, the strengthening effect is improved with both increasing particle size and volume fraction [34,36].

Since an increase in particle size reduces the strengthening effect of impenetrable particle mechanism, but enhances the effect of penetrable particle mechanism, the maximum dispersion strengthening is achieved when these two mechanisms contribute similarly to the total strengthening, otherwise, the dislocation line will select the less energy depleting route [34,36]. The critical particle radius (r_{crit}) could therefore be estimated from:

$$\Delta\tau = \frac{Gb}{d} = \frac{2r_{crit}\sigma}{bd}$$

$$\Rightarrow r_{crit} = \frac{Gb^2}{2\sigma}$$

Hence, the selection of particle size, as well as volume fraction and inter-particle distance, is important in determining the effectiveness of dispersion strengthening.

Overall, based on materials requirements including low radiation induced activity, radiation damage resistance and persistence of mechanical properties at high temperatures, ferritic/martensitic steels strengthened by thermodynamically stable NPs, which are referred to as ODS steels, have emerged as the one of the most promising materials candidates for future fission and fusion applications.

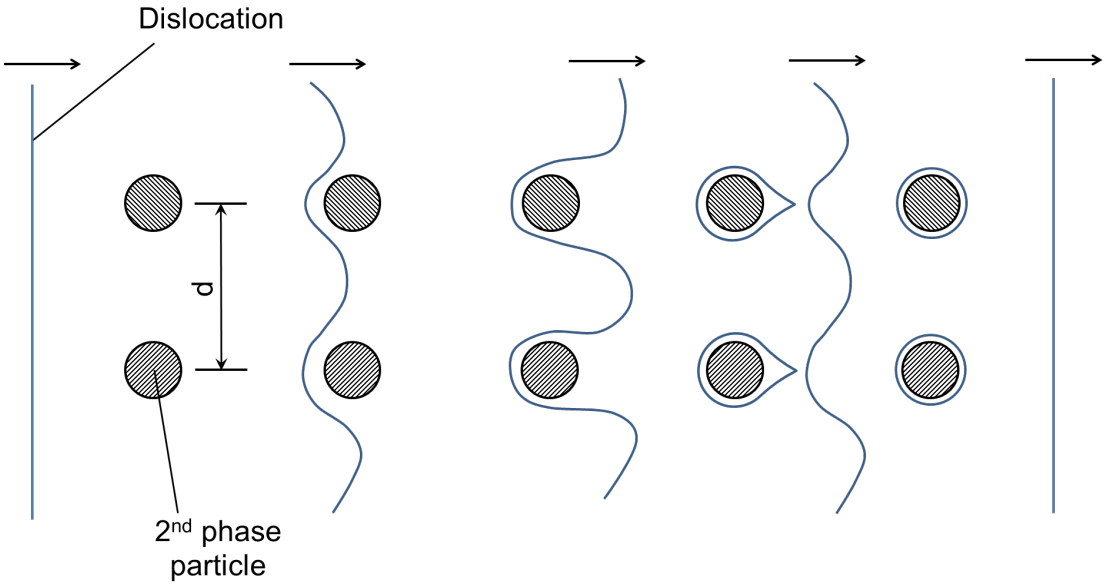

Figure 2.4: Dispersion strengthening from impenetrable particles. Inter-particle spacing is d [34].

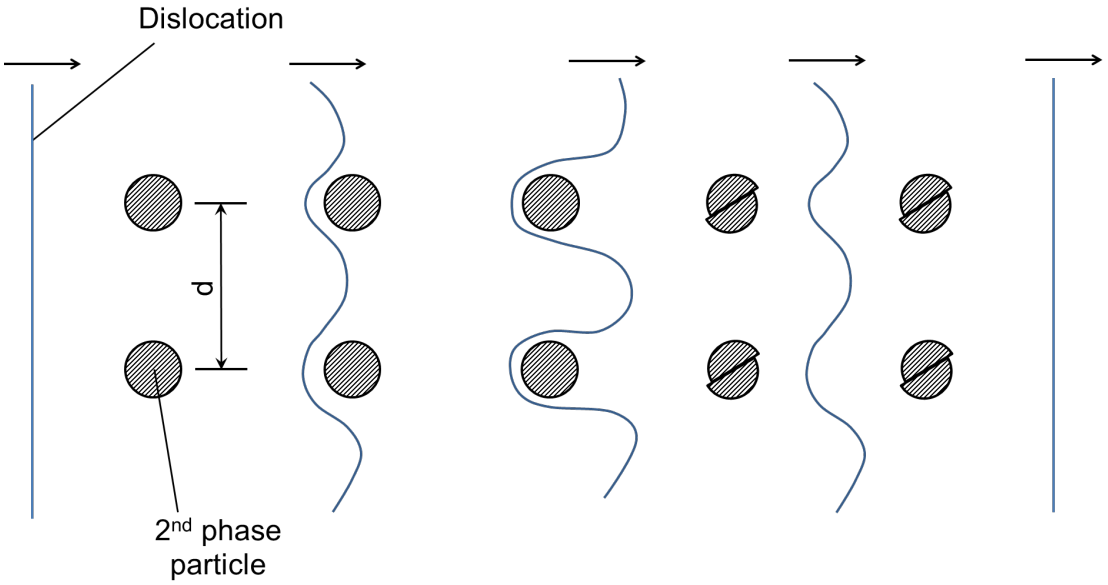

Figure 2.5: Dispersion strengthening from penetrable particles. Inter-particle spacing is d [34].

2.3 Oxide dispersion strengthened steels

The evolution of ODS ferritic/martensitic steels strengthened by a fine dispersion of thermodynamically stable Y enriched oxides can be traced back to the 1960s and 70s, when the Fe based superalloys MA956 and PM2000 were developed to provide high temperature strength and oxidation/corrosion resistance for applications such as gas turbine combustion chambers [40]. The strengthening of these alloys was exerted by dispersion of 10 – 50 nm Y-Al-O based particles [40,41].

Fe based alloy MA957, a derivative from MA956, was subsequently evaluated for potential applications in future nuclear concepts, where conventional austenitic steels had inadequate irradiation resistance and conventional ferritic steels could not deliver suitable thermal creep resistance at service temperatures up to 700 °C [42]. However, both MA956 and MA957 stopped commercial production, due to their high cost and limited market penetration.

Since the late 1980s, ODS steel research for nuclear applications has regained momentum. Leading the thrust was the Japan Atomic Energy Agency (JAEA) which initiated a series of optimizations on composition and processing of ODS steels, and was quickly followed by the EU and the USA [32,41,43–46]. A 9Cr ODS steel targeted for fuel cladding of next generation fast neutron fission reactors was developed with efforts focused on addressing anisotropic mechanical properties in tube and thin cladding after cold rolling [8,47]. An ODS-Eurofer 97, with similar Cr concentration was subsequently developed for potential fusion applications [43,48]. Later developments on ODS steels more oriented for fusion applications demonstrated a trend of higher Cr content up to 12 – 14 wt% [4,44–46]. The most common alloys in this category are referred to as 12YWT and 14YWT, and the nominal compositions of major alloying elements for the main types of ODS steel are summarised in Table 2.4 [44,45].

Table 2.4: Nominal chemical compositions (wt%) of major alloying elements in ODS steels

Alloy	Cr	W	Ti	Al	Y_2O_3
MA956	20	-	0.5	4.5	0.5
PM2000	19	-	0.5	5.5	0.5
MA957	14	-	1.0	-	0.25
9Cr ODS	9	2	0.2	-	0.35
ODS-Eurofer 97	8.6	0.3	-	-	0.3
12YWT	12	2.5	0.4	-	0.25
14YWT	14	3	0.4	-	0.25

2.3.1 Alloying composition

A major transition from the early ODS steels, such as MA956 and PM2000, to the later nuclear oriented steels involved removal of Al due to requirements on low induced activity under high energy neutron irradiation [19].

The addition of Cr provides corrosion and oxidation resistance for the ODS steels, while unlike Ni, it maintains a desirable bcc matrix structure [7]. Cr has a strong impact on stabilizing irradiation generated defects by suppressing the size and motion of the dislocation loops at temperatures higher than 500 °C [49]. Research on model alloys with different Cr contents demonstrated that alloys with higher Cr content (up to 12 wt%) maintained their yield strength and ductility after irradiation at relatively low dose rates of up to 1.5 dpa [50].

The relatively large atoms of W further strengthen the ODS steels via solid solution strengthening, while maintaining low activation of the alloys [7]. The addition of 1 – 3 wt% W in model alloys also benefits fracture toughness after annealing at 800 °C for 1h [51].

Y and O are the backbone elements for the thermodynamically stable NPs that create the dispersion strengthening and radiation damage resistance to the ODS steels. These two elements are typically introduced at the beginning of manufacture in the form of Y_2O_3. However, excess O (subtracting O in the strengthening NPs from total O in the steel) can be incorporated into the steel due to reactions with other alloying elements and by ingress of O from the atmosphere during various stages of production and handling [6,47]. Detailed investigations revealed that the excess O could significantly reduce density and uniformity of the strengthening NPs, as shown in Figure 2.6a and b, and subsequently degrade high temperature strength of the ODS steels [6,47]. In addition, if excess O was not controlled at an appropriate level, it may preferentially combine with other common alloying elements such as Ti and form coarse (> 50 nm) TiO_2 particles that are less effective in dispersion strengthening [52]. Therefore, tight control over excess O is critical to obtain the most effective NPs and avoiding other embrittling oxides.

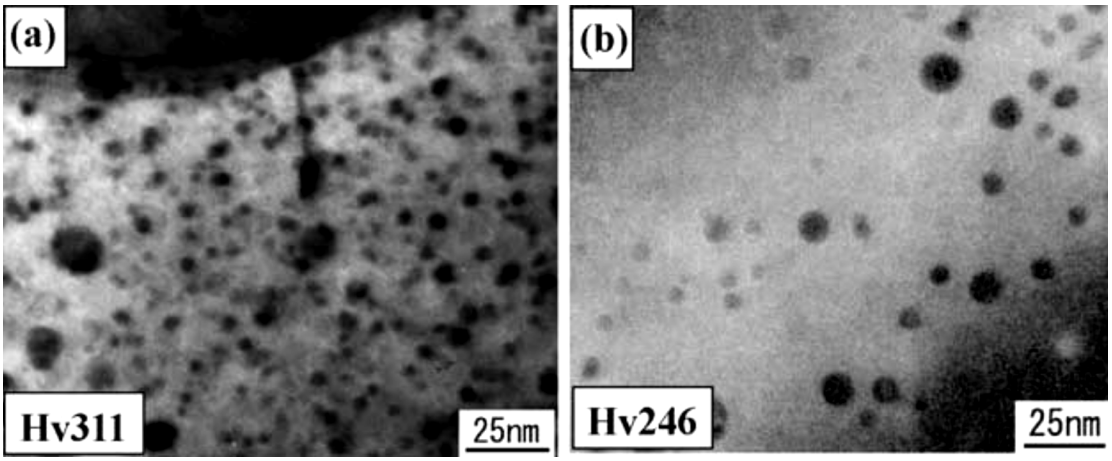

Figure 2.6: Transmission Electron Microscopy (TEM) micrographs showing different NP distributions of model alloy Fe-9Cr-2W-0.2Ti-0.35Y_2O_3 with (a) 0.07 wt% excess O and (b) 0.15 wt% excess O after annealing at 1050 °C for 1 h [6].

The introduction of Ti to the ODS steels essentially changes the composition of the NPs from Y_2O_3 to complex Y-Ti-O enriched oxides. By comparing a model alloy with little or no Ti with 12YWT (see Table 2.4), Ti not only helped reduce size of NPs from

10 – 40 nm (Figure 2.7a) to 3 – 6 nm (Figure 2.7b), but also increased their number density from 10^{20} – 10^{21} m^{-3} to 1 – 5 x 10^{23} m^{-3} [19,44,53]. The 12YWT demonstrated significantly higher tensile and creep strength than the model alloy at temperatures up to 900 °C, which was consistent with microstructural observations and dispersion strengthening theory discussed in section 2.2.4.1 [44]. However, excessive Ti may negatively affect processability of ODS steels due to exaggerated hardening [32]. The Ti concentration of recently developed ODS steels is generally < 0.5 wt%.

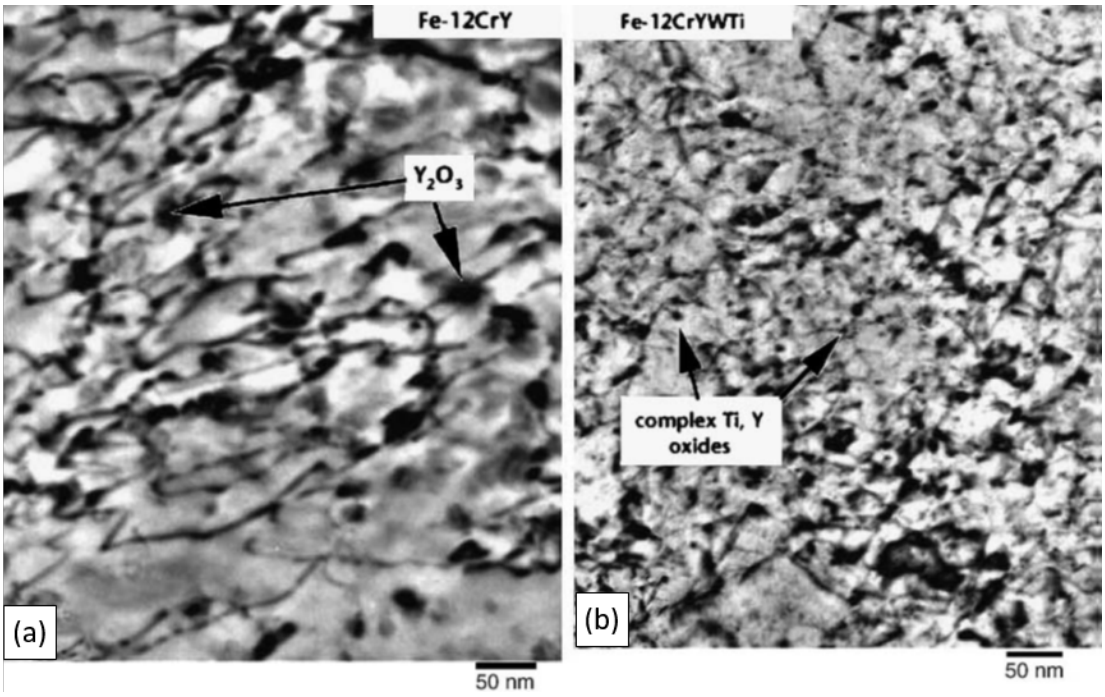

Figure 2.7: TEM micrographs of (a) Fe-12Cr-0.25Y_2O_3 and (b) Fe-12Cr-2.5W-0.4Ti-0.25Y_2O_3 ODS steels. The sample bar was produced by hot extrusion at 1150 °C, followed by hot and cold rolling [44].

2.3.2 Microstructure

Provided with appropriate chemical compositions and processing routes, the newly developed ODS steels possess a ferritic matrix with controlled sub-micron grain sizes, as shown in Figure 2.8, and a recrystallized grain aspect ratio of 1 – 5 depending on the consolidation technique used, such as hot isostatic pressing (HIP) and hot extrusion [21,33]. The refined grain structure contributed to good fracture toughness of the alloys both before and after irradiation [21,33].

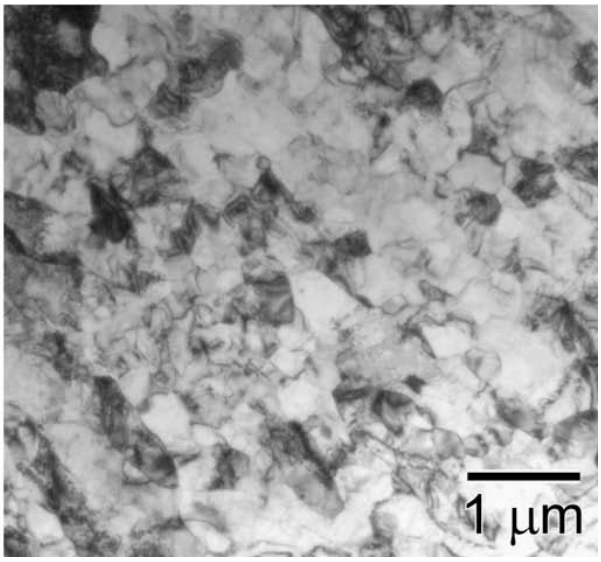

Figure 2.8: TEM micrograph showing the typical fine-scale ferritic matrix microstructure of 14YWT [21]

Although it is well known that the NPs are crucial for ODS steels to achieve both high temperature mechanical properties and radiation damage resistance, ambiguity still remains as to their exact microstructure. Depending on different characterisation techniques, stoichiometric $Y_2Ti_2O_7$ and/or Y_2TiO_5 have been observed using TEM [30,54], while Atom Probe Tomography (APT) investigations more often revealed other relative Y-Ti-O concentrations, even within the same material [16,55]. An opinion of the lower O concentration measured by APT is that O could be 'missed' due to limitations in data acquisition characteristics, although this was disputed by others [48,53]. It may very well be the case that different types of NPs coexist in ODS steels.

Attempts have been made to associate chemical composition of the NPs with their sizes. As shown in Figure 2.9, the smaller (1 – 15 nm) Y-Ti-O clusters have a lower Y/Ti atomic ratio than the larger (15 – 35 nm) particles [16,52]. It was therefore suggested that an appropriate increase of Ti concentration and subsequent decrease of Y/Ti ratio in the composition could promote formation of the smaller NPs [52].

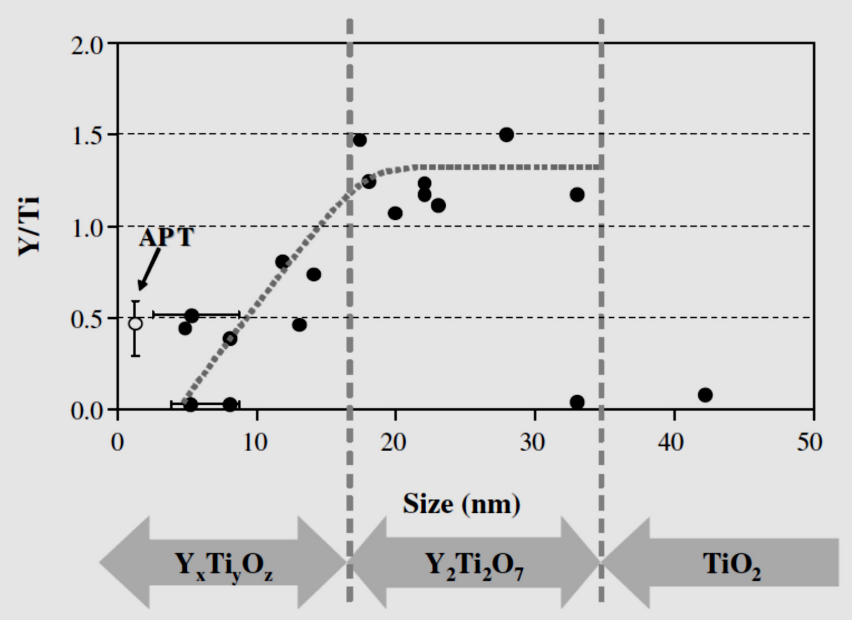

Figure 2.9: Suggested correlation between chemical composition and size of oxide particles. The particles were separated from polished surface of a Fe-14Cr-0.3Mo-1.0Ti-0.25Y_2O_3 ODS steel using carbon extraction replica. The compositions were measured using Scanning Transmission Electron Microscopy (STEM) Energy Dispersive X-ray spectroscopy (EDX) [52].

Investigations of smaller (< 10 nm) NPs using APT also suggested that Y-Ti-O particles were likely to be surrounded by a roughly 2 nm Cr-rich region in the matrix, which was referred to as a 'core-shell' type structure [48,53,56]. It was proposed that the Cr rich shell acted as a wetting layer for formation of the NPs, which could be another function of the alloying element in the ODS steels [56].

2.3.3 Performance

The high temperature mechanical properties of ODS steels, including fracture toughness, tensile and creep strength have been investigated by many researchers [33,41,44,57].

As shown in Figures 2.10a and b, 12YWT optimized for future nuclear applications demonstrated superior tensile strength at temperatures up to 600 °C and thermal creep resistance given by a Larson-Miller-Parameter (LMP) when compared with earlier

commercial ODS steel PM2000 and conventional ferritic/martensitic low activation steel 9Cr2WVTa [41,44]. Investigations of high temperature tensile strength of 14YWT revealed similar promising results [33]. After irradiation at 300 °C to a relatively low dose of 1.5 dpa, 14YWT demonstrated good radiation damage resistance, with negligible irradiation hardening up to 300 °C and approximately 10% increase of yield strength at 600 °C [33].

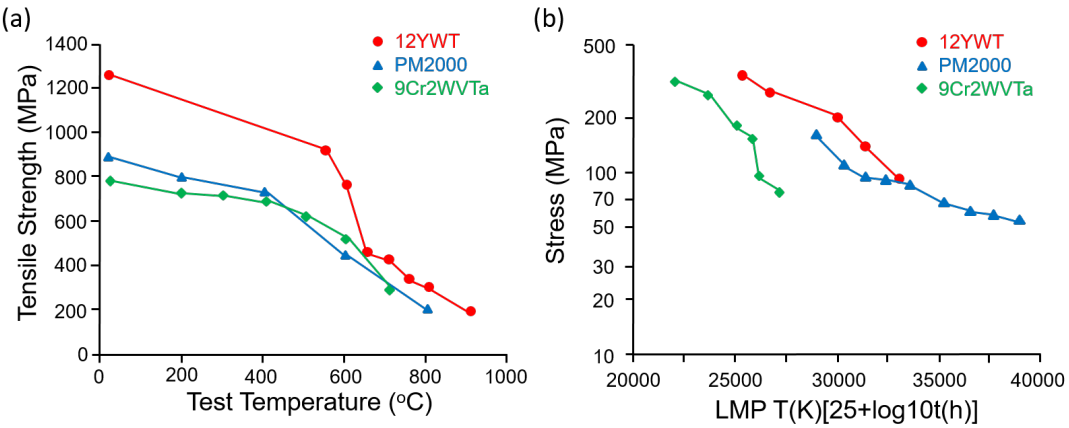

Figure 2.10: Comparison of (a) tensile strength; and (b) creep strength (rupture stress vs. Larson Miller parameter) for 12YWT, PM2000 and 9Cr2WVTa [41].

14YWT also displayed good fracture toughness of approximately 175 $\mathrm{MPa}\sqrt{\mathrm{m}}$, compared with MA957 of about 130 $\mathrm{MPa}\sqrt{\mathrm{m}}$ [33]. The ductile brittle transition temperature (DBTT) of the 14YWT steel (- 188 °C) was more than 60 °C lower than that of the ferritic/martensitic Eurofer 97 steel [33]. After irradiation at 300 °C to 1.5 dpa, an approximately 20 % increase of fracture toughness and a small 6 °C increase of DBTT suggested the 14YWT has favourable resistance to radiation embrittlement [33].

The irradiation resistance of ODS steel mechanical properties was also consistent with microstructural observations. Compared with relatively coarse (up to 10 nm) and bimodal distributed He bubbles observed in a conventional ferritic/martensitic steels (Figure 2.11a) after irradiation, He bubbles were suppressed to a finer scale (< 2 nm) with better uniformity in 12YWT (Figure 2.11b) [30].

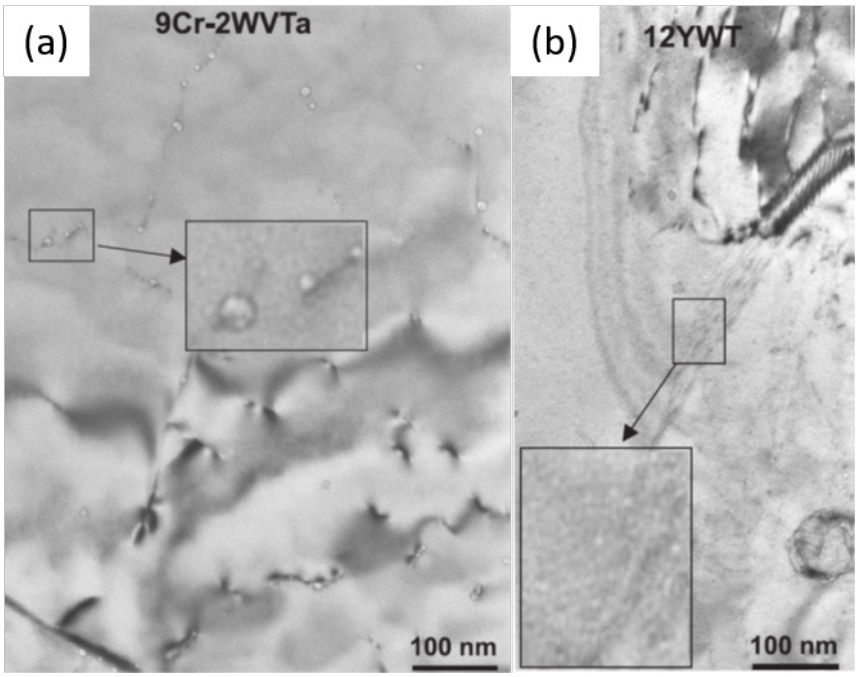

Figure 2.11: TEM micrographs showing (a) 9Cr2WVTa; and (b) 12YWT steels after irradiation to 50 dpa at 650 °C with 3.2 MeV Fe^{+} and 330 KeV He^{+} ions [30].

2.4 Processing of oxide dispersion strengthened steels

Processing of ODS steels determines critically the extent to which the designed microstructure and subsequent performance might be achieved. In particular, the dissolution/break-up (see later) and reprecipitation of the NPs, which takes place in the early stages of processing. There is little subsequent opportunity to manipulate the NPs because of their deliberate insolubility and stability.

One of the major difficulties for manufacture of the ODS steels is the generation of uniformly distributed Y-Ti-O enriched NPs. The negligible solubility of Y in Fe is shown in the equilibrium binary phase diagram in Figure 2.12, which has prevented the use of traditional liquid metal processing to mix the elements in liquid phase, quench in solid solution, and then reprecipitate from a Fe-Y solid solution with simultaneous 'internal oxidation' to oxide particles [58–60].

In a Cu-Y system, casting resulted in segregation of the more reactive Y as Cu-Y intermetallics in the inter-dendritic spacings [60]. Although these intermetallics could be

'internally oxidized' to form oxides, they were on the scale of the cast microstructure (10 – 100 μm), which is too coarse to stabilize irradiated alloys usefully [61]. To circumvent the problems of casting/liquid metal processing, a solid-state processing route has been developed based on MA [58].

MA at room temperature is capable of refining and dispersing desirable quantities of Y_2O_3 into the ferritic matrix by forming a supersaturated solid solution of Y and O in Fe, a metastable amorphous phase of an extremely fine scale Y-O containing glass, or possibly even very tiny Y_2O_3 fragments [12,18]. These non-equilibrium structures can then be decomposed at elevated temperature in subsequent consolidation and thermomechanical treatments, through which Y-O containing crystalline phases (Y_2O_3, Y_2TiO_5, $Y_2Ti_2O_7$ *etc.*) with desirable size, distribution and microstructure can be formed [12,18].

Figure 2.13 illustrates a typical MA based process route for ODS steels [62]. Steel powder, either in elemental or pre-alloyed form, is first mixed with Y_2O_3 powder in pre-determined fractions, followed by the MA to form a steady-state single phase powder material (typically 20 – 60 h). After vacuum degassing, the milled powder is consolidated into bulk using techniques such as HIP or hot extrusion. The consolidated ODS steels are usually then subjected to further thermomechanical processing by forging, rolling, extrusion *etc.* in order to ensure full density, to recrystallize the ferritic grains, and to provide optimal ageing response to balance critical precipitates of interest.

Since the thermodynamically stable Y-Ti-O rich NPs cannot be easily manipulated once formed, control over their formation and subsequent properties of the ODS steels can only be achieved from the beginning of processing, so that MA is the key processing stage and is the subsequent focus of the review [2,4,7].

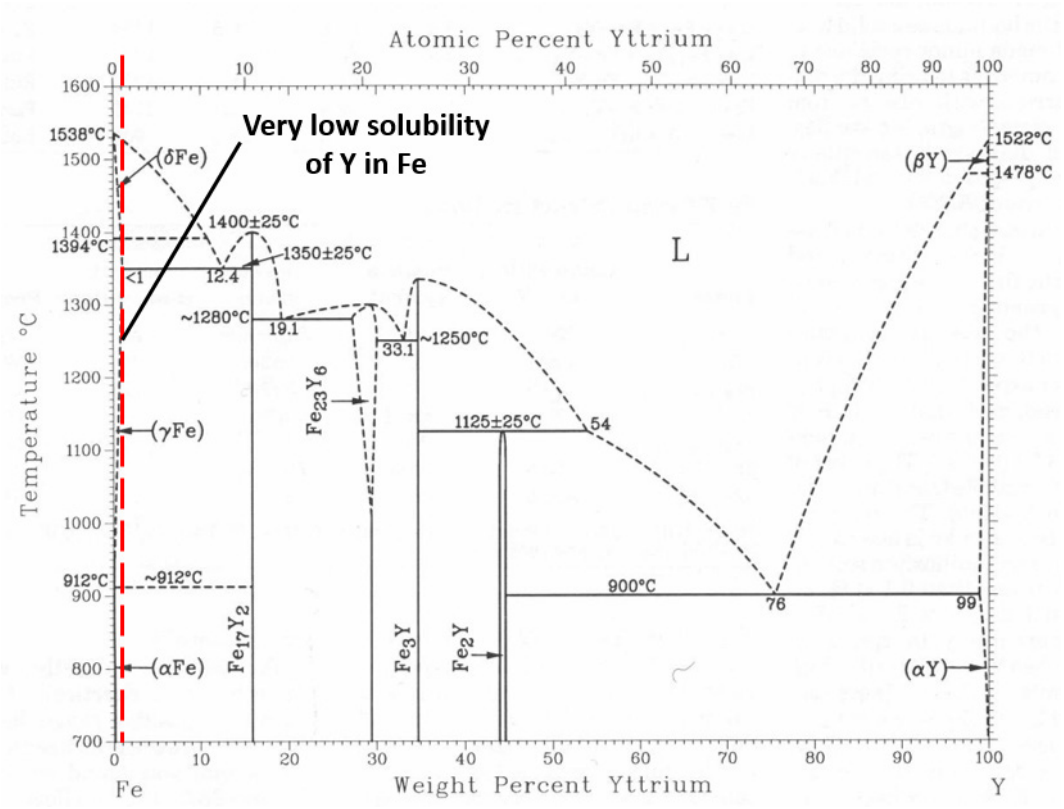

Figure 2.12: The Fe-Y equilibrium binary phase diagram [63]

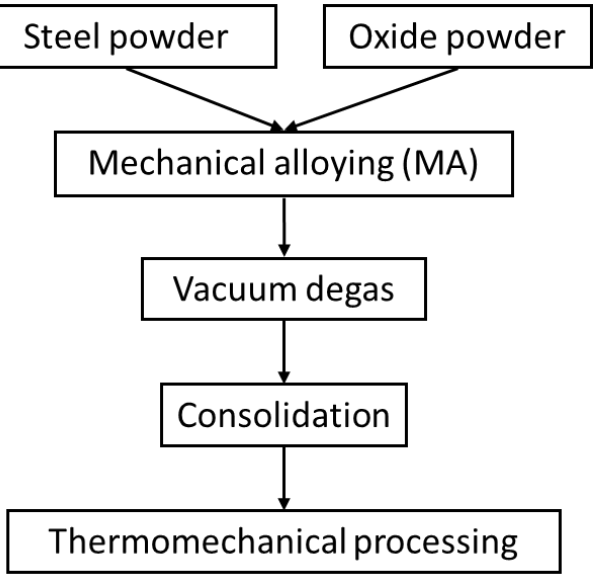

Figure 2.13: The flow chart of typical process route for ODS steel manufacture [62]

2.4.1 Mechanical alloying

MA was originally developed in the 1960s for the production of ODS nickel based superalloys [64]. After more than four decades of development, it now provides the

capability to manufacture a range of complex dispersion strengthened alloy systems, including nickel, cobalt, iron, titanium and aluminium based alloys [40,65].

MA is carried out by a highly agitated ball charge which constantly creates ball-powder-ball collisions [40]. Depending on the characteristics of the starting materials, MA can be categorised into three different types of powder combinations, ductile-ductile, ductile-brittle and brittle-brittle [18,42]. The production of ODS steels is a typical ductile-brittle type, in which the steel powder is relatively ductile (at least initially) compared with the brittle Y_2O_3 powder [18]. As shown in Figure 2.14, during the initial stages of MA, the ductile steel powders undergo cycles of plastic deformation, work hardening, brittle fracture, and cold welding to form a characteristic layered structure [18,42]. On the other hand, the brittle oxide particles are fractured under milling ball collisions and entrapped into the cold welded interfaces of the steel particles [18,42]. With increasing milling times, the layered structures are refined into smaller inter-layer spacings, and become highly convoluted. Eventually, through a process of continued atomic scale transfer, the different constituents are homogeneously distributed throughout the milled powder particles. Along with the high density of defects (such as vacancies and dislocations) generated by the input of mechanical energy, the inter-layer spacings are refined to a state that short-range diffusion of different constituents is facilitated, tending towards a supersaturated solid solution or, if still insoluble, an amorphous phase [18,42]. These micro- or nano-scale arrangements are generally highly metastable, and presence of much higher defect densities distorts equilibrium thermodynamics so that a wide range of seemingly unlikely solid solutions can be obtained. These effects can be even further from equilibrium if cooling is applied, although milling times can become extended [42].

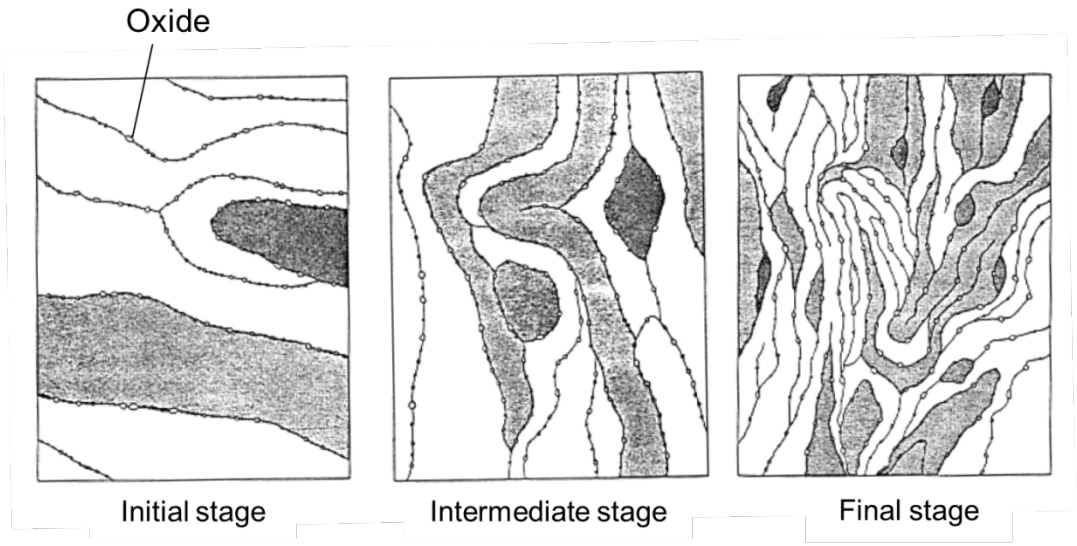

Figure 2.14: Schematic illustration of microstructure evolution of a ductile-brittle powder combination [42].

2.4.1.1 Steady-state

The steady-state condition developed in MA is typically used to judge the completion of a milling process [42]. At steady-state, the composition of each powder particle is identical and conforms to the proportion of elements in the starting materials [42]. It is also an equilibrium point when cold welding and brittle fracture of the powder particles reaches a dynamic balance [18].

The characterisation of steady-state generally requires a combination of techniques including particle size measurement, microhardness, X-ray diffraction (XRD) investigation of the phases, and electron probe microanalysis (EPMA) of elemental segregation [16,55,66,67].

Figure 2.15a shows a typical evolution of average particle size with increasing milling time [66]. After a rapid drop at the first 10 h, the average particle size reached a steady-state at approximately 18 μm. A slight increase in diameter after 12 h was likely caused by agglomeration of the particles due to over-milling. The reducing error bar indicated a narrower particle diameter distribution with increasing milling times, which is another general trend of particle evolution during MA [18,67].

Figure 2.15b illustrates a typical evolution of powder microhardness, showing that hardness reached a plateau of approximately 1200 kg/mm^2 after 10 h milling [66].

A typical evolution in the powder XRD trace with increasing milling time involves the progressive reduction in peak intensity from Y containing minor constituents, and broadening of the bcc Fe matrix peaks due to a reduced crystallite size and/or an increased lattice strain caused by defects and solutionizing of the Y and any impurities [29,66,67]. XRD data may be interpreted using various methods such as Rietveld analysis to produce optimized fitting between measured data and a modelled pattern, through which properties such as crystallite size and lattice strain can be obtained. Figure 2.15c shows the evolution of the calculated (using the Scherrer formula) crystallite size reached a steady-state at approximately 41 nm after 10 h milling, which was consistent with the milling times to achieve steady-states in particle size and microhardness in Figures 2.15a and b [66]. However, the major disadvantage of Rietveld analysis is the fitting of many non-structural parameters, including background, peak shape, lattice constants, preferred orientations and phase fractions *etc.*, some of which may be difficult to obtain; many degrees of freedom in the fitting provides the chance for non-physically sensible deductions.

EPMA involves detecting X-rays of elemental specific wavelengths generated by interaction of incident electron beam with the sample material, and is capable of quantifying elemental concentrations and their spatial distribution, with a resolution of typically 1 – 2 μm [68]. However, since the characterisation samples a comparatively small volume of material, a reliable determination generally requires measurements to be taken from multiple points.

Other higher resolution techniques such as TEM and APT can also be used to characterise the chemical distributions of milled powder particles, but results obtained at the nanometre scale should be treated extremely carefully, since they may not reflect properly the chemical state of the bulk of the powders [53,54].

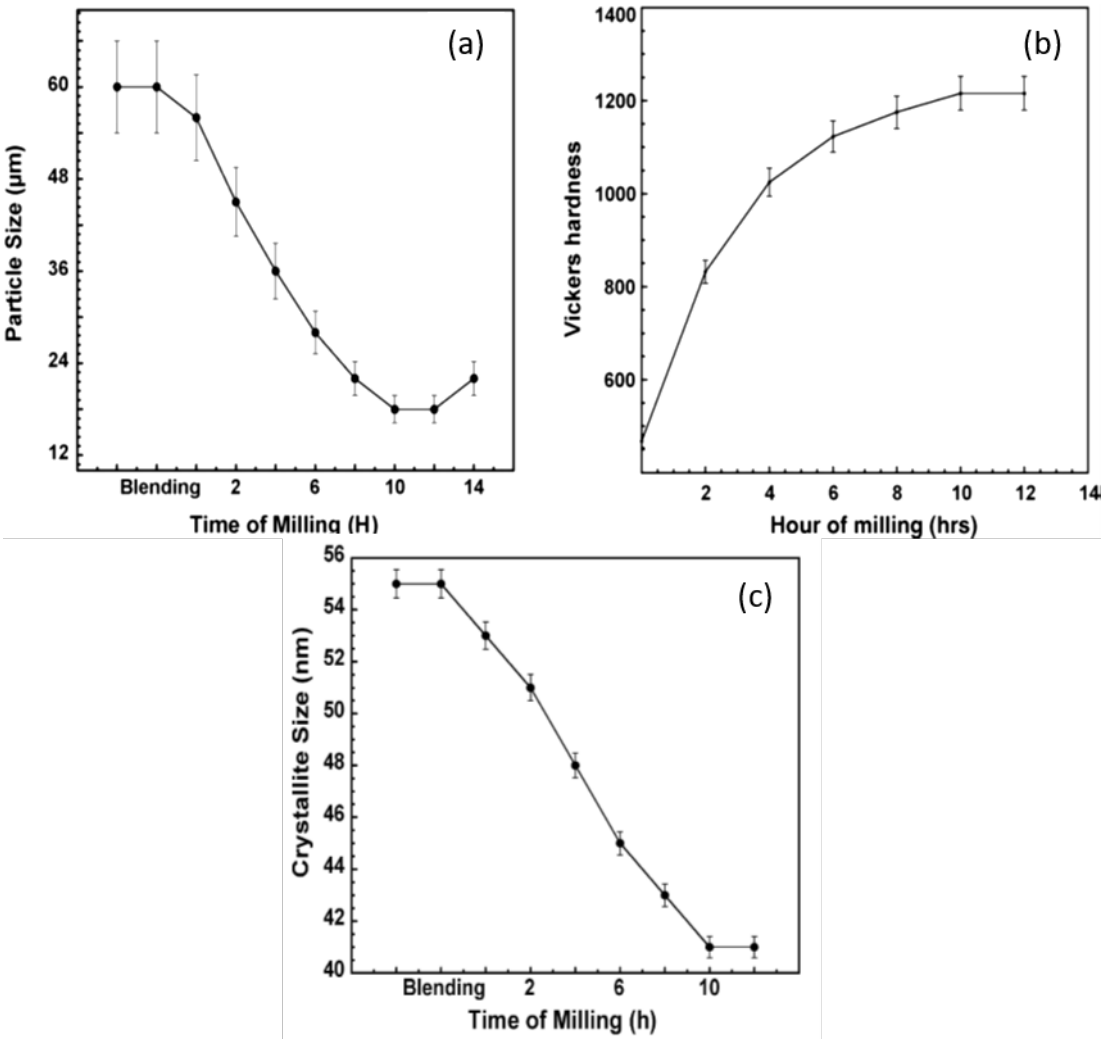

Figure 2.15: Evolution of (a) particle size; (b) microhardness; and (c) crystallite size of ODS Eurofer 97 powder as a function of milling time [66].

2.4.1.2 Milling variables

To achieve a homogeneous distribution of constituents in the powder particles, successful MA requires control over milling variables, including feedstock materials, milling energy, and milling atmosphere.

Feedstock materials for MA ODS steels relate to the use of either elemental or pre-alloyed steel powder [29]. The use of elemental powders provides advantages such as more freedom in chemical composition adjustment and lower cost. Researchers have declared production of high quality ODS steels from elemental powders, but others dispute their quality, and have argued that elemental homogeneity was always

restricted, and that pure elemental powders were generally relatively reactive and suffered more from excessive O and N contamination [29,67,69].

Milling energy is determined by the shape, mass of milling balls, and the rotational or comminution energy applied. Commonly available laboratory ball mills include shaker, planetary and attritor mills, which have milling energies in a high to low order, and load capacities in an exactly opposite order [18,42]. A comparison between different mills found that milling for 20 min in a high energy shaker mill and 20 h in a low energy vibratory mill yielded qualitatively equivalent results [70]. Hence, a well-designed combination of experiments can be carried out by applying high energy mills for initial screening of process parameter and composition, and gradually transitioning into low energy and high capacity mills to emulate commercial production.

As for the milling atmosphere, MA of ODS steels is commonly carried out under a protective gas such as Ar to limit the amount of O in the final product [6,18,47]. However, Ar was reported to remain in a 9Cr ODS steel as nano-sized bubbles after consolidation, and were stable under TEM characterisation environments, although their exact effect on ODS steel properties requires further investigation [71].

2.4.2 The formation mechanisms of Y-Ti-O enriched nano-sized particles

Although the Y_2O_3 in the starting material decomposes/vitrifies/fractures at the nano-scale during MA, the exact mechanism(s) and those controlling the reprecipitation of NPs retains some uncertainty.

The commonly reported mechanism is that the non-equilibrium MA process induces dissolution of the Y_2O_3 into the ferritic matrix, forming a supersaturated solid solution of Y and O in Fe, which then precipitates as Y-Ti-O enriched NPs (in Ti containing variants) during the following consolidation/annealing process [7,12,29,32]. This mechanism has been supported by the disappearance of Y_2O_3 peaks from XRD patterns and an increasingly homogenous chemical distribution of Y and O within the

matrix at the steady-state, as well as precipitation of relatively complex NPs containing elements *e.g.* Ti, that were not present in the starting ceramic powder [12,48,53].

On the other hand, it has also been suggested that Y_2O_3 in the starting powder mix was dissociated during MA via fragmentation and amorphisation, which were subsequently reorganized into the Y-Ti-O enriched NPs during consolidation/heat treatment, *i.e.* there is no distinct dissolution and subsequent nucleation steps [72]. This proposition was supported by progressive disappearance of Y_2O_3 peaks in neutron and X-ray diffraction patterns during MA, with an almost constant lattice strain even for a 10 wt% Y_2O_3 model alloy, which was hard to reconcile if all the Y and O were fully dissolved in the Fe matrix [72,73].

Based on the evidence provided by the two different propositions, it is likely that both mechanisms may contribute to the disappearance of Y_2O_3, while amorphisation may become more significant at high Y_2O_3 fractions. Since understanding of the NP formation mechanism provides valuable insights on alloy design of the ODS steels, further investigations are needed.

2.5 Alternative processing routes for ODS steels

Although MA has been widely practiced for the manufacture of ODS steels, its prolonged processing time, small batch size, tendency for contamination associated with high specific area of the powder, high inherent cost of feedstock powders, *etc.* remain major disadvantages for technological implementation at any useful scale [6,13–18]. Since large sized commercial ball mills normally generate much lower milling energy than laboratory ones, it can be safely estimated that some of these disadvantages will be further amplified in commercial production [18,70].

Alternative processing routes to the conventional MA for ODS steels have been investigated with the target of better cost-effectiveness, *i.e.* to shorten processing time, and/or to improve microstructure and subsequently performance of the material. While

perhaps not providing the performance achievable in small batch laboratory processing by MA, these alternative approaches may still provide material with a usable cost-benefit-scale balance.

2.5.1 Reactive mechanical alloying

One of the leading alternative options to the manufacture of ODS steels is reactive MA (also referred to as mechanochemical synthesis), in which a solid state chemical reaction to form NPs is induced [16,55,74]. Provided with appropriate starting material and conditions, the formation of nanostructures can generally be promoted [18,75,76]. Although this approach is not a radical departure from traditional MA, it may offer some attractions for reduced times.

A characteristic feature of solid state reactions is that formation of the product phase spatially separates from the reactant phases. Therefore, solid state reactions are generally limited by diffusion of reactant atoms through the product phase. The accumulating product phase may effectively act as a barrier layer for further diffusion of reactant atoms and eventually inhibits the reaction, making some thermodynamically feasible reactions kinetically impractical [18,77].

MA can substantially enhance the kinetics of solid state reactions by: 1) increasing overall surface area, vacancy and dislocation densities, while decreasing diffusion distances as a result of particle size reduction; and 2) dynamically generating fresh surfaces for reactions due to repeated welding and fracturing of powder particles [65,77]. Consequently, MA provides a useful means to facilitate diffusion processes and to accelerate subsequent solid state reactions. Reactions that otherwise require high temperatures to overcome kinetic barriers can be carried out at lower or even room temperatures via MA [65,77].

The study of the reactive MA started in 1989 with a successful demonstration of reducing CuO to Cu through milling of CuO and Ca powders [78]. From then on, reactive

induced reductions have been reported for various metal oxides, chlorides, sulphides and hydrides [18,77,78], most of which can be expressed in the following displacement reaction formula:

$$MX + R \rightarrow M + RX$$

where M is a pure metal, which is less reactive than pure metal R; MX is M in its oxide/chloride/sulphide/hydride etc.; and RX is R in its oxide/chloride/sulphide/ hydride etc. More extensive lists of previously studied reactions induced by reactive MA can be found in reviews [18] and [77]. A common feature of these reactions are their negative enthalpy change (ΔH), which means they are all thermodynamically feasible yet kinetically constrained [18].

2.5.1.1 Reactive mechanical alloying for ODS steels

Although reactive MA has been studied since the late 1980s, its application for the manufacture of ODS steels started recently. Brocq et al. [16,55,74] first proposed and explored the idea based on reaction: $2Fe_3Y + Fe_2O_3 \rightarrow 8Fe + Y_2O_3$. Instead of directly adding Y_2O_3 powder at the start of milling as in conventional MA, the yttrium containing precursor Fe_3Y was used, from which formation of Y rich strengthening oxides was promoted from reduction of Fe_2O_3, with the input of mechanical energy [74,79].

The idea was validated by MA of Fe_3Y and Fe_2O_3 powders with a target composition of Fe-60.5Y_2O_3 [74]. The very high Y and O contents in the model ODS alloy facilitated XRD characterisation (which is generally difficult in ODS steels with oxide fractions < 1 wt%), which confirmed the dissolution of reactants after 280 h milling, as well as the formation of Y_2O_3 after annealing at 800 °C for 1 min [74].

Reactive MA of Fe_3Y, Fe_2O_3 and pre-alloyed Fe-14Cr-2W-1Ti at more general compositions with equivalent Y_2O_3 contents of 1 wt% and 0.25 wt% were then carried out [55,74]. As shown in Figure 2.16b, Y-Ti-O enriched NPs that are similar to those obtained via conventional MA were observed in annealed powder [74]. Their relatively

small diameter (< 10 nm) was also consistent with the proposition based on conventional MA that a < 1 Y/Ti atomic ratio of the starting composition generally promoted formation of smaller (1 to 15 nm) NPs [52].

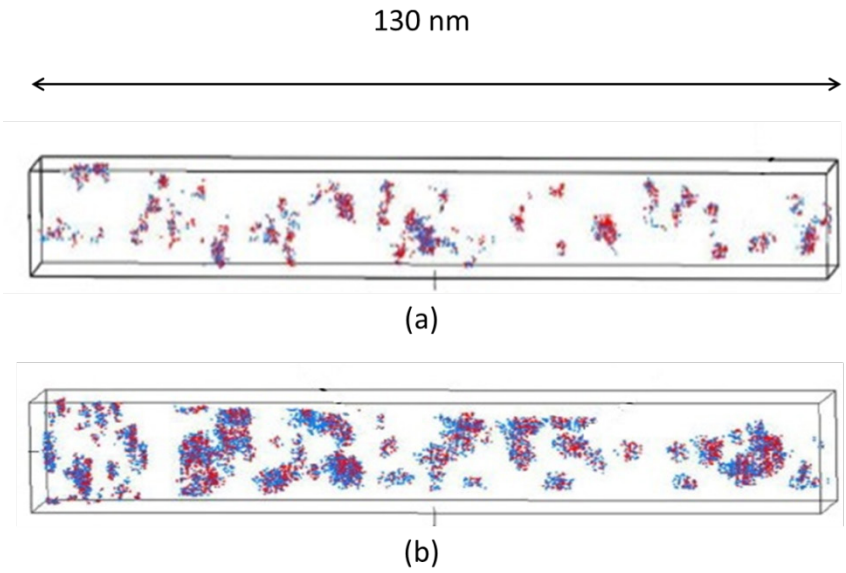

Figure 2.16: 3D APT atomic reconstruction showing NPs in Fe-14Cr-2W-1Ti-1Y_2O_3 ODS steel in the (a) as milled; and (b) annealed state. Atoms of Ti and TiO are in blue; Y and YO are in red [16].

However, the detection of small (0.8 ± 0.5 nm) Y-Ti-O enriched NPs in the as-milled powder in Figure 2.16a prompts the idea that MA not only facilitates the dissolution of reactants (Fe_3Y and Fe_2O_3) into the metallic matrix, but also promotes the NP nucleation [16,55,74]. Subsequent growth in quick annealing (5 min) at relatively low temperature (800 °C) resulted in a high number density of comparatively small NPs [16,55].

Possible differences in NP formation mechanisms may reflect the differences in conventional and reactive MA. Since Brocq et al. [16,55,74] used substantially longer milling times (144 – 280 h in a planetary mill) than those applied in conventional MA (several tens of hours), it is possible that NP nucleation would have also occurred in the powders of conventional MA with long enough milling times. However, if such nucleation of NPs during MA does not cause decisive improvement in the final

distribution and density of the strengthening NPs, milling should be stopped when dissolution of reactants is complete to save time and cost of production, and reduce potential contamination from the milling media.

It is worth mentioning that although protective Ar environments are generally applied during MA and feedstock/material transfer, a higher (35 %) than nominal O fraction was detected in EPMA analyses of as-milled powder [74]. The excess O suggested potential ingress of a small amount of O during processing, which is always difficult to exclude. Careful control of the relative amounts of all feedstocks may provide a possible method to compensate for any excess O pick-up by adding less oxygen source (Fe_2O_3 powder) at the start of milling.

In addition to the use of intermetallic Fe_3Y, reactive MA based on reduction of Fe_2O_3 by the hydride YH_2 has also been investigated [79]. The milling was conducted using YH_2, Fe_2O_3, TiH_2 and pre-alloyed Fe-14Cr-3W powders with a nominal composition of Fe-14Cr-3W-0.3Ti-0.3Y_2O_3. Decomposition of the reactants was achieved after 24 – 48 h milling in a planetary mill, and NPs were successfully nucleated after annealing at the same temperature (800 °C) as those used for a Fe_3Y precursor [79]. The formation of NPs in this case appeared consistent with the conventional formation mechanisms, without the detection of nucleation in the as-milled state. The precipitates were stoichiometric $Y_2Ti_2O_7$ (10 – 20 nm in diameter) according to TEM characterisation, which is the same as those observed in a typical ODS steel such as 14YWT. Interestingly, Fe_2O_3 was suggested to promote decomposition of YH_2, presumably as free energy is released as Fe_2O_3 converts to Y_2O_3 [79].

Overall, reactive MA has proved to be a feasible alternative processing route for ODS steels, in that the Y containing precursors can be successfully dissolved into the metallic matrix, and Y and O enriched NPs can be formed after subsequent heat treatment. Based on the nature of solid state reaction, it can be speculated that reactive MA may offer potential advantages compared with conventional MA. First, since the Y

containing precursors are less thermodynamically stable than Y_2O_3, less energy and shorter milling times are likely to be required to achieve a supersaturated solid solution during MA [74]. Then, formation of the more favourable small sized (< 15 nm) NPs can be encouraged due to *in-situ* chemical reaction [16,52,75,76,80]. Last, the excess oxygen content that deteriorates high temperature tensile and creep properties can be better controlled since addition of the yttrium containing precursors does not involve any deliberate addition of O as Y_2O_3 [6,16,52].

2.5.2 Liquid metal processing

The key to ODS steel manufacture is to disperse the thermodynamically stable Y and O enriched NPs evenly and at low fraction, high number density and fine-scale in the Fe based matrix [74]. A pivotal step to achieve this in the MA route is the decomposition of Y containing materials into the metallic matrix and formation of a non-equilibrium supersaturated solid solution/amorphous phase by the input of mechanical energy.

Unlike conventional liquid metal processing that generally implies solidification rates < 1 mm/s, melt spinning is capable of achieving significant extensions of solid solubility as the strongly non-equilibrium solidification suppresses the segregation of minority alloying additions [40,81]. Potentially (and as expected in this thesis), the supersaturated Y in the matrix can subsequently be oxidized to precipitate and form the desirable Y and O enriched particles.

2.5.2.1 Melt spinning

As shown in Figure 2.17, the melt spinning process starts with melting an alloy of desirable composition in a crucible. After holding in the molten state for a short time of a few seconds to allow elemental homogenization, a stream of the molten alloy is ejected by a protective gas over-pressure, and brought into contact with a rapidly rotating substrate (typically Cu) surface. Once the melt impinges onto the substrate, it is rapidly solidified, forming a thin ribbon and detaching from the substrate under centrifugal force [82]. The formation of a metastable supersaturated solution generally

requires a cooling rate above 10^5 K/s (or more useful, a solidification velocity of > 1 mm/s), with extent of super-saturation depending on the actual velocity of solidification and the specific alloy system [81].

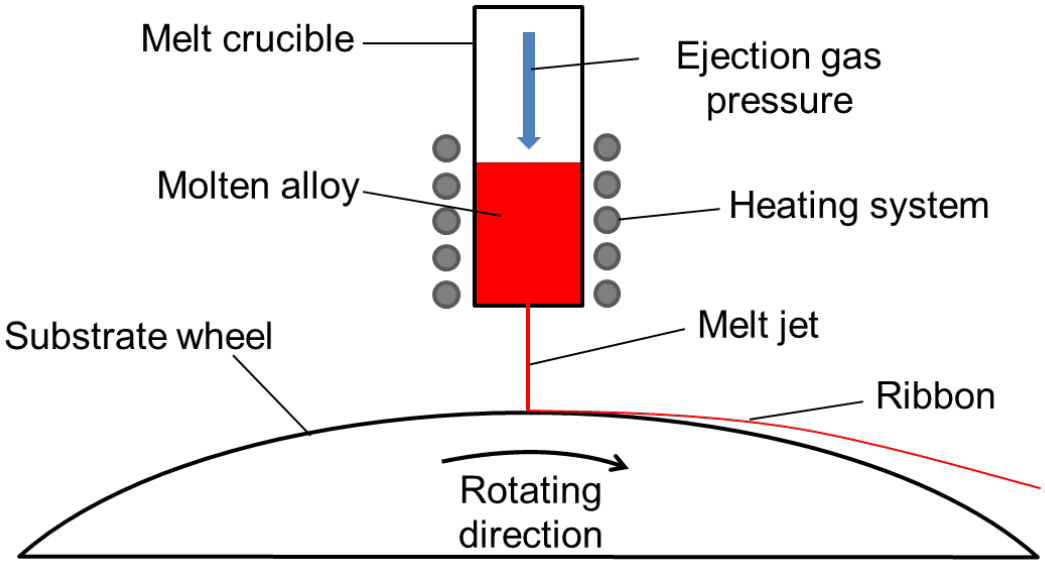

Figure 2.17: Schematic illustration of melt spinning process [82]

The melt spinning process is capable of forming supersaturated solid solutions in alloys composed of early (Zr, Nb, Ta, and Ti *etc.*) and late (Fe, Co, Ni, Cu, Zn and Pd *etc.*) transition elements, as well as group IIA and IIIA metals (Mg, Ca, Al, and Be *etc.*) [83]. Although the obtainable solubility extension in melt spinning is generally smaller than MA, especially for those alloy systems that possess very low solid solubility at room temperature [18], it should be noticed that the required extension for an ODS alloy is not very high, considering a typical ~ 0.2 wt% Y concentration in common ODS steels, such as 14YWT.

Figure 2.18 illustrates a typical microstructure distribution in a melt spun ribbon. The region in close vicinity of the ribbon/substrate interface is the chill zone (A) and is comprised of fine equiaxed grains with random orientation [82]. In some cases, an entirely partitionless or even amorphous structure can be formed in this region, especially if large solidification undercoolings are induced immediately before

nucleation. With a then reduced cooling rate once solidification is nucleated due to the release of latent heat, separation of the ribbon from the wheel, and increasing distance of the solid/liquid interface to the cold wheel surface, columnar grains (B) appear from 'top' of the chill zone growing opposite to the gradient of heat flow, which then transitions (C) into a coarser or even equiaxed dendritic structure (D) towards free side of the ribbon, as the cooling rate continues to reduce [82]. Presence or absence of each of these microstructure types is possible in various cases and depends largely on the local cooling rate, which is controlled by the amount of undercooling prior to rapid solidification and the velocity of the melt/substrate interface [82].

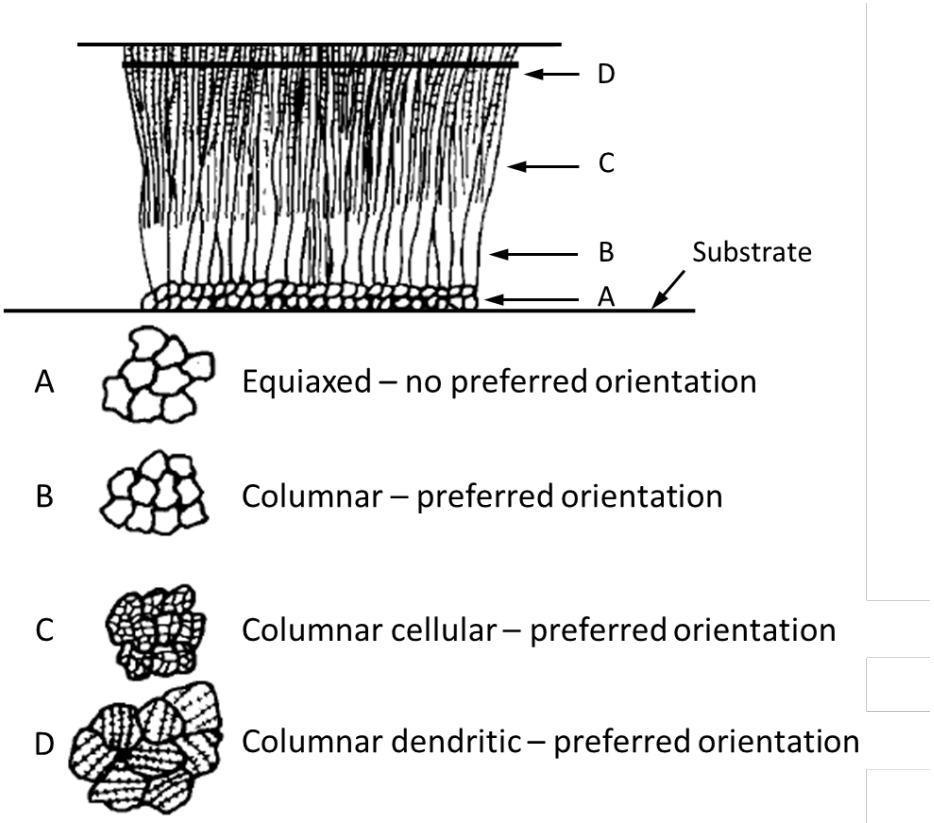

Figure 2.18: Schematic illustration of solidification microstructure that may appear in melt spun ribbons [82].

2.5.2.2 Internal oxidation

For a metallic solid solution, internal oxidation is a process through which selective oxidation of a less noble solute occurs with the introduction of oxygen, forming finely

dispersed oxides in the matrix of the solvent [84–86]. A successful internal oxidation generally requires the following conditions:

1. The ability of oxygen to diffuse into the alloy and react with an alloying element at an appreciable rate;
2. The formation of an oxide of the alloying element that is more stable than oxides of the solvent metal;
3. A relatively low solubility of this oxide in the matrix [85,86].

Internal oxidation has been successfully applied in production of commercial Cu ODS alloys, GlidCop®, for over 40 years. The strengthening oxides are produced by oxidizing Al from dilute Cu-Al alloy (< 0.7 wt% Al) powders, which are then consolidated and processed into required dimensions [60,61,87]. The 1 – 3 vol.% Al_2O_3 micro-particles provide Cu ODS alloys with a good combination of high electrical/thermal conductivity and high temperature mechanical properties [61].

Investigations of internal oxidation in Ni, Fe, Ag and other Cu alloys have also been reported [61,84,86]. A common feature of these alloying systems is the capability of forming an extended solid solution relatively easily.

The prospects of applying more thermodynamically stable oxides from elements insoluble in the solvent matrix, such as Y_2O_3 strengthened ODS steels, eventually attracted an investigation of the internal oxidation behaviour of Fe-Y intermetallics [88]. Figures 2.19a and b show the lamellar (about 20 nm in width) and spherical particles (40 – 80 nm in diameter) produced from the internal oxidation of bulk $Fe_{17}Y_2$ using the Rhine's pack [85] method at 700 °C for 3 days [88]. Penetration depths of 10 – 20 μm were achieved in the bulk samples, while XRD characterisation of powder samples oxidised in the same conditions found $FeYO_3$, Y_2O_3 and FeO [88].

It is encouraging that oxides with a similar size as those produced by MA were achieved through internal oxidation, but the distribution was inhomogeneous, which is

expected due to gradient of oxygen diffusion during internal oxidation of bulk samples. Oxide particles in internally oxidized powder samples may show a better distribution, but were not presented in this work.

Another potential problem of the particles attained via internal oxidation compared with those via MA routes was their lower thermodynamic stability [88]. There was substantial coarsening of internally oxidized particles from 20 – 40 nm to 0.5 – 1 μm (Figure 2.19c), while an investigation of NPs produced via MA in 14YWT reported a much smaller increase in average diameter from approximately 3 nm to only 9 nm after annealing at 1300 °C for 1 day [45,88]. This strongly suggested a different structure and/or composition of the internally oxidised particles from those generated via MA.

It is worth mentioning that although internal oxidation was conducted using Fe-Y intermetallic with the lowest available Y concentration ($Fe_{17}Y_2$), its 15.8 wt% Y was still much higher than proposed compositions of useful ODS steels of approximately 0.2 wt% Y. Therefore, other processing routes that are capable of dissolving and distributing Y in Fe at a lower and more useful content should be explored for internal oxidation to be an effective method of ODS steel manufacture.

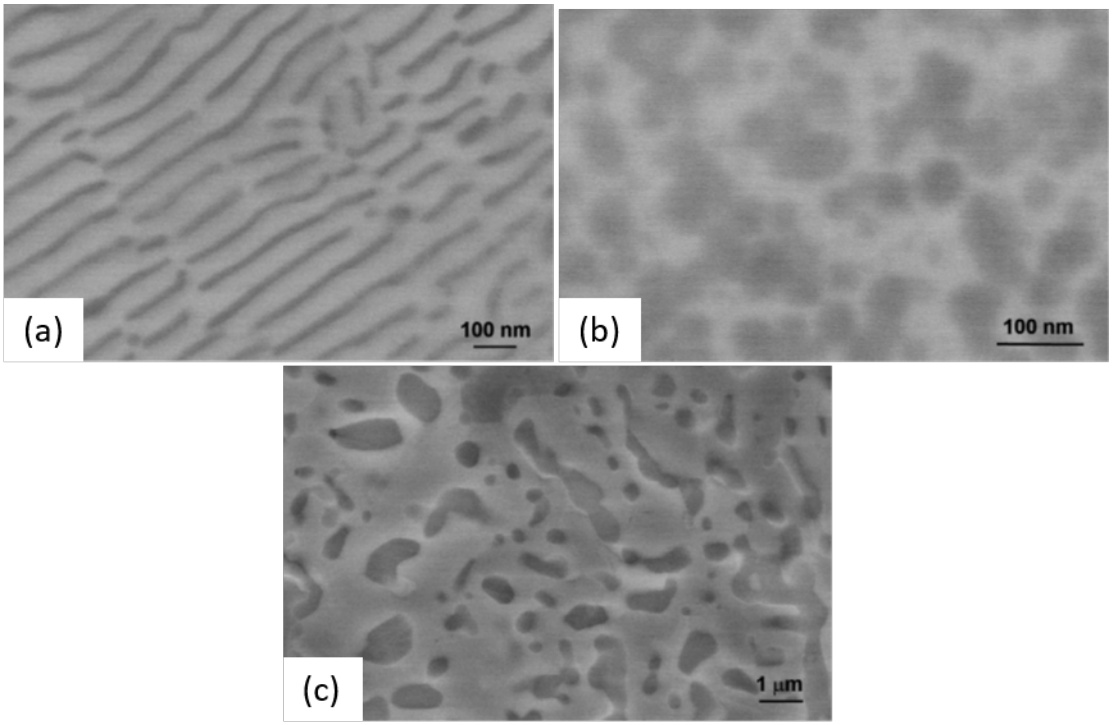

Figure 2.19: SEM backscattered images of (a) lamellar; and (b) spherical oxide particles in internally oxidized $Fe_{17}Y_2$ (700 °C for 3 days); as well as (c) substantially coarsened oxide particles in internally oxidized $Fe_{11}YTi$ (700 °C for 3 days) followed by annealing at 1000 °C for 1 day [88].

2.5.2.3 Combination of melt spinning and internal oxidation

Investigation of the combination of melt spinning and internal oxidation on ODS steel manufacture has not been reported to date. This combination has been studied by Nagorka et al.[60,89] for Cu alloys using oxides of Zn, Y and other rare earth elements that are insoluble in Cu.

Figure 2.20a shows a Cu-0.45Y melt spun ribbon with an obvious region of columnar grains (about 3 µm in width) on top of the refined equiaxed grains at the bottom chill zone, which gradually transitioned into larger equiaxed grains (approximately 10 µm) towards the top free side. The TEM image in Figure 2.20b shows a high number density of Cu-Y intermetallics smaller than 80 nm [60]. After internal oxidation at 750 °C for 64 h, oxide particles (Figure 2.20c) with a bimodal particle size distribution (5 – 10 nm and 50 – 100 nm in diameter) were formed in clusters that were present in approximately

similar sizes and spacings to the intermetallic phases in Figure 2.20b. There were also sparsely distributed nano-sized particles of ~ 10 nm throughout the material, but their number density was unhelpfully low [60]. In addition, there were internally oxidized precipitates throughout the thickness of the melt spun ribbons, reflecting a much better oxygen diffusion in the thin (approximately tens of μm) ribbons compared with bulk samples.

Instead of total dissolution and homogeneous distribution of Y into the Cu matrix, the melt spinning process resulted in the formation of a Cu-Y intermetallic phase, which was likely the precursor of the Y-O enriched particles formed in the following internal oxidation. However, since the intermetallic phase was refined to less than hundreds of nanometres and evenly distributed in the matrix, clusters of oxides of potentially beneficial sizes were formed via the combined melt spinning/internal oxidation (liquid metal) process. A brief milling for the ribbons before consolidation may to some extent break down the clusters, and yield better distribution of precipitates in the final bulk form, but excessive reliance on a milling step undermines the benefit of the melt route.

Overall, clustered oxides produced via liquid metal processing may not be as effective in dispersion strengthening as those produced from MA routes, but the processing route may nevertheless offer other advantages of higher processing throughput with less contamination. Therefore, the potential application of this processing route or others based on liquid alloy for the manufacture of ODS steels is worthy of further investigation.

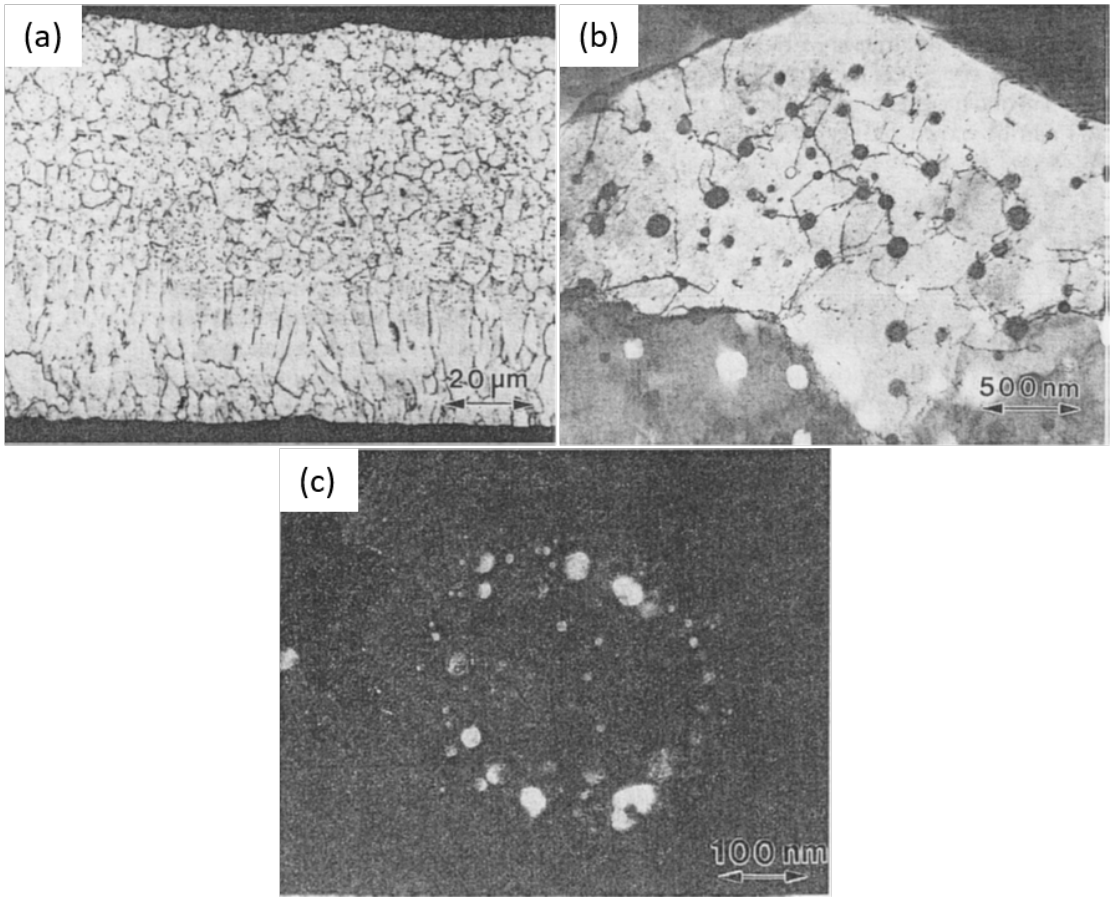

Figure 2.20: The microstructure of a Cu-0.45Y melt spun ribbon: (a) optical micrograph with wheel side at the bottom; (b) TEM micrograph taken near mid-thickness of the ribbon; and (c) bimodal distribution of oxides formed after internal oxidation at 750 °C and 64h [60].

2.6 Research objectives

The requirements for structural materials of future fission and fusion reactors is particularly demanding, which comprises low activation alloying constituents, high energy neutron irradiation resistance and high temperature mechanical properties.

As one of the most promising materials candidates, many investigations have been devoted to the Y-Ti-O enriched NP strengthened ferritic/martensitic steels, resulting in optimization of alloying composition, microstructure and performance.

Conventional MA-based processing of the ODS steels has proved to be effective in generating desirable high number density and acceptably uniform distributed NPs,

although problems such as prolonged processing times and scale-up limitations still remain, which prompts the desire to explore alternative processing routes.

This thesis focuses on development of two alternative processing routes for ODS steels, including (i) an 'evolutionary' reactive MA based processing and (ii) a 'revolutionary' melt spinning based processing.

The research objectives are summarised below.

For reactive MA based processing:

- To investigate potential benefits of using Fe-Y intermetallics instead of Y_2O_3 during MA on powder and consolidated alloy. This will be realised by a range of microstructural, microhardness and mechanical testing techniques.

For melt spinning based processing:

- To optimise manufacturing of Y-containing melt spun ribbons with gradually increasing processing capacity, reducing Y concentration (5 wt% to 1 wt%), introduction of Ti (1 wt%), and thorough microstructural analyses.
- To investigate the formation of Y-enriched oxide particles in melt spun ribbons via internal oxidation. This will be achieved by internal oxidation studies at 600 – 1200 °C with accompanying microstructural analyses.
- To establish manufacturing of bulk ODS steel from Y-containing melt spun ribbons through simultaneous consolidation and internal oxidation. This will be explored by a range of microstructural and microhardness testing techniques.

3 Processing

3.1 Introduction

The conventional processing route for ODS steels is a powder metallurgy process typically consisting of two major steps (section 2.4), in which the starting materials consisting of an Fe based matrix and a normally nano-sized Y_2O_3 powder are first MA'ed to produce a powder precursor, followed by consolidation into bulk materials using various techniques such as HIP, hot extrusion and more recently field assisted sintering technique (FAST)/spark plasma sintering (SPS) [7–12].

In this thesis, two alternative processing routes for the manufacture of ODS steels were explored to assess any potential benefits in mechanical properties and/or production throughput, and to what extent properties might be compromised in pursuit of higher throughput, improved consistency or possible cost reduction.

The first route was an 'evolutionary' modification to the conventional processing, in which Y_2O_3, the traditional source of Y, was replaced by Fe_3Y, an Fe-Y intermetallic, during the MA stage. The ball milled powder was then consolidated using HIP. The intention was that milling might be accelerated by the comparatively easy dissolution of the Fe_3Y (rather than Y_2O_3), and that either sufficient oxygen for oxides would in any case be incorporated, or would be provided by a sacrificial oxygen source.

The second route was a more 'revolutionary' approach, in which the whole MA stage was replaced by melt spinning of a dilute Fe-Y alloy. The melt spun ribbons were then pulverised into smaller flakes, blended with iron oxide (as an oxygen source) and consolidated into bulk using FAST, during which the Y would precipitate as Y_2O_3 via 'internal oxidation'.

This chapter describes in detail the chemical composition, raw materials, key equipment and their operating parameters for both routes.

3.2 Mechanical alloying based processing

3.2.1 Chemical composition

The composition of the ODS steel produced by MA was Fe-14Cr-3W-0.2Ti-0.25Y_2O_3 (wt%), and was chosen based on requirements including low radiation induced activity, high radiation damage resistance, desirable mechanical properties and a rich literature [29,62,90–92].

Cr promotes attractive mechanical properties, corrosion resistance, oxidation resistance and stabilizes the bcc ferrite structure, which performs better than other structures in resisting radiation damages such as volumetric swelling (see section 2.3) [7,49,93]. Cr also has lower radiation induced activity compared with other common ferrite stabilizers such as Al, Ni, Nb and Mo (see section 2.2). As shown in Figure 3.1, at 14 wt% Cr, single bcc α phase (ferrite) should be achieved since γ phase (austenite) and γ+α phase loops extending to 13.4 wt% at typical powder consolidation temperatures (1000 – 1200 °C) are avoided, while minimising the risk of forming brittle σ phase at higher Cr contents [7,29,90,94].

W provides solid solution strengthening with low radiation activity [7]. Systematic studies on the effect of tungsten concentration on ODS steels have shown that an increase in tungsten (2 – 3.5 wt%) increased tensile strength, ductile brittle transition temperature (DBTT), high temperature (up to 700 °C) creep rupture strength and the thermal stability of W in solid solution at a cost of reduced ductility and upper shelf energy, which was caused by formation of a brittle Laves phase [95,96]. It is generally considered that a compromise of 3 wt% is optimum.

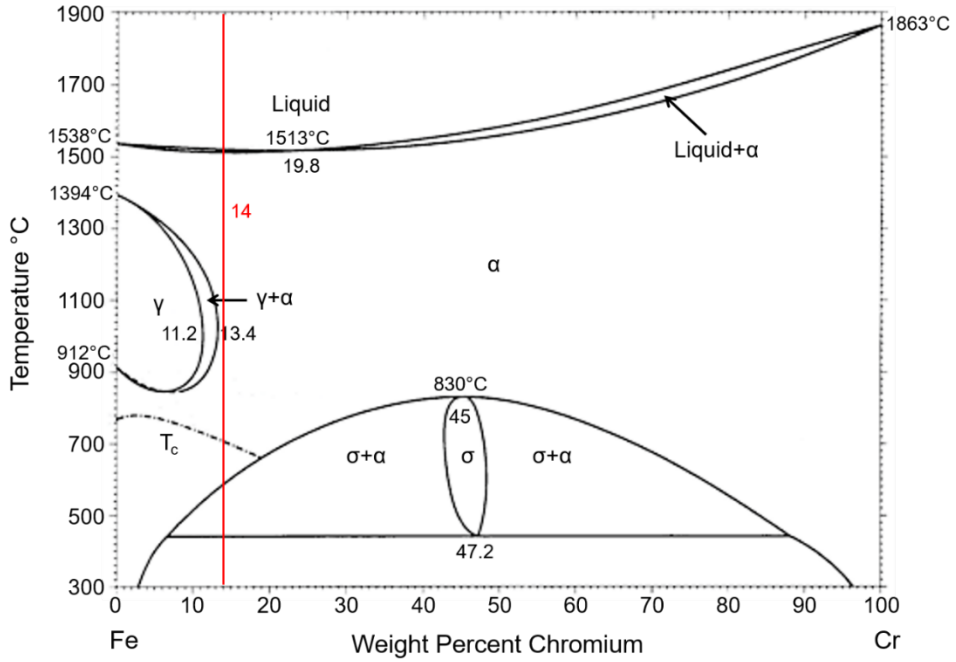

Figure 3.1: Fe-Cr binary phase diagram [94]

Y and O form the thermodynamically stable NPs that provide the dispersion strengthening and radiation damage resistance (see section 2.2). They are typically added in the form of nano-sized Y_2O_3 powder: an increase in Y_2O_3 contents from 0 – 0.56 wt% approximately doubled the ultimate tensile strength and high temperature (750°C) creep strength of an ODS steel at a cost of about 50% reduction in ductility [97]. The optimum Y_2O_3 fraction is generally considered to be approximately 0.25 wt% [21,29,62,80].

Ti refines the size of Y-rich particles, and thus increases their number density (see section 2.3), involving a change in composition of Y_2O_3 to more complex Y and Ti enriched oxides. Although various compositions can be found in the literature, the most commonly reported stoichiometry is $Y_2Ti_2O_7$ [58,98–100]. Hence, a near 1:1 atomic ratio between Y and Ti was chosen, *i.e.* 0.2 wt% Ti corresponding to 0.25 wt% Y_2O_3.

Then, based on this relatively well-studied 'baseline' composition, the intended 0.25 wt% Y_2O_3 was substituted by 0.57 wt% Fe_3Y so that the same Y concentration was preserved in the final alloy. The small amount of 'missing' O was assumed to be at

least partially available from the excess O known to be absorbed during handling and processing of mechanically milled powder [62,97].

Detailed specimen designations and chemical compositions are summarised in Table 3.1.

Table 3.1: Chemical composition and the corresponding designation of specimens produced by MA.

Specimen ID	Nominal composition (wt%)
14WT	Fe-14Cr-3W-0.2Ti
14YWT	Fe-14Cr-3W-0.2Ti-0.25Y_2O_3
14YWTa	Fe-14Cr-3W-0.2Ti-0.57Fe_3Y

3.2.2 Raw materials

The main constituent of all the alloys was gas atomised pre-alloyed Fe-14Cr-3W-0.2Ti (14WT) powder produced by Aubert and Duval, France by Ar atomisation, and sieved to < 150 μm. Detailed results of chemical and particle size analyses supplied by the manufacturer are listed in Tables 3.2 and 3.3 respectively. The 'undesirable' austenite stabilizers C, N and Ni were controlled to suitably low concentrations [93].

A cubic Y_2O_3 powder with diameters of 20 – 40 nm from PI-KEM Ltd or a gas atomised Fe_3Y chips with diameter < 2 mm produced by Nanoval GmbH & Co, Germany were used to achieve the 14YWT and 14YWTa compositions respectively.

Table 3.2: Chemical composition of 14WT pre-alloyed powder (wt%) [101]

Elements	C	Si	Mn	S	Cr	Ni	Mo	Co
14WT	0.008	0.167	0.350	0.003	14.040	0.024	<0.005	<0.010
Elements	**Ti**	**Cu**	**Nb**	**N**	**O**	**Fe**	**W**	**P**
14WT	0.238	<0.010	<0.005	0.009	0.008	81.50	3.030	0.004

Table 3.3: Particle size distribution of the 14WT pre-alloyed powder [101]

Range (µm)	< 25	25 – 50	50 – 63	63 – 80	80 – 100	100 – 125	125 – 150	> 150
wt%	12.26	20.16	23.11	16.51	13.66	9.25	5.05	0

3.2.3 Mechanical alloying

MA of the raw materials was carried out using a Fritsch Pulverisette P5 four-station planetary ball mill with 500ml milling vials and 10 mm diameter milling balls, as shown in Figure 3.2.

800 g of milling balls were used for each milling vial to achieve the recommended filling capacity as per the Fritsch operating manual [102]. Based on previous successful studies, a 10:1 ball to powder weight ratio was applied, giving a 80 g milling capacity per milling vial [10,29,62,91].

Efforts were taken in selecting suitable materials for the milling vials and balls to minimise risks of cross-contamination between milling media and materials, yet possessing sufficient hardness/wear resistance to avoid excessive erosion during the aggressive milling cycles. X210Cr12 tool steel and AISI 52-100 ball bearing steel (Acton Bright Steels Ltd) were selected for the milling vials and milling balls respectively. The chemical compositions of the two steels in Tables 3.4 and 3.5 respectively show that apart from a higher C concentration, concentrations of all other

elements in the milling media were below or at the same concentration as the 14WT pre-alloyed powder, ensuring cross-contamination effects were firmly under control.



Figure 3.2: Fritsch Pulverisette P5 four-station ball mill (right) and a steel milling vial loaded with steel milling balls (left).

The operating parameters for the ball mill were 250 rpm for 60h with 30 min pause (for cooling) per 1-hour milling and rotational direction reversion after each pause. The parameters were selected according to extensive optimisations carried out previously in the same research group for similar powders [62]. Powders were sampled at a number of different milling times to investigate changes throughout the milling process.

All materials handling including filling and discharging of powders was carried out in a Plas-lab 816-SS/GB/SP glove box filled with Ar (99.999 wt%, BOC) at a 50 mbar positive pressure to minimise O and N contaminations.

Table 3.4: Chemical composition of X210Cr12 steel used for milling vials (wt%) [103]

C	Si	Mn	P	S	Cr
2.2	0.1 - 0.4	0.2 - 0.6	< 0.03	< 0.03	12.5

Table 3.5: Chemical composition of AISI 52-100 steel used for milling balls (wt%) [103]

C	Si	Mn	Cr
1.0	0.1 - 0.6	0.35	1.5

3.2.4 Hot isostatic pressing

Hot isostatic pressing (HIP) was used as the consolidation method for the MA powders.

The HIP cans (cylinder with 20 mm in height and diameter) were custom made using mild steel with a central filling tube extending to about 25 cm in length. Each HIP can was filled with 75 – 80 g ball milled powders in the glove box, temporarily sealed and vacuum degassed at 500 °C for 4h. The filling tube was then permanently sealed off by double crimping 1 – 2 cm above the HIP can, as shown in Figure 3.3. HIP was carried out at 150 MPa, 1150 °C for 4h at Birmingham University. The temperature ramp up rate was 10 °C/min with a matching pressure ramp up rate. Cans were furnace cooled to room temperature. The HIP parameters were selected according to previous studies conducted by the group [62]. All alloys were HIPed in the same run to ensure the same processing history.

In summary, powder and alloy specimens of the MA based alternative processing 14YWTa were produced and studied using 14YWT and 14WT specimens with the same processing history as reference.

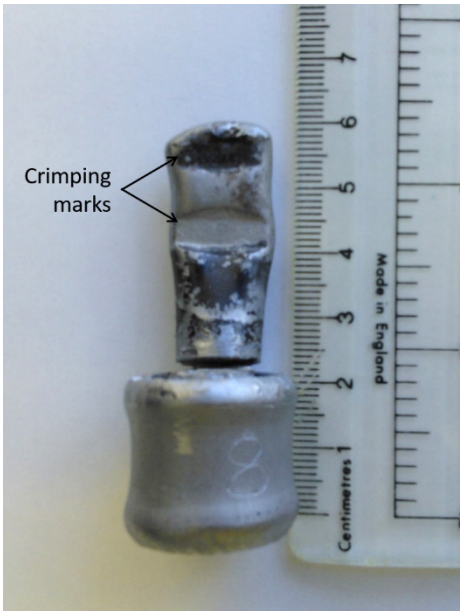

Figure 3.3: A 20 mm diameter and height HIP can in as-HIP form.

3.3 Melt spinning based processing

3.3.1 Chemical composition

Compared with the MA based processing, the first challenge for the melt spinning of ODS steels was the selection of feasible compositions.

The literature contained no prior work on melt spinning of relevant compositions for any Fe ODS alloy. Perhaps the closest research was ODS steel processing by internal oxidation of arc melted $Fe_{17}Y_2$ and $Fe_{11}TiY$ intermetallics [88]. However, the Y concentrations of these intermetallic compounds were at least 30 times higher than those typically (< 0.4 wt% Y) produced by MA [10,29,62,91,97].

Moreover, the possibility to produce an ODS Cu alloy using melt spinning, internal oxidation and hot extrusion from a vacuum induction melted Cu-0.45Y alloy was investigated by Nagorka et al. [60,104]. Nano-sized Y oxides (< 100 nm) were successfully formed after internal oxidation of the melt spun ribbons, although there were difficulties in achieving a homogeneous particle distribution [60].

Using the Fe-Y binary equilibrium phase diagram (Figure 3.4) as a reference, a Fe-5Y composition was selected as the starting point. At 5 wt% Y and at equilibrium, the

microstructure should comprise a majority of bcc α-Fe with limited Y solubility, and a dispersion of secondary $Fe_{17}Y_2$. Moreover, it was hoped that the rapid solidification experienced in melt spinning might lead to extended solubility of Y 'trapped' in the bcc α-Fe in a metastable solid solution, and a reduced fraction of $Fe_{17}Y_2$ or other metastable intermetallic compounds. The relatively high Y concentration was also chosen to make identification of any Y-based oxides easier, compared with the low fractions usually used in mature MA'ed materials. If this approach showed promise, more dilute alloys – closer to those more widely explored – might then be investigated.

Based on encouraging melt spinning and internal oxidation investigations using Fe-5Y, a Fe-1Y-1Ti composition was subsequently studied. Ti was also introduced at this stage to explore if its refining effect well-known in MA might be reproduced in the melt-based approach.

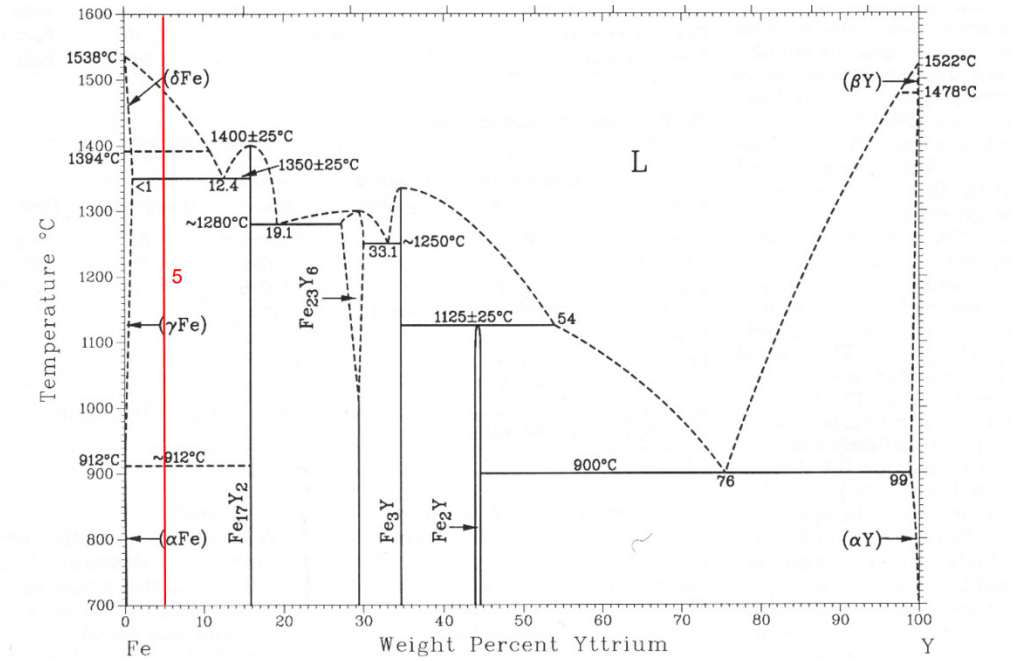

Figure 3.4: Fe-Y binary phase diagram [63]

3.3.2 Raw materials and master alloy production

Master alloy production was the first step for the melt spinning based processing. For the selected two compositions, master alloys were produced in three different ways using various raw materials and equipment, and presented significant challenges.

For Fe-5Y, the master alloys were produced by arc melting of high purity Fe (< 10 µm, 99.9%, Alfa Aesar) and Y (< 400 µm, 99.6%, Alfa Aesar) powder using a Lincoln Electric Idealarc R3R 500-I arc melting furnace (Figure 3.5a) with a water cooled Cu die. The raw materials were first cold pressed into billets at 10 MPa to prevent excessive powder scattering during melting. The furnace chamber was pumped to < $1x10^{-3}$ mbar, and refilled with 200 mbar He – 4% H_2 (99.999%, BOC) to provide a reducing atmosphere to minimise master alloy oxidation. The master alloy billet was flipped over and remelted three times to encourage homogeneous element distribution. Each master alloy billet was approximately 10 g in weight.

The same approach was applied to produce the first batch of Fe-1Y-1Ti master alloy billets with the addition of pure Ti powder (< 100 µm, 99.9%, Alfa Aesar).

A second batch of Fe-1Y-1Ti master alloy billets was produced from Fe (99.97%, Alfa Aesar), Fe-33.1Y (Goodwich) and Ti pieces (99.99%, Alfa Aesar) using a vacuum induction furnace with an alumina crucible at the Fraunhofer IFAM, Dresden, Germany to match the need for an increased melt spinning capacity. Instead of pure Y powder, presumably less reactive intermetallic Fe-33.1Y pieces were used in an attempt to reduce potential Y oxidation, since the acceptable margin for any loss of Y was much smaller than for the more concentrated Fe-5Y. Billets of up to 1 kg were produced.

A third and last batch of Fe-1Y-1Ti master alloy billets were produced from the same Fe, Fe-33.1Y and Ti pieces using a more modern Arcast Arc 200 arc melting furnace with a larger water cooled Cu die (Figure 3.5b). The intention was to further reduce master alloy oxidation by avoiding the use of an alumina crucible where O could be

drawn to react with Y during melting. The furnace chamber was pumped to < $1x10^{-3}$ mbar and re-filled to 200 mbar with high purity Ar (99.999%, BOC) before arc melting. The master alloy billet was flipped over and remelted three times to promote elemental uniformity. The billets were approximately 100 g.

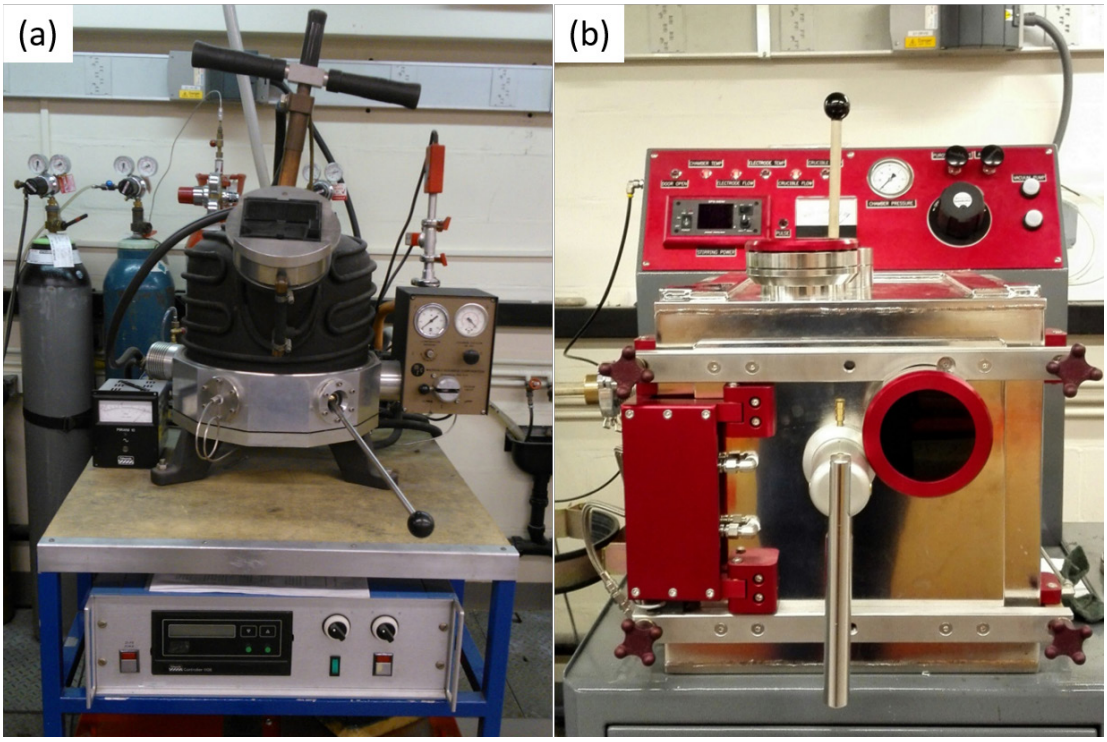

Figure 3.5: (a) Lincoln Electric Idealarc R3R 500-I and (b) Arcast Arc 200 arc melting furnaces

3.3.3 Melt spinning

Melt spinning of the master alloy billets was carried out on three melt spinners with progressively increasing processing capacity.

The Fe-5Y ribbons were produced using the melt spinner at the Department of Materials, Oxford University (Figure 3.6a). The process started with induction melting of a Fe-5Y billet in a BN crucible (BN7000, Kennametal Ltd.) at 200 mbar Ar pressure. The molten alloy was then ejected using a sudden 100 mbar ‘spike’ of Ar pressure through a spherical nozzle (1mm diameter) in the bottom of the crucible onto a polished Cu wheel rotating at a tangential velocity of 20 m/s and rapidly solidifying into 10 to 20

μm thick ribbons. Figure 3.6b shows a snapshot of the melt spinning of a Fe-5Y ribbon. The melt spinner chamber was pumped to $1x10^{-4}$ mbar and purged with high purity Ar gas three times prior to melt spinning. More than 6 g of ribbon was produced from a maximum crucible capacity of about 10 g.

The processing capacity was roughly doubled using a melt spinner at Shanghai Jiaotong University, Shanghai, China (Figure 3.7a) for the production of Fe-1Y-1Ti ribbons from the first batch of Fe-1Y-1Ti master alloy billets. Processing parameters including crucible material, nozzle geometry, Ar ejection pressure, Cu wheel tangential velocity and Ar protective environment were kept the same as those used at Oxford University to allow some inter-comparison. Figure 3.7b shows the melt spinner configuration for the production of Fe-1Y-1Ti ribbons.

The largest scale processing was carried out using the melt spinner at the Fraunhofer IFAM, Dresden, Germany (Figure 3.8a). Two batches of Fe-1Y-1Ti ribbons were produced from the second and third batches of Fe-1Y-1Ti master alloy billets. As shown in Figure 3.8b, the melt spinner shared a very similar configuration to those in Figures 3.6b and 3.7b. To achieve a higher throughput, the BN crucible (BN7000, Kennametal Ltd.) utilized a 2.3 x 0.6 mm slit nozzle (Figure 3.8c) at the bottom for faster molten alloy ejection, while the cooling wheel was made of a more durable CuCr1Zr alloy. After several trials, the Ar ejection pressure and cooling wheel tangential velocity were optimised to 100 mbar and 40 m/s respectively. Figure 3.8d shows the produced Fe-1Y-1Ti ribbons. Up to 100 g of ribbon could be produced from the maximum billet loading capacity of approximately 130 g.

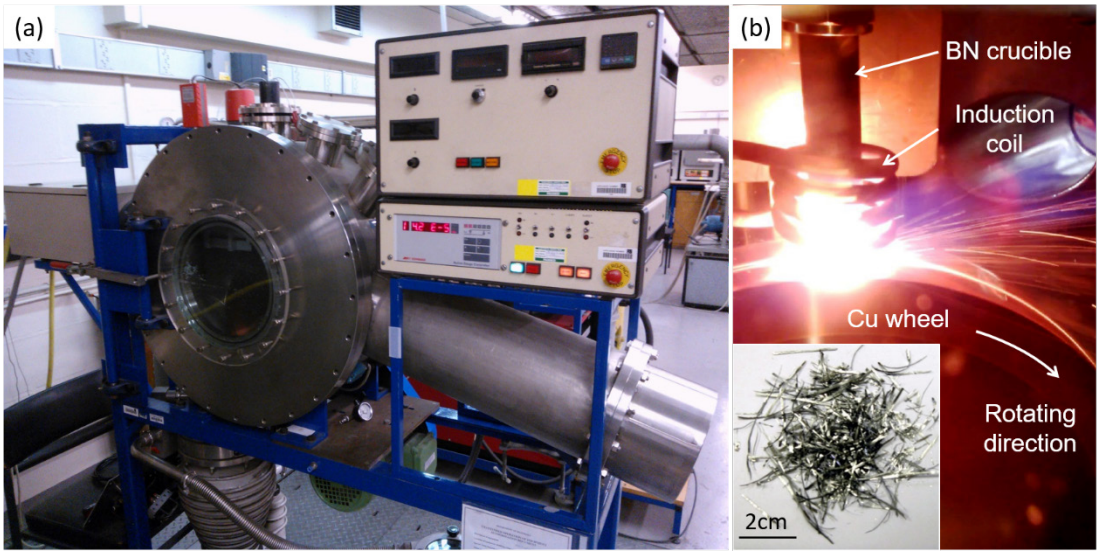

Figure 3.6: (a) Melt spinner at the Department of Materials, Oxford University; and (b) the production of Fe-5Y ribbons with produced ribbons in inset.

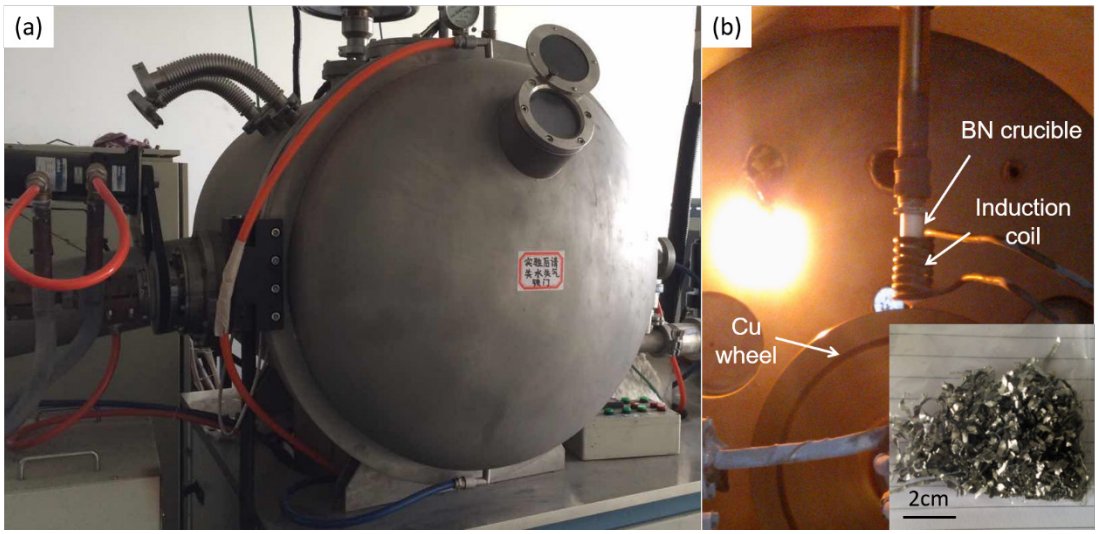

Figure 3.7: (a) Melt spinner at Shanghai Jiaotong University, Shanghai, China; and (b) melt spinner assembly for the production of Fe-1Y-1Ti ribbons with produced ribbons in inset.

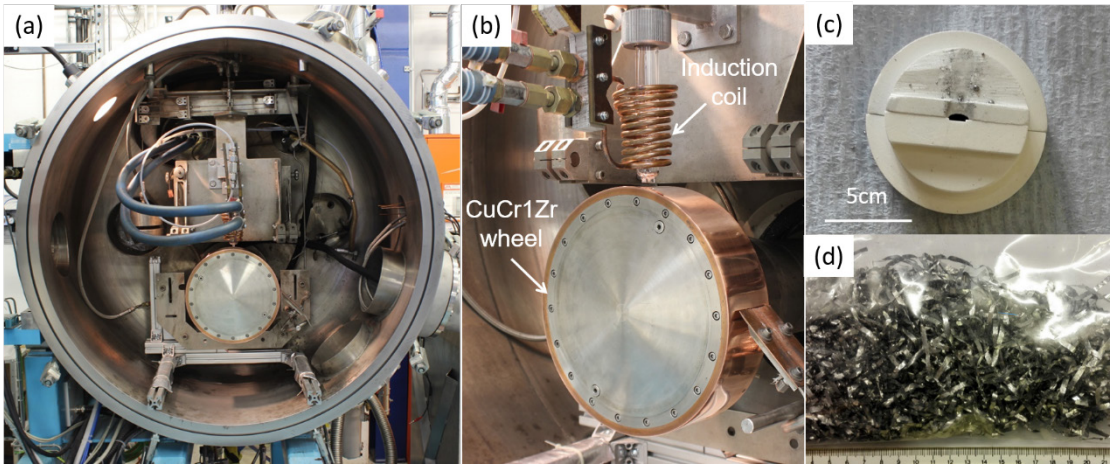

Figure 3.8: (a) Melt spinner at Fraunhofer IFAM, Dresden, Germany; (b) the melt spinner assembly, (c) detachable nozzle of BN crucible and (d) produced Fe-1Y-1Ti ribbons.

3.3.4 Internal oxidation

Before consolidating into bulk specimens, internal oxidation experiments on ribbons using the Rhines pack method [105] were carried out to investigate any formation of Y enriched oxides from supersaturated Y trapped by rapid solidification.

As shown in Figure 3.9, the melt spun ribbons were packed inside a quartz tube with Fe_2O_3 powder, separated by quartz fibre, pumped to vacuum (< $1x10^{-4}$ mbar), sealed and then heated to temperatures ranging from 600 – 1200 °C.

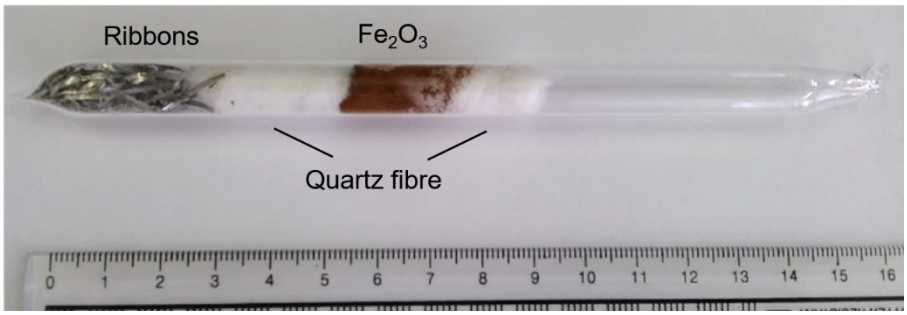

Figure 3.9: Fe-5Y ribbons sealed in a quartz tube ready for internal oxidation using the Rhines pack method [85,105].

3.3.5 Ribbon pulverization

Before consolidating into bulk specimens, the relatively long ribbons needed to be pulverized into smaller lengths to achieve better packing density.

As shown in Figure 3.10, ribbon pulverization was carried out using a Fritsch P6 Pulverisette one-station ball mill with an 80 ml zirconia milling vial and 100 g of 10 mm diameter zirconia milling balls. About 20 g of ribbons could be processed per milling run.

The ball mill was operated at 200 rpm for 2h, with 30 min pause per 15 min milling and a reverse of rotational direction after each pause. Compared with the operating parameters discussed in section 3.2.3, lower rotational speed, shorter milling time, smaller milling vial and less milling balls all resulted in much lower milling energy [18]. Therefore, the milling process could be categorized as pulverisation/blending rather than MA.

As shown in Figure 3.11, the Fe-1Y-1Ti ribbons were broken down into < 5 mm flakes after 1h milling, and the majority continued to reduce in size to < 1 mm powders after 2h milling, and a better packing density (by eye) was achieved.

To help promote oxidising the supersaturated Y and Ti in the ribbons in consolidated materials, 1.8 wt% Fe_3O_4 powder (99.5%, 15-20 nm, US Research Nanomaterials, Inc.) was blended in at this stage for one of the consolidated bulk specimens. The intention was that the Y and Ti might react with the Fe_3O_4 to form Y and Ti enriched oxides, leaving Fe that readily forms part of the ferritic majority ‘matrix’ phase.

Again, all materials handling was carried out in an Ar filled glove box to prevent unwanted ribbon oxidation.

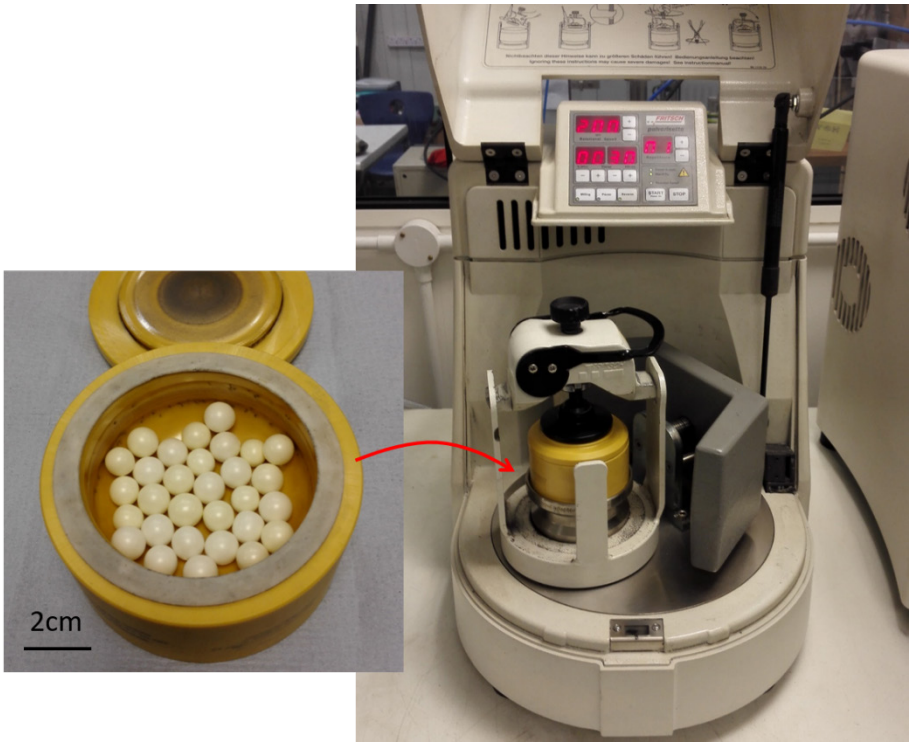

Figure 3.10: Fritsch Pulverisette P6 one-station ball mill (right) and a zirconia milling vial loaded with zirconia milling balls (left).

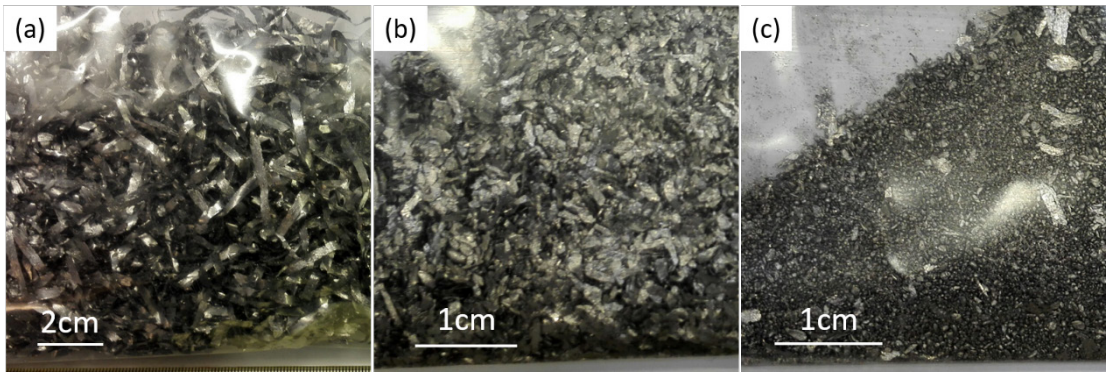

Figure 3.11: Fe-1Y-1Ti ribbons (a) in the as melt spun state; (b) after 1h ball milling; and (c) after 2h ball milling.

3.3.6 Field assisted sintering

As the last step of the melt spinning based processing, the pulverised ribbons were consolidated using a Dr. Fritsch DSP507 field assisted sintering (FAST) machine (Figure 3.12a) with a 20 mm diameter graphite die (Figure 3.12b).

To prevent excessive oxidation, the graphite die was filled in the Ar filled glove box and cold pressed at 10 MPa for 10 min, before transferring by hand to the FAST machine where a vacuum down to < $5x10^{-2}$ mbar was immediately applied.

The sintering was carried out at 1000 °C and 50 MPa for 30 min. A typical FAST process parameter history is shown in Figure 3.13. Note that the high temperature isothermal consolidation was achieved using carefully controlled direct current (up to 1.2 kA) at relatively low voltage (up to 4 V). Sintering carried out at lower temperature and pressure resulted in an unacceptable level of porosity.

Table 3.6 summarizes the specimens investigated by melt spinning-based processing.

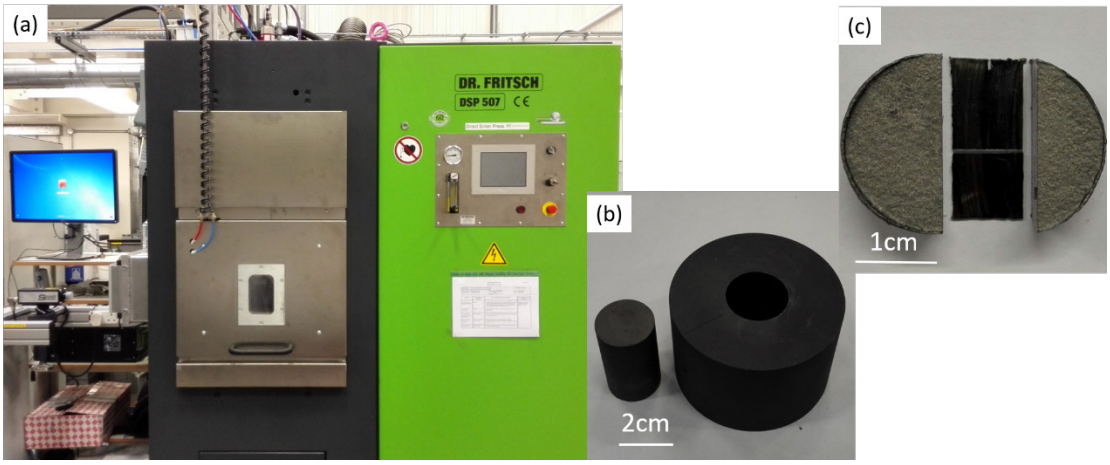

Figure 3.12: (a) Field assisted sintering (FAST) machine; (b) graphite die; and (c) produced bulk specimen with a slice taken from across a diameter.

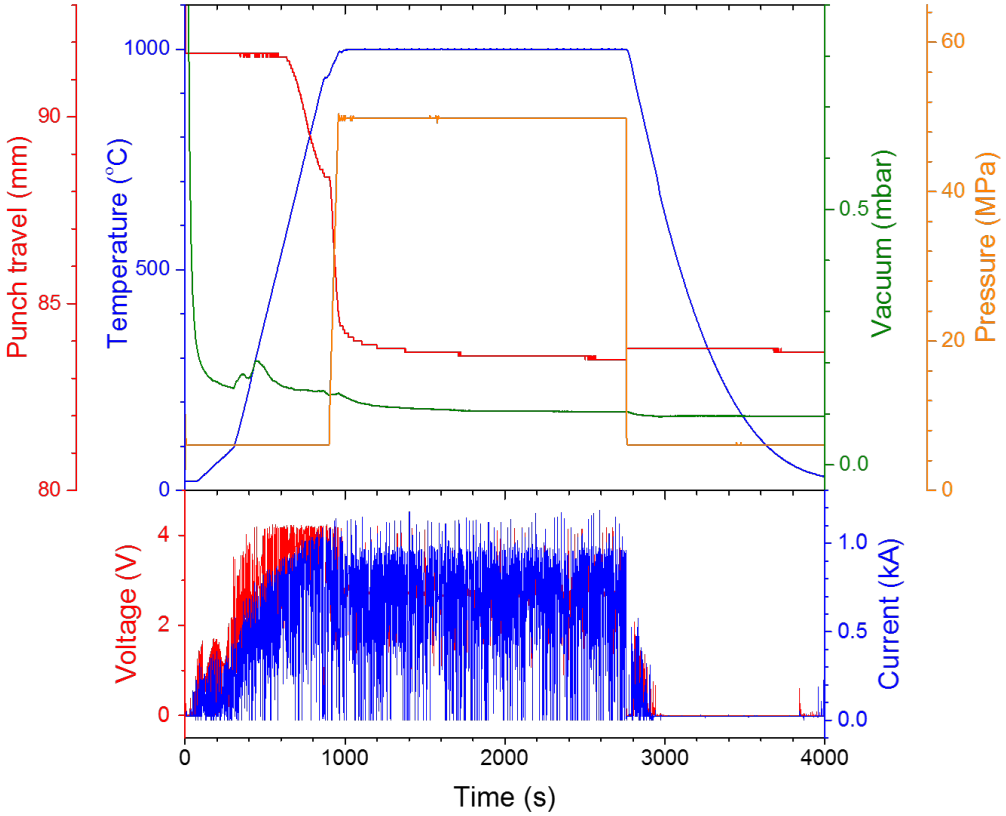

Figure 3.13: A typical FAST process showing variations in temperature, punch travel, vacuum, pressure, voltage and current with respect to time.

Table 3.6: Specimen designation with their corresponding nominal composition, processing history and raw materials of melt spinning based processing.

	Specimen ID	Nominal composition (wt%)	Processing	Raw materials
Master alloy	**MA01**	Fe-5Y	Arc melting	Fe and Y powder
	MA02	Fe-1Y-1Ti	Arc melting	Fe, Ti and Y powder
	MA03	Fe-1Y-1Ti	Vacuum induction melting	Fe, Fe-33.1Y and Ti pieces
	MA04	Fe-1Y-1Ti	Arc melting	Fe, Fe-33.1Y and Ti pieces
Melt spun ribbon	**MS01**	Fe-5Y	Melt spinning	MA01
	MS02	Fe-1Y-1Ti		MA02
	MS03	Fe-1Y-1Ti		MA03
	MS04	Fe-1Y-1Ti		MA04
Bulk alloy	**BA01**	Fe-1Y-1Ti	FAST	Pulverised MS04
	BA02	Fe-1Y-1Ti	FAST	Pulverised MS04 and Fe_3O_4 powder
	BA03	Fe-1Y-1Ti	FAST and annealing	Pulverised MS04 and Fe_3O_4 powder

4 Characterisation

4.1 Scanning electron microscopy

Scanning electron microscopy (SEM) based techniques were extensively used in this thesis for the microstructural characterisation of powders, ribbons and bulk specimens.

4.1.1 Imaging

Secondary and backscattered electron (SE and BSE) imaging that provides primarily topographical and compositional contrast respectively were used for investigation of microstructural features as the first step to judge if higher resolution or other more detailed and time-consuming characterisation techniques might be required [106].

Four SEMs were used, including a JEOL 840A operating at 20 kV and 10 mm working distance, a Zeiss EVO operating at 20 kV and 8.5 mm working distance, a JEOL 6500F with a field emission gun (FEG) operating at 15 kV and 8.5 mm working distance and a Zeiss Merlin with a FEG operating at 10 kV and 8.5 mm working distance.

Sample preparation for bulk specimens started with mechanical polishing using progressively finer SiC grinding papers up to grit 4000. The samples were then polished using 3 µm and 1 µm diamond suspensions on Nap polishing cloth (Struers), before moving onto colloidal silica suspension on Chem polishing cloth (Struers). Polished samples were stuck onto aluminium SEM stubs using silver dag.

Powder and ribbon specimens were first cold mounted using epoxy resin (SpeciFix-20, Struers), followed by the same polishing procedure described for bulk specimens. Polished samples were painted with an approximately 5 mm wide carbon band on sidewalls using carbon paint and coated on the top surface with a 15 to 20 nm carbon layer using a Cressington carbon coater to create a conductive passageway from top to bottom.

The same sample preparation procedures were applied for other SEM characterisation techniques described below.

4.1.2 Energy dispersive X-ray spectroscopy

SEM energy dispersive X-ray spectroscopy (EDX) was used to provide local compositional information by analysing the energy spectrum of characteristic X-rays emitted from interaction between the electron beam and sample surface [106].

For common standardless quantitative analysis, the weight fraction of elements is estimated by comparing X-ray intensity from the spectrum with calculated standard intensity derived from manufacturer standards adjusted with a correction matrix including beam penetration, sample absorption and secondary fluorescence [106,107]. Typical accuracy for EDX concentration measurement is approximately ± 2% for polished bulk specimen and ± 5% for particles and rough surfaces [106]. The accuracy is further reduced for light elements ($Z < 10$) due to strong specimen absorption of the relatively low energy characteristic X-rays [106]. Since X-rays are generated from relatively deep regions in the interaction volume, the spatial resolution for EDX analysis at common intermediate (15 – 20 kV) accelerating voltage is 1 – 5 μm^3 for light elements ($Z < 10$) and 0.2 – 1 μm^3 for heavy elements ($Z > 10$) [106,107].

SEM EDX scans were performed in the form of spot, area, line and maps using three different SEMs: JEOL 840A operating at 20 kV and 20 mm working distance, Zeiss EVO operating at 20 kV and 10 mm working distance and Zeiss Merlin with a FEG operating at 5 kV and 7.5 mm working distance.

4.1.3 Electron backscatter diffraction

SEM electron backscatter diffraction (EBSD) was used to analyse the orientation, size and distribution of grains. EBSD relies on indexing Kikuchi bands of electron backscattered diffraction pattern via a Hough transform, comparing it with a known

crystal phase and subsequently determining crystal orientation of the local area being scanned by electron beam [106,108].

SEM EBSD scans were carried out in the JEOL 6500F with an EDAX EBSD detector operating at 15 kV and 17 mm working distance. Samples were tilted 70° towards the detector for maximum detection efficiency. A 500 nm step size was used for coarse overview scans, while an 80 nm step size was applied for high resolution scans. For data processing, minimum confidence index and minimum number of points in a grain were set at 0.1 and 3. Grain boundaries were defined with a misorientation angle of > 15°.

4.1.4 Electron probe microanalysis

Electron probe microanalysis (EPMA) is an SEM with the electron beam current optimised for X-ray emission and analysis coupled with wavelength dispersive X-ray spectroscopy (WDX) to provide local chemical composition.

Compared with EDX above, WDX analyses the characteristic X-rays of a single specific wavelength rather than the whole spectrum, which provides superior energy resolution and consequently higher accuracy in measuring minor and trace (< 0.1 wt%) elements at the cost of longer scanning times [106].

A JEOL JXA8800 EPMA fitted with four WDX detectors was used, which operated at 15 kV and 30 nA. The detectors used a thallium acid phthalate (TAP) crystal for detection of W and Y, a lithium fluoride (LIF) crystal for Fe and Mn, and a pentaerythritol (PET) crystal for Cr and Ti. Each detector was calibrated for the elements of interest using standard specimens. Qualitative EPMA maps were carried out on a 204.8 µm x 204.8 µm area using 0.8 µm step size or a 51.2 µm x 51.2 µm area using 0.2 µm step size, while quantitative EPMA lines were performed along a 20 µm line using a 0.5 µm step size.

4.2 Transmission electron microscopy

Transmission electron microscopy (TEM) was applied for high resolution imaging, composition, phase and crystal structure analyses. The investigations were carried out using a FEG-TEM JEOL 3000F operating at 300 kV.

Among the various techniques, bright field (BF) imaging was carried out at relatively low magnifications (< 150,000x) to provide mass-thickness and diffraction contrast by selecting the direct beam using an objective aperture [109]. This simple and fast technique was also used to locate regions of interest for other more time-consuming TEM techniques.

In contrast with BF, dark field (DF) imaging was carried out by selecting a portion of the diffracted beams using an objective aperture [109]. Although dark field imaging also provides mass-thickness contrast, its diffraction contrast was primarily used in this study to investigate size and distribution of grains of polycrystalline specimens.

Selected area diffraction (SAD) was carried out by selecting an area of interest (200 to 500 nm diameter) in a BF or DF image using a SAD aperture [109,110]. In this study, SAD was primarily used to generate ring patterns from fine-scale polycrystalline regions for local phase and crystal structure analyses.

The crystal structure of individual nano-sized (< 20 nm) Y, Ti and O rich particles was characterised using high resolution TEM (HRTEM) at magnifications > 250,000x. The lattice images were Interpreted using Fast Fourier Transform (FFT) image simulation that were achieved using CrysTBox software [111].

In addition to parallel beam TEM, convergent beam scanning TEM (STEM) with a probe size of 1 nm was used to acquire high angle annular dark field (HAADF) images and to perform high resolution EDX composition analyses.

The STEM HAADF imaging provided atomic number (Z) contrast using high angle (> 50 mrads) scattering electrons via an angular dark field (ADF) detector [109]. Since the

Z contrast is unaffected by small variation in specimen thickness, compositional differences between Y, Ti and O enriched particles and Fe the in ODS steels were revealed. STEM HAADF imaging was used extensively to analyse size and distribution of the particles.

STEM EDX maps were obtained from regions of interest in STEM HAADF images to provide localised compositional information of refined (< 20 nm) Y, Ti and O enriched particles. STEM EDX adopts the same principle as an SEM EDX (described in section 4.1.2), but provides much higher resolution due to a considerably smaller interaction volume between a refined STEM probe and a very thin TEM specimen [109].

The TEM specimens were prepared based on FIB lift-out technique by Williams et al. [109] using a Zeiss Auriga FEG-SEM/FIB dual beam microscope.

Figure 4.1 illustrates the key steps of the FIB TEM sample preparation procedure. As shown in Figure 4.1a, a Pt protective coating was first applied on area of interest, followed by trenching using FIB (30 kV, 16 nA) on either side to leave a 2.5 µm thick specimen wall. The thin wall was further milled to approximately 1.2 µm thickness using lower FIB current at 4 nA and trimmed away at the sides, leaving a small supporting area on top corner as shown in Figure 4.1b. A probe manipulator was then moved to position and attached to the specimen wall using Pt deposition, before cutting off the final supporting area. The cut-off specimen was lifted out of the bulk sample using the manipulator and welded onto sample post of a Cu grid using Pt deposition, as shown in Figure 4.1c. After cutting off from the manipulator, a portion of the specimen was further milled to approximately 150 nm thickness using FIB at progressively smaller current from 1 nA to 50 pA. For final polishing and cleaning, the sample was tilted to 8° from the FIB axis and gently polished at reduced accelerating voltage (5 kV) and current (20 pA) for minimal surface damage and Ga contamination until electron transparent in the SEM at 5 kV, as shown in Figure 4.1d.

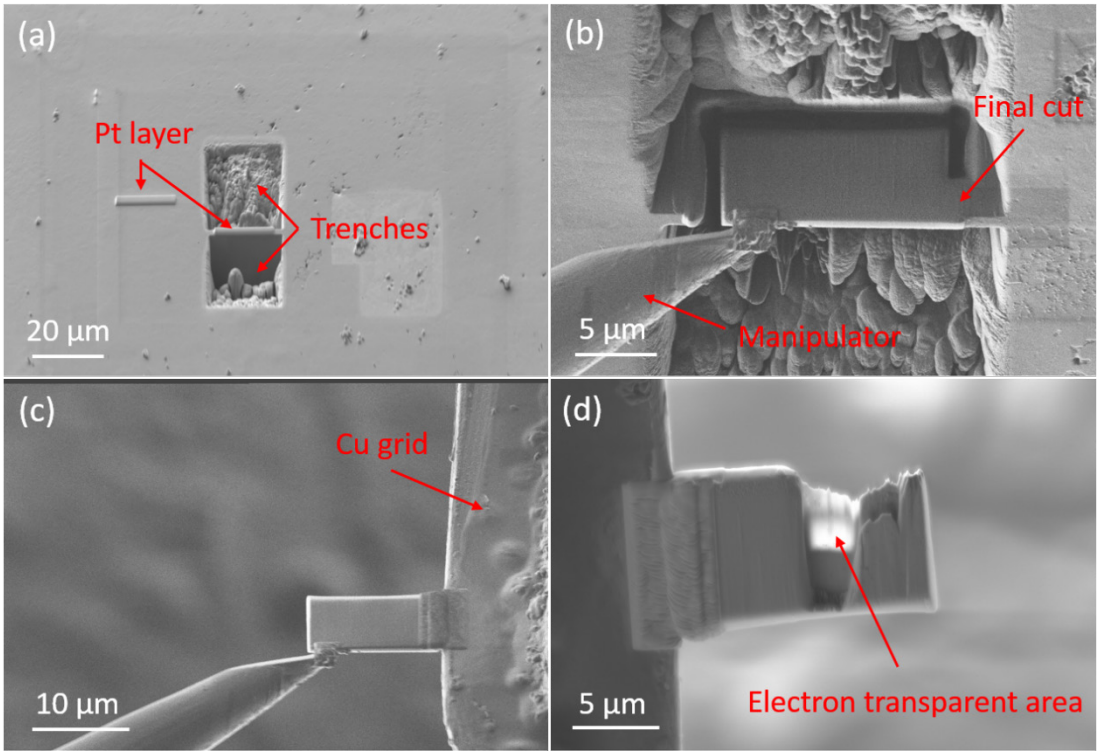

Figure 4.1: FIB TEM sample preparation procedure.

4.3 X-ray diffraction

X-ray diffraction (XRD) is used for phase identification and microstructural characterisation of crystalline materials based on Bragg's Law [36].

In this study, XRD investigations of powder and bulk specimens were carried out using a Siemens D5000 X-Ray Diffractometer, which operated at 40 kV and 30 mA using a Ni filtered Cu Kα radiation source with a wavelength of 0.154184 nm. Diffraction data was collected over a 2θ angle of 10° to 90° using a 0.05° step size.

Powder specimens were directly pressed onto sample holder to form a level surface, while bulk specimens were cut to approximately 1.5 mm thick pieces and mechanically polished to achieve a mirror surface using SiC grinding papers up to grit 2500.

Rietveld refinements were carried out by the least squares method to extract estimates of the crystallite size and micro-strain from peak shape, position and intensity of the XRD scans. The Rietveld refinements were performed using Maud software [112].

4.4 Powder size distribution

The size and distribution of ball milled powder particles were analysed using a Malvern Instruments Mastersizer 2000. The instrument measures the radial intensity of light scattered by dispersed powder particles passing through a laser beam and calculates the size of the particles according to Mie theory [113,114].

For each experiment, up to 5 g of powder was added and suspended in deionised water at the sample dispersion unit until reaching the recommended 10% scattering density. Sonication was applied 1 min prior to and during the measurements to break up and prevent powder agglomeration. In the analysis, a refractive index of Fe (2.86) was assumed as a close approximation for the ODS steel powders, and the size of the irregular shaped powder particles were modelled and calculated as spherical particles with equivalent volume [114]. Ten measurements were taken for each powder specimen with results then summed and normalised to provide a representative size distribution.

The laser scattering based Mastersizer 2000 provided more reliable powder size and distribution information due to a much larger sampling volume compared with microscopy based techniques such as SEM, but relies on the assumption of powder sphericity.

4.5 Vickers microhardness

Microhardness is a measure of a material's resistance to localized plastic deformation and has a linear correlation with yield strength for most materials [115]. The Vickers microhardness number (HV) is given by [115]

$$HV = \frac{1854.4P}{D^2} \qquad (4.1)$$

where P is the applied load in g and D is the mean diagonal length of the resulting pyramidal indentation in μm.

A Wolfson Instrument 402MVD microhardness tester with a diamond indenter was used to measure the hardness of powder specimens. The powder samples were prepared using the same procedure as discussed in section 4.1.1. Tests were carried out using 25 g load and 20 s dwell time. Ten measurements were carried out for each powder specimen. The relatively small testing load was selected so that the plastic zone was fully contained within even small (~ 20 μm) powder particles. The diagonal length of the indents was kept to below a third of the powder particle diameter.

A high temperature microhardness tester with a sapphire indenter was used to measure the hardness of bulk specimens at temperatures up to 700 °C. The samples were prepared using the same procedure described in section 4.1.1 and mounted on alumina stubs using silver dag. Tests were carried out using a 200 g load with 20 s dwell time at < $1x10^{-4}$ mbar vacuum. Seven measurements were performed for each specimen.

4.6 Four-point bending

Four-point bending tests were carried out using an Instron 3366 universal testing machine with a custom built molybdenum testing jig.

As shown in Figures 4.2 a and b, the load applied from the universal testing machine was transferred through a loading rod to the testing jig and distributed to the specimen by four rollers, which put the specimen into a four-point bend with maximum tensile stress and strain on the notched lower surface.

The maximum tensile stress for a specimen as shown in Figure 4.2b can be calculated from: [116]

$$\sigma = \frac{Pdl_1}{4I} \qquad (4.2)$$

where P is the total load, d is the specimen thickness, l_1 is the distance between inner and outer roller and I is the second moment of area. For a specimen with rectangular cross section, I is given by:

$$I = \frac{wd^3}{12} \tag{4.3}$$

and w is the specimen width. Hence,

$$\sigma = \frac{3Pl_1}{wd^2} \tag{4.4}$$

The maximum strain at the notched lower surface could be calculated from: [116]

$$\varepsilon = \frac{3dD}{2l_1(l_1 + 3l_2)} \tag{4.5}$$

where D is the displacement of the loading rod and $2l_2$ is the distance between the two inner rollers.

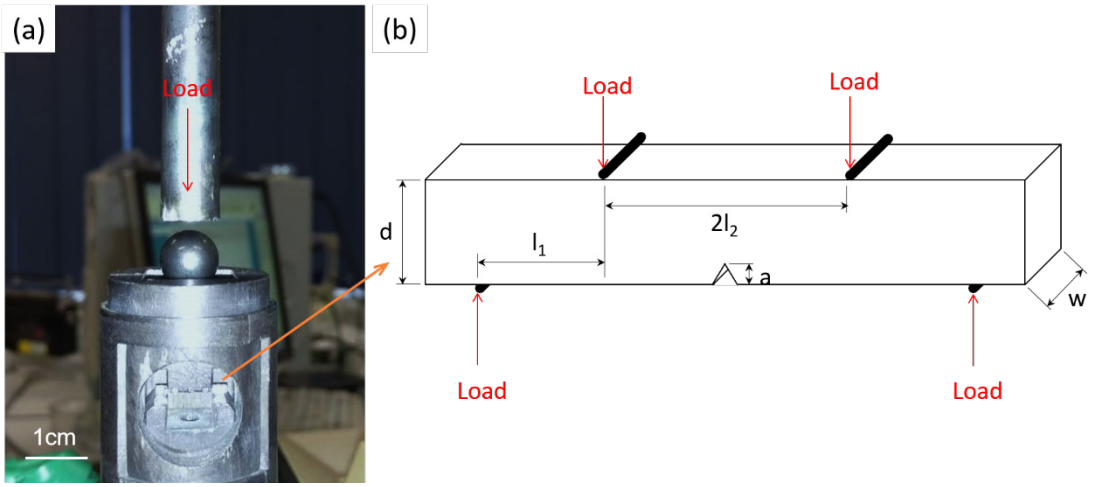

Figure 4.2: Four-point bending (a) molybdenum testing jig; and (b) schematic illustration of specimen geometry and loading configuration.

Test specimens were cut to 12 mm x 1 mm x 1 mm matchsticks using electrical discharge machining (EDM) and mechanically polished using SiC grinding paper to grit 2500. As shown in Figure 4.3, a 200 μm depth notch was then placed at centre of each test specimen using EDM and checked by SEM imaging.

Tests were carried out at a constant strain rate of 3.3 x 10^{-5} s^{-1}, which was converted to loading rod displacement velocity and adjusted for small variations in specimen geometry for each specimen using equation 4.5. A 4 N load was applied before each test to achieve a tight fit from the loading rod to the specimen and prevent potential slip. Load and displacement data were converted to stress and strain for analysis via equations 4.2 and 4.5.

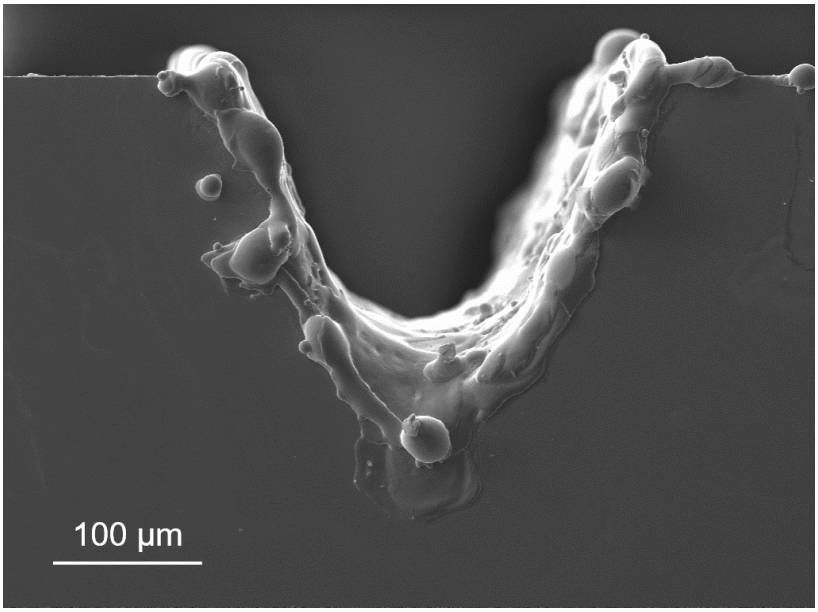

Figure 4.3: A 200 µm depth notch on four-point bending test specimen.

5 Mechanical alloying based processing

5.1 Introduction

The use of 20 – 50 nm sized Y_2O_3 powder added to Fe-based alloy powders as the starting materials for MA of ODS steels is well established [7–12].

Although alternative oxides/oxide formers, such as MgO, Ce_2O_3, La_2O_3, ZrO_2 and Hf, have also been studied, and sometimes have shown the potential for improving, for example, the fracture toughness of the ODS steels, they ultimately have failed to deliver the same level of dispersion strengthening as the Y enriched nano-sized complex oxides that forms from the Y_2O_3 powder in MA and subsequent consolidation and thermo-mechanical processing [53,62].

Fe-Y intermetallics, such as Fe_2Y and Fe_3Y, have been recognized as potential substitutes for Y_2O_3 that can still give rise to the critical strengthening Y-rich oxides by 'internal oxidation', but might also provide benefits of higher oxide particle density and high temperature strength by avoiding excess residual oxygen in solution [6].

The number of studies relating to Fe-Y additions are relatively small and there remains some controversy of any benefits when compared with Y_2O_3. Brocq et al. reported similar dissolution characteristics between Fe_3Y and Y_2O_3 during MA through EPMA, small angle neutron scattering (SANS) and atom probe tomography (APT) analyses [16,55]. The results were in accordance with Williams et al.'s investigation, which showed a virtually identical size distribution and number density of Y and Ti enriched nano-sized oxides between Fe_2Y and Y_2O_3 additions in ODS steels using TEM and APT characterisation [53]. Nevertheless, Oksiuta et al. reported finer and more densely distributed nano-sized oxides in Y_2O_3 ODS steel compared with Fe_2Y ODS steel using TEM analysis, which led to a lower hardness and better fracture toughness of the Fe_2Y ODS steel [17]. Arguably, all the key insights, whether encouraging or not, have been using TEM and APT that interrogate only relatively small sampling volumes. In addition,

the H_2 milling environment applied by Oksiuta et al. [17] resulted in O concentrations less than half of those required to fully oxidise Y and Ti in the Fe_2Y ODS steel, which may partially contribute to the property variations.

This chapter describes a comparative investigation between 14YWTa (containing Fe_3Y) and 14YWT (containing Y_2O_3) powders and steels produced using the same MA and consolidation parameters, intended to isolate the use of Fe_3Y or Y_2O_3 in the starting material as the only variable causing variations both in powders and consolidated steels. Characterisation of the powders was carried out throughout the MA process, as well as on final consolidated steels, to elucidate the microstructural and chemical evolution in the two stage ODS steel processing. Significant effort was expended in ensuring that key insights were based on representative sampling area/volumes.

The powders were ball milled for 60h using a Fritsch P5 ball mill, and then HIP'ed into bulk alloys at 1150°C for 4h. Detailed composition and processing parameters were already provided in section 3.2.

5.2 Mechanical alloyed powder

The microstructural evolution of 14YWTa and 14YWT powders during MA were investigated and compared in aspects of particle size distribution, morphology, hardness, microstructure and element distribution.

5.2.1 Particle size distribution and morphology

The particle size distributions of the 14YWTa and 14YWT powders were measured after 1, 4, 8, 15, 30, 45, and 60h of ball milling based on procedures detailed in section 4.4.

Figures 5.1a and b show the use of Fe_3Y in 14YWTa instead of Y_2O_3 in 14YWT affected early stages (< 4h) of milling behaviour where coarser (> 500 μm) particles comprised much higher volume fractions. This was probably caused by the substantially larger initial size of the 1 – 3 mm Fe_3Y chips in 14YWTa compared with the 20 – 40 nm Y_2O_3

powder in 14YWT. The larger Fe_3Y chips were in general slower to comminute and disperse well into the powder blend in the early stages of processing, whereas the Y_2O_3 powder was already at the nano-scale. Nevertheless, after 8h, the 14YWTa powder transitioned to a uni-modal particle size distribution that was similar to the 14YWT powder. Indeed, as shown in Figure 5.1c, the two powders then showed comparable trajectories in particle size evolution, both approaching a steady-state distribution at 30h after the rapid, initial size reductions. Overall, Fe_3Y or Y_2O_3 had a similar influence on the overall time required to achieve the dynamic balance between cold-welding and work hardening/fracturing for powder particles that defines the steady-state regime [18].

Figure 5.1c shows the reducing difference in the volume median diameter between the 14YWTa and 14YWT powders stopped after 30h milling, leaving a constant but small variation of approximately 6 μm when both powders were at their steady-states in particle sizes. Although the difference is small and likely close to the resolution of the technique, it may be that there is a different saturation point of strain energy and dislocation density between the two powders, possibly due to the reduced O concentration and weaker chemical bonding in Fe_3Y compared with Y_2O_3.

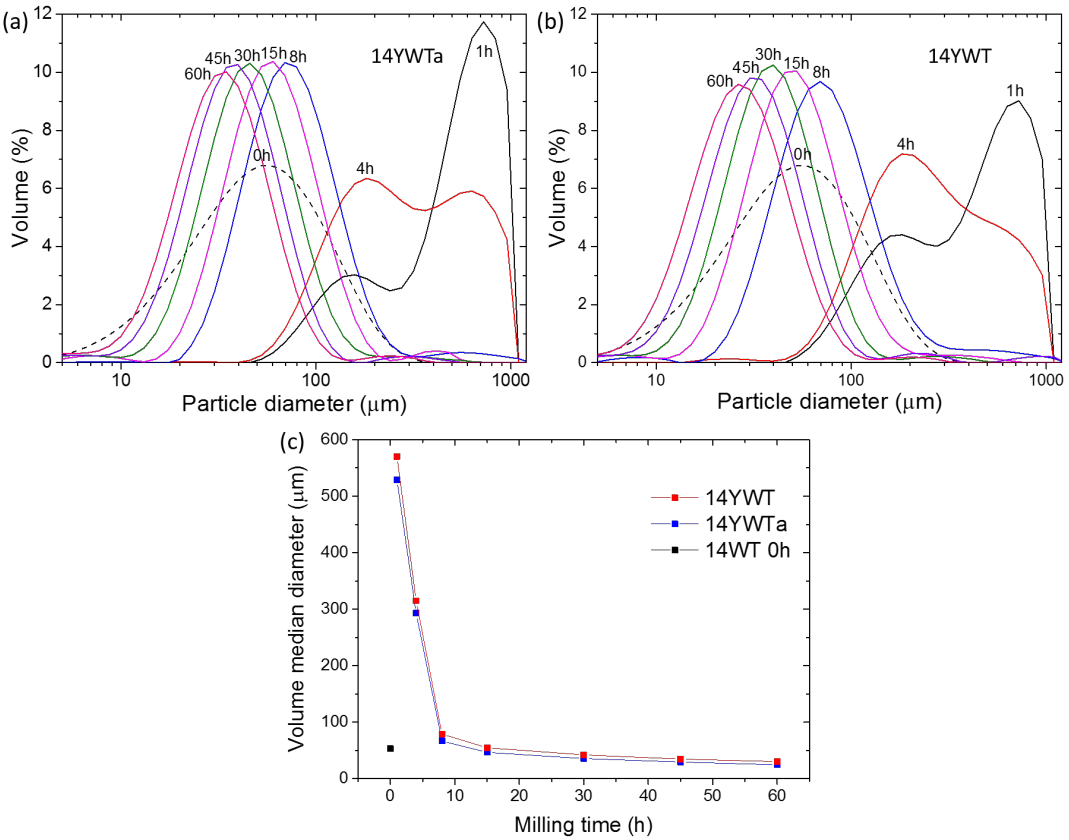

Figure 5.1: Evolution of particle size distributions during ball milling for (a) 14YWTa and (b) 14YWT powders with their D50 volume median diameters in (c). The 0h dashed lines in (a) and (b) refers to the as-received 14WT pre-alloyed powder.

The 14WT pre-alloyed powder, Fe_3Y chips and 14YWTa powder at different stages of milling were imaged in the SEM, based on the procedures detailed in section 4.1.1.

There was a significant increase of particle size after 1h milling (Figure 5.2c) from the gas atomised 14WT powder (Figure 5.2a), with a significant morphology change from spherical to flattened, which is typical for powder particles after early stages of milling [117]. The mm-sized Fe_3Y chips (Figure 5.2b) were rapidly reduced in size with no trace of the original morphology after the first hour of milling, suggesting the Fe_3Y chips might be suitable for MA even though it was initially much coarser than the Y_2O_3. With an increase of milling time from 4h to 60h (Figures 5.2d – f), the particle size of 14YWTa powder progressively reduced and the shape gradually transitioned from flattened to equiaxed, which was again consistent with typical MA powders [18,117].

The SEM images in Figures 5.2c – f suggest that particle sizes of the 14YWTa powder were in broad agreement with those measured by laser scattering, and as previously summarised in Figure 5.1a.

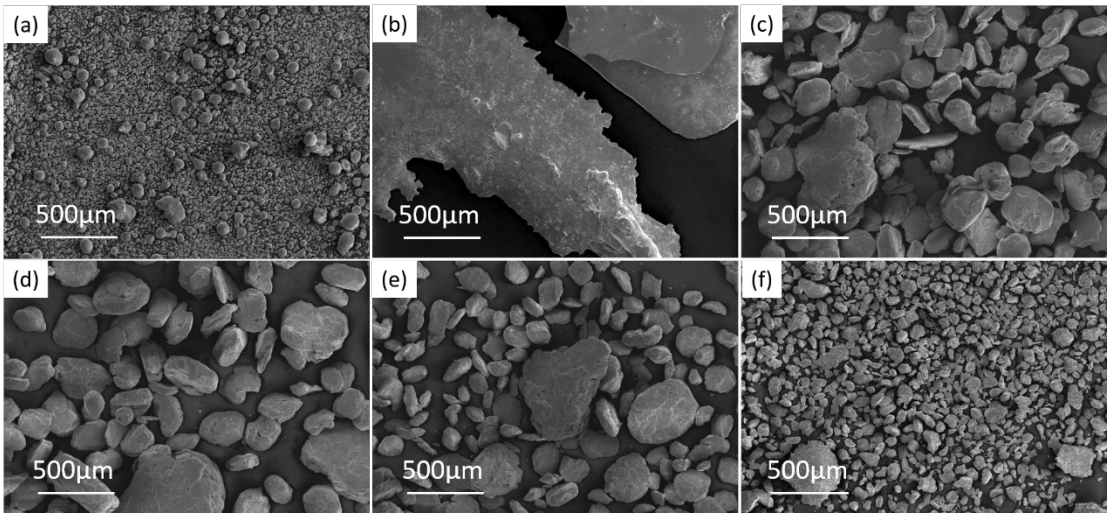

Figure 5.2 SEM micrographs for (a) 14WT pre-alloyed powder; (b) gas atomised Fe_3Y chips; (c) 1h milled; (d) 4h milled; (e) 15h milled; and (f) 60h milled powders.

5.2.2 Microhardness

The Vickers microhardness of the 14YWTa and 14YWT powders were measured based on procedures detailed in section 4.5.

As shown in Figure 5.3, the two powders shared similar plots of microhardness against milling time, with hardness increasing rapidly from the starting 14WT (black symbol) powder in the early stages of milling, followed by progressively reducing increases before both hardness reached plateaux at approximately 1000 kg/mm^2 after 30h milling.

The similarity of microhardness of 14YWTa and 14YWT powders, as well as other ODS steel powders of similar compositions and processing parameters [12,62,118], indicated the replacement of Y_2O_3 by Fe_3Y in the starting materials did not significantly affect the overall times required to achieve saturation of work hardening in powder particles, although a steady hardness discrepancy of approximately 20 kg/mm^2 between the two powders after 30h milling might suggest a subtle difference in the

exact saturation points, which might be expected if the Y additions and O concentrations are in different forms in the Fe_3Y and Y_2O_3 variants.

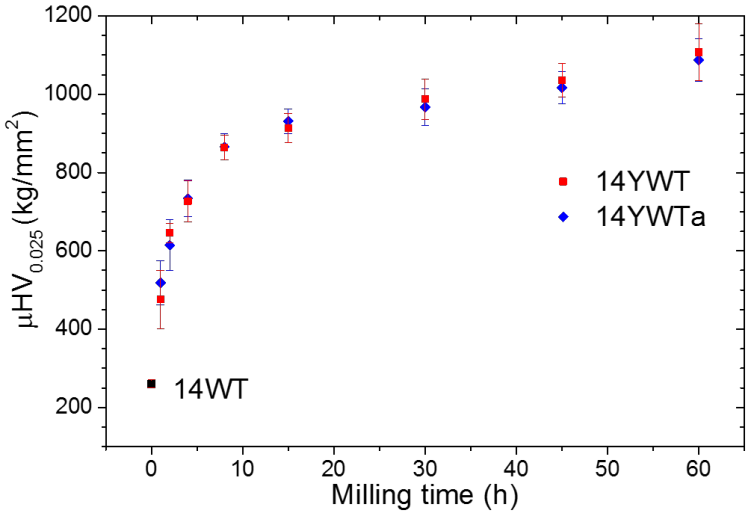

Figure 5.3: Microhardness of 14WT (black) pre-alloyed powder, as well as 14YWTa (blue) and 14YWT (red) powders after 1, 2, 4, 8, 15, 30, 45 and 60h milling.

5.2.3 XRD

XRD measurements and Rietveld refinements were carried out on MA 14YWTa and 14YWT powders based on procedures detailed in section 4.3.

Figures 5.4a and b show the 14YWTa and 14YWT powders had comparable XRD traces throughout the milling process. Only the (1 1 0) and (2 0 0) peaks of bcc Fe (PDF: 00-006-0696) are shown on these traces and all other peaks behaved similarly. The milling procedure for Fe_3Y and Y_2O_3 additions refined/dispersed both to below the detection limit on this instrument after only 1h of milling. The peaks were broadened and shifted with increasing milling time due to the well-known effects of decreasing crystallite size and increasing lattice strain in MA powders from accumulation of defects and work hardening during ball milling [18].

Consistent with XRD traces, variations in crystallite size and lattice strain for 14YWTa and 14YWT in Figures 5.4c and d were similar. Crystallite size in the 14YWTa and 14YWT powders both decreased from approximately 250 nm to 25 nm, while lattice

strain of the two powders increased to approximately 0.5% as milling time increased to 60h. Both parameters approached a near steady-state after 30h. The XRD results were in good accordance with XRD results for ODS steel powders of similar composition and processing parameters [118,119].

Overall, the similarities between 14YWTa and 14YWT may suggest lattice strain due to work hardening dominates over strain due to breakdown of the Fe_3Y or Y_2O_3 additions and the incorporation of Y and/or O in the defective ferrite lattice.

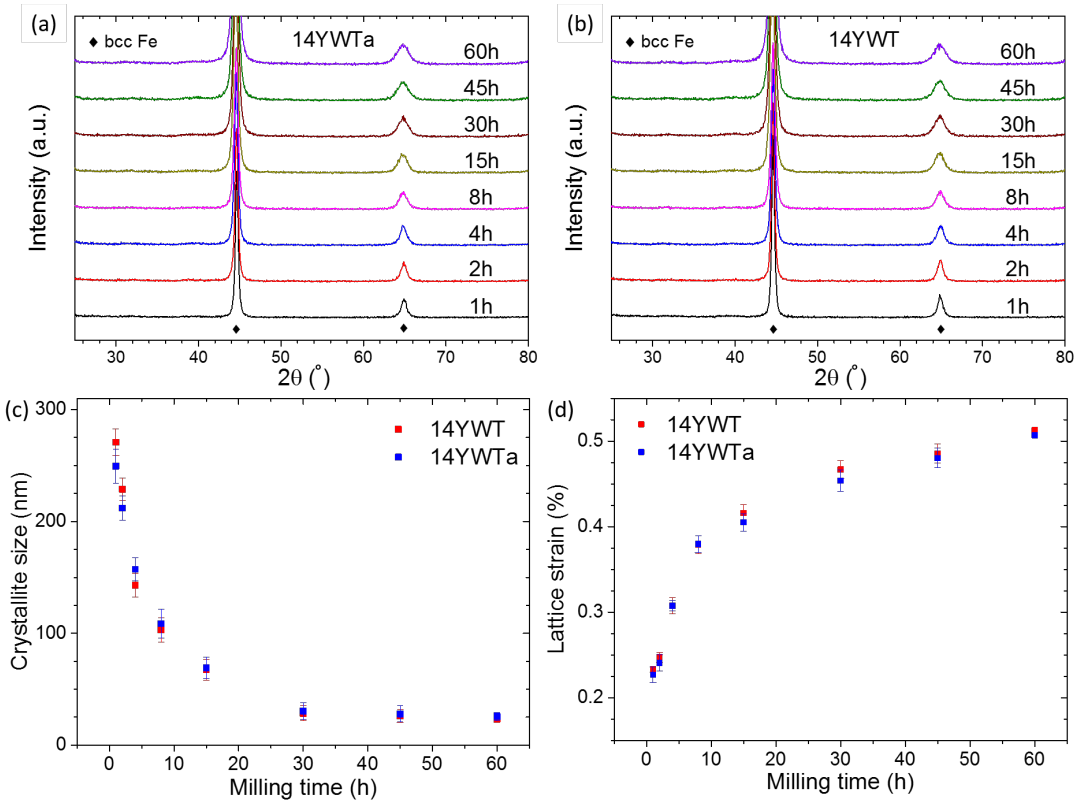

Figure 5.4: XRD measurements of (a) 14YWTa and (b) 14YWT powder particles after 1, 2, 4, 8, 15, 30, 45 and 60h milling, with their estimated (c) crystallite size and (d) lattice strain plotted as a function of milling time.

5.2.4 TEM

TEM investigations were carried out on 60h milled 14YWTa and 14YWT powders using procedures detailed in section 4.2 to further explore the phase chemistry and to obtain further microstructural information.

Figures 5.5a and d show SAD patterns of the 60h milled 14YWTa and 14YWT powders that contained only diffraction rings due to bcc Fe (PDF: 00-006-0696), which was consistent with the XRD results in Figures 5.4a and b. No residual discrete regions of Fe_3Y and Y_2O_3 were found and if present were below the SAD detection limit.

Both 14YWTa and 14YWT powders had a nanocrystalline microstructure, which is shown in the representative DF TEM images in Figures 5.5b and e, with similar average grain sizes of 22 nm and 19 nm respectively (Figures 5.5c and f), based on measurements of more than 100 grains for each sample.

The area weighted grain sizes (D_A) measured by TEM were in good agreement with the volume weighted (D_V) crystallite sizes from XRD measurements according to the equation $D_v = \frac{9}{8} D_A$ [120].

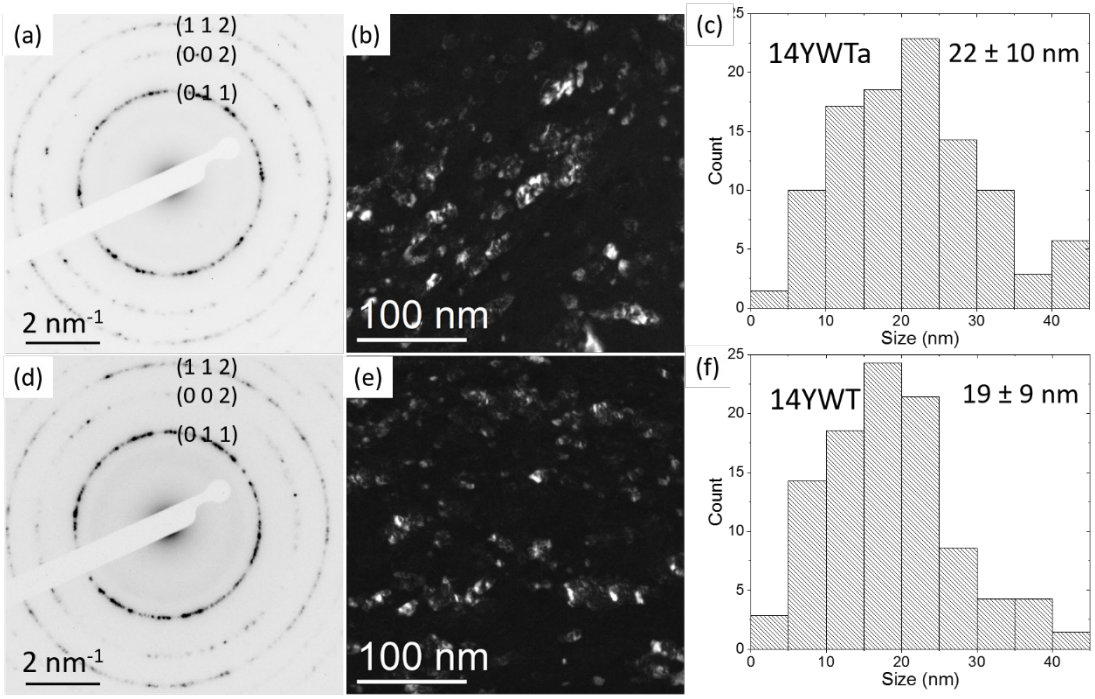

Figure 5.5: TEM microstructural analyses for 14YWTa and 14YWT powder particles after 60h milling, including (a) SAD pattern, (b) DF TEM image and (c) grain size histogram of 14YWTa; and (d) SAD pattern; (e) DF TEM image and (f) grain size histogram of 14YWT.

5.2.5 EPMA

Qualitative EPMA maps and quantitative EPMA line scans of pre-alloyed 14WT and 2, 8, 30 and 60h milled 14YWTa and 14YWT powders were used to investigate and compare the distributions of key elements at different stage of MA. The measurements were conducted based on procedures detailed in section 4.1.4.

Figures 5.6a – c show EPMA maps of the starting 14WT gas atomised powder with relatively uniform distributions of Fe, Cr and W, while Ti displayed point concentrations of brighter contrast in Figure 5.6d, predominantly in inter-dendritic or grain boundary regions of the 14WT particle, based on channelling contrast of the corresponding BSE SEM image in Figure 5.6e [106]. Assuming that the Ti in the enriched regions was not entirely insoluble (i.e. due to the formation of TiN etc.), it appeared that MA broke-up/dissolved these regions, so that a more uniform distribution of the strengthening Y and Ti enriched oxides might be formed after consolidation [12].

The concentrations of Ti, Cr and W in the 14WT particle were measured along an EPMA line-scan of 20 μm. As shown in Figure 5.7, Cr and W concentrations remained relatively steady with means of 14.4 wt% and 2.8 wt%, and standard deviations below 1% and 3.5% respectively. Ti, on the other hand, demonstrated higher fluctuations with a highest concentration of 0.4 wt%, which was three times that of the smallest concentration of 0.15 wt%, and consistent with the Ti rich inter-dendritic and/or grain boundaries revealed in the EPMA Ti map (Figure 5.6d).

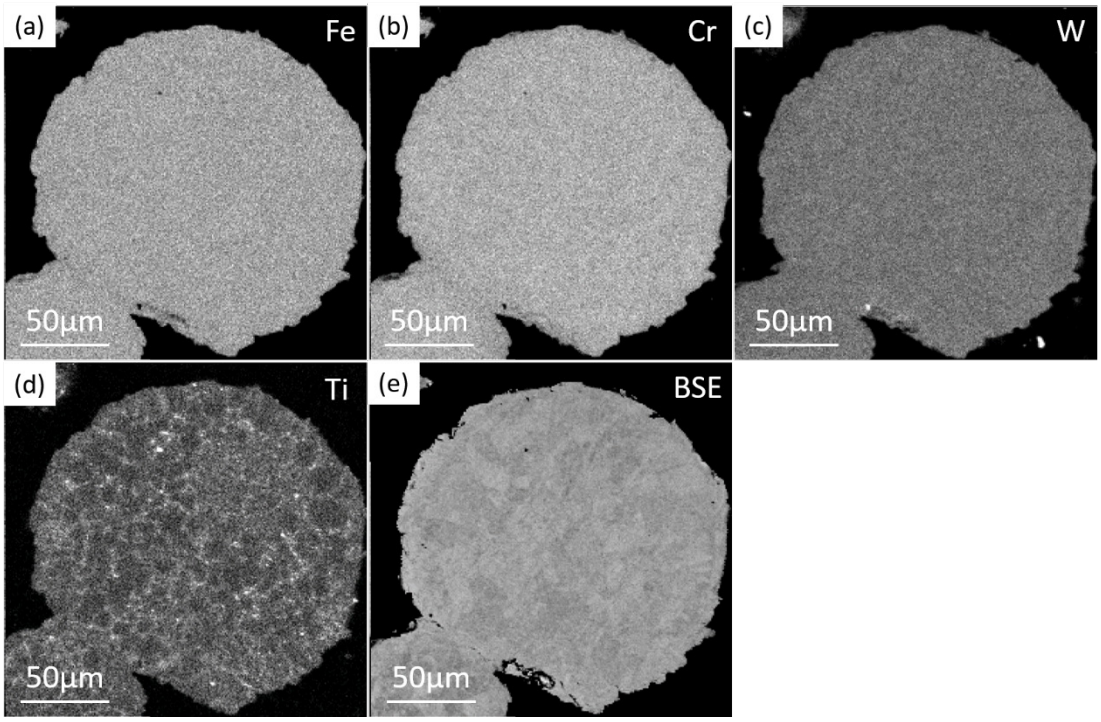

Figure 5.6: EPMA maps of 14WT pre-alloyed powder showing element distributions of (a) Fe, (b) Cr, (c) W, and (d) Ti with the corresponding BSE SEM image in (e).

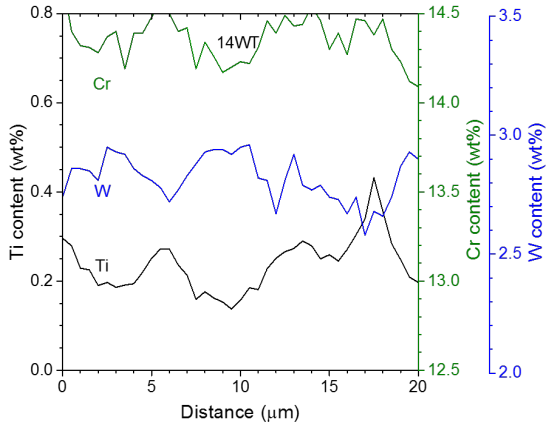

Figure 5.7: EPMA line scan of 14WT pre-alloyed powder showing variations of Ti, Cr and W concentrations over a 20 µm line-scan.

The most distinctive feature of the 2h milled 14YWTa powder particle in Figure 5.8 was a lamellar microstructure delineated by convoluted layers of contrast variations in the BSE SEM image (f) and corresponding EPMA maps (a – e). This microstructure formed through the repeated flattening, cold welding and folding of the 14WT powder, with simultaneous comminution and entrapment of the brittle Fe_3Y chips along the welds

[18,117]. The Fe_3Y chips were rapidly comminuted from mm to μm-sized layers and pockets (Figure 5.8e). The Ti concentration heterogeneity in inter-dendritic regions of the 14WT powder was improved, although some small μm-sized Ti-rich regions persisted (Figure 5.8d). The distributions of Fe, Cr and W remained generally as uniform as those measured in the 14WT powder, but the Y concentration was strongly inhomogeneous and concentrated along the interfaces of the folded lamellae. Some Y concentrations were as large as 5 μm, with a wide range of smaller sizes (Figure 5.8e). Noticeably, the region of high Fe concentration in the red circle of the Fe map (Figure 5.8a) was deficient in Cr, W and Ti (Figures 5.8b – d), and may be due to a fragment of the Fe-rich milling media described in section 3.2.3.

The 2h milled 14YWT powder particle in Figure 5.9 showed a very similar lamellar microstructure and elemental distributions. There were again concentrated Y inter-layers (Figure 5.9e), which were perhaps of slightly weaker contrast compared with those of 14YWTa in Figure 5.8e, probably suggesting a better Y distribution at this stage of milling considering the higher Y concentration in Y_2O_3 (78.6 wt%) compared with Fe_3Y (34.6 wt%). Similar Fe-rich regions were also found, highlighted by the red circle in the Fe map (Figure 5.9a), which again may be due to fragments from the Fe-rich milling media. No other element under investigation was associated with these regions.

EPMA line scans of 2h milled 14YWTa and 14YWT powders in Figures 5.10a and b respectively both show significant fluctuations in Y concentrations, with portions of the scan apparently free of Y, which was consistent with Y-enriched layers in the EPMA maps (Figures 5.8e and 5.9e). Compared with the EPMA line scan of the starting 14WT powder (Figure 5.7), Cr and W concentrations of 14YWTa and 14YWT fluctuated similarly, apart from one or two substantial drops, due to the occluded Fe_3Y/Y_2O_3 and/or milling media contamination. Ti concentrations in both 14YWTa and 14YWT exhibited less variations than those in the starting 14WT powder, consistent with

improved Ti distributions induced by milling and shown previously in the EPMA maps (Figures 5.8d and 5.9d).

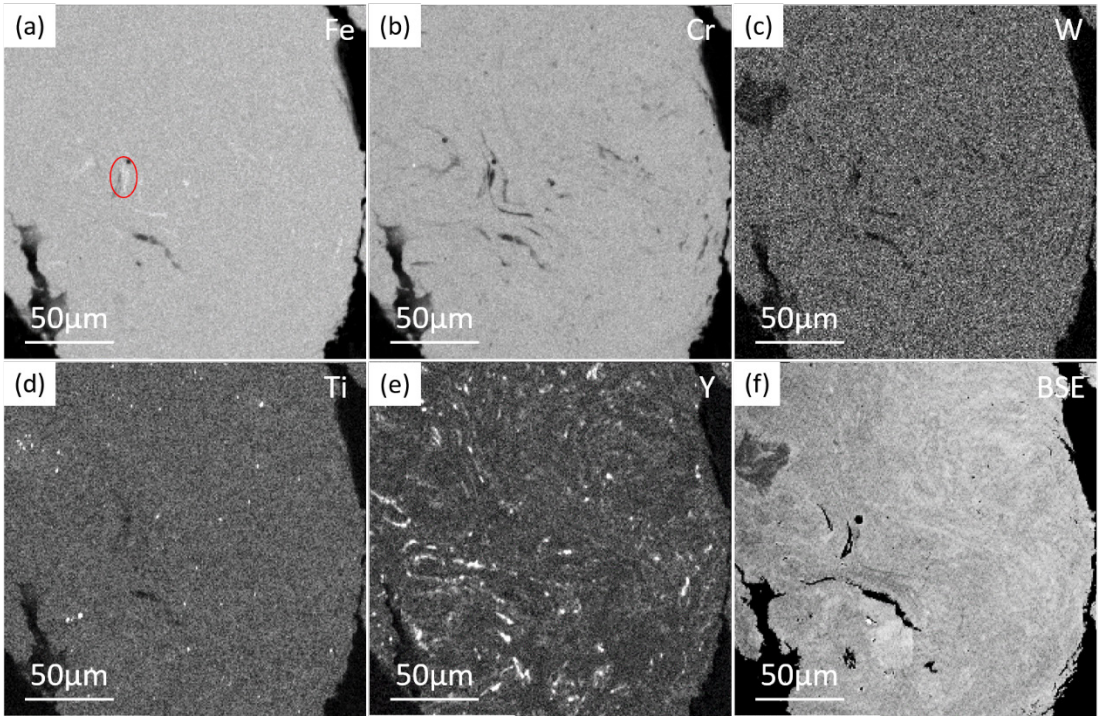

Figure 5.8: EPMA maps of 2h milled 14YWTa powder showing element distributions of (a) Fe, (b) Cr, (c) W, (d) Ti, and (e) Y with the corresponding BSE SEM image in (f).

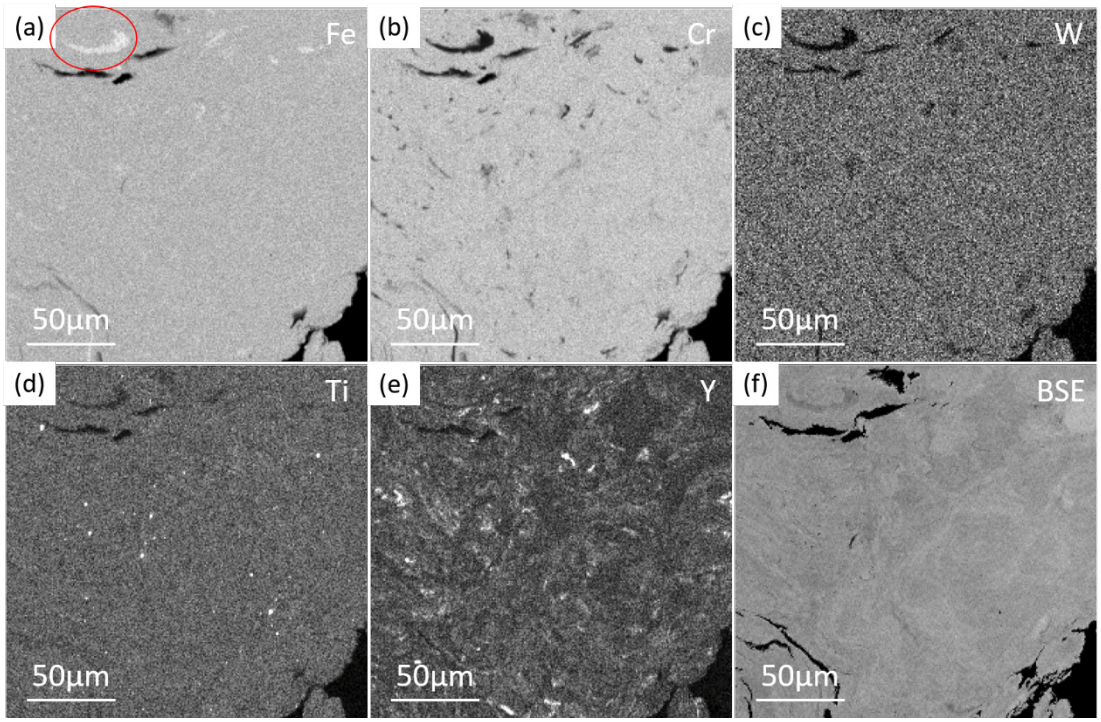

Figure 5.9: EPMA maps of 2h milled 14YWT powder showing element distributions of (a) Fe, (b) Cr, (c) W, (d) Ti, and (e) Y with the corresponding BSE SEM image in (f).

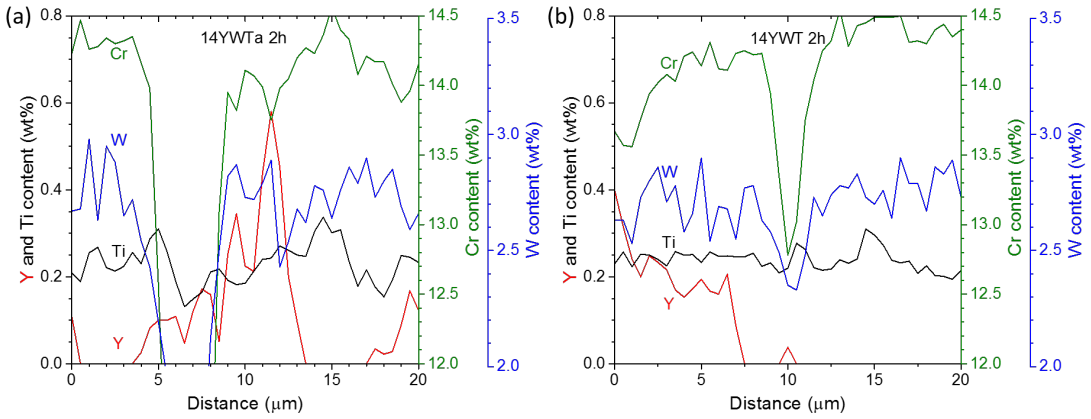

Figure 5.10: EPMA line scans of 2h milled (a) 14YWTa and (b) 14YWT powders showing variations of Y, Ti, Cr and W concentrations over a 20 μm line-scan.

When the milling time was increased to 8h, EPMA maps and BSE SEM images of the 14YWTa and 14YWT powders in Figures 5.11 and 5.12 respectively showed a significantly more refined lamellar microstructure and much weaker inter-lamellar contrast. The microstructure refinements were accompanied by increased homogenization of Y, which evolved from concentrated layers after 2h milling (Figures 5.8e and 5.9e) to weaker patches and a more uniform distribution elsewhere (Figures 5.11e 5.12e). On the contrary, the Ti distributions of both powders (Figures 5.11d and 5.12d) remained largely unchanged, suggesting relative difficulty of dispersing Ti compared with Y. The distributions of Fe, Cr and W were generally homogeneous for both powders, with again potential Fe-rich contamination labelled by red circles in Figures 5.11a and 5.12a.

The 8h milled 14YWTa and 14YWT powders displayed similar compositions in EPMA line scans (Figures 5.13a and b), with relatively steady concentrations for all investigated elements over a 20 μm line-scan. Cr and W concentrations were both averaged at 13.5 wt% and 2.6 wt% respectively, which were approximately 6% and 9% lower than those of the starting 14WT powder, probably due to further Fe-rich milling media contamination. Changes in Ti concentrations were too small to be accurately detected within the error of measurements. The Y concentrations of the 14YWTa and

14YWT powders both averaged at 0.15 wt%, with a standard deviation of 12% from place-to-place, demonstrating relatively good dispersion at this stage of milling.

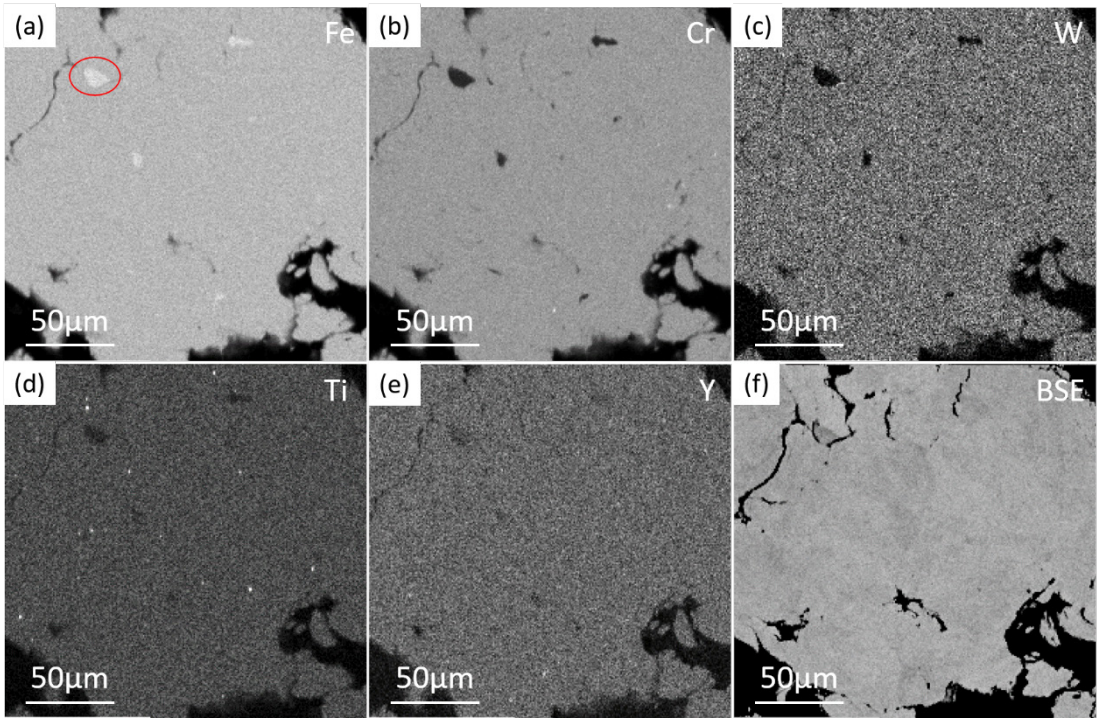

Figure 5.11: EPMA maps of 8h milled 14YWTa powder showing element distributions of (a) Fe, (b) Cr, (c) W, (d) Ti, and (e) Y with the corresponding BSE SEM image in (f).

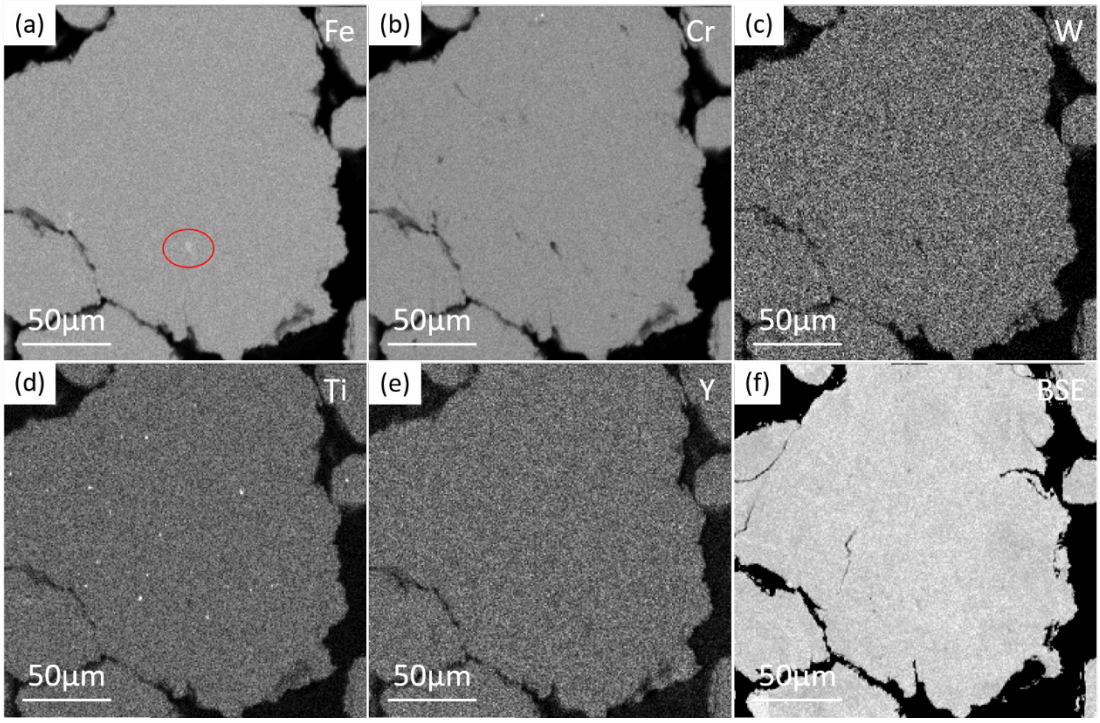

Figure 5.12: EPMA maps of 8h milled 14YWT powder showing element distributions of (a) Fe, (b) Cr, (c) W, (d) Ti, and (e) Y with the corresponding BSE SEM image in (f).

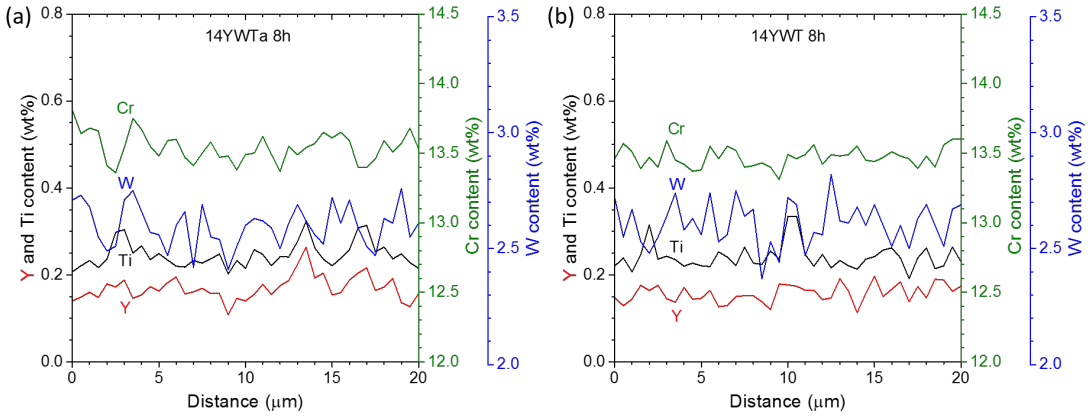

Figure 5.13: EPMA line scans of 8h milled (a) 14YWTa and (b) 14YWT powders showing variations of Y, Ti, Cr and W concentrations over a 20 μm line-scan.

After 30h of milling, EPMA maps (Figures 5.14a – e and Figures 5.15a – e) for both 14YWTa and 14YWT powders exhibited broadly homogeneous distributions of all investigated elements. Although regions of Fe-rich contamination were continued to be incorporated and resolved in the EPMA Fe map (Figure 5.14a), its weaker contrast and smaller size compared with those in the 2h and 8h milled powders suggested a levelling off of additional contamination at this stage of milling, probably due to formation of a stable powder coating on surface of the milling media that prevented further wear [18].

The EPMA line scans in Figures 5.16a and b again showed the similar compositions of the two powders. The average Cr concentrations had decreased by approximately 1% compared with the 8h milled powders. A spike in the Cr concentration for the 14YWT powder (Figure 5.16b) was co-located with faint Cr-rich spots in the EPMA map (Figure 5.15b). For both powders, the average concentrations of W, Ti and Y remained at the same levels as the 8h milled powders, while fluctuations in W concentration decreased.

On further increasing the milling time to 60h, the 14YWTa and 14YWT powders both maintained their comparatively homogeneous element distributions in the EPMA maps (Figures 5.17a – e and Figures 5.18a – e), even when higher spatial resolution of 0.2

μm was applied (compared with spatial resolution of 0.8 μm for previous scans). The line scans for both powders (Figures 5.19a and b) showed average concentrations and fluctuations were little changed from the 30h milled powders, indicating a near steady-state of element distributions were reached after 30h milling.

Overall, the BSE SEM images, EPMA maps and EPMA line scans of the 14YWTa and 14YWT powders demonstrated generally similar element distributions throughout MA process. The differences between using Fe_3Y and Y_2O_3 became undistinguishable after 8h milling despite the substantial initial size difference between the two Y sources. Both powders approached a near steady-state in element distributions after 30h milling, which corresponded well with steady-state values of other key parameters including particle size distribution, microhardness and microstructure, as discussed in previous sections 5.2.1, 5.2.2 and 5.2.3.

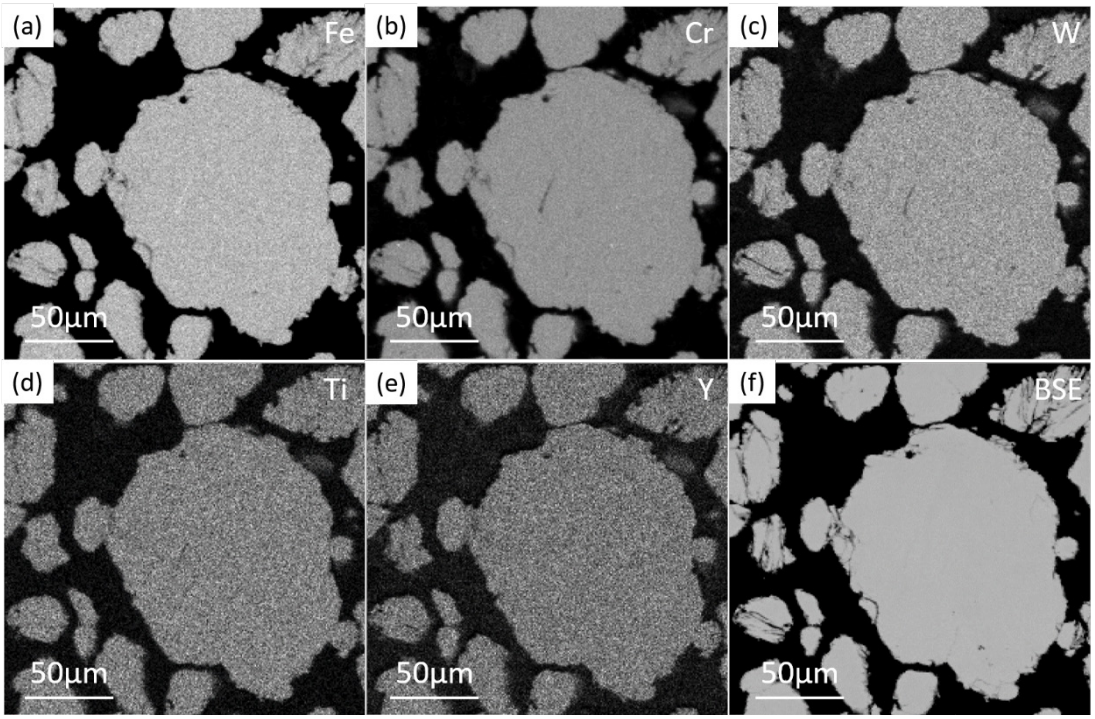

Figure 5.14: EPMA maps of 30h milled 14YWTa powder showing element distributions of (a) Fe, (b) Cr, (c) W, (d) Ti, and (e) Y with the corresponding BSE SEM image in (f).

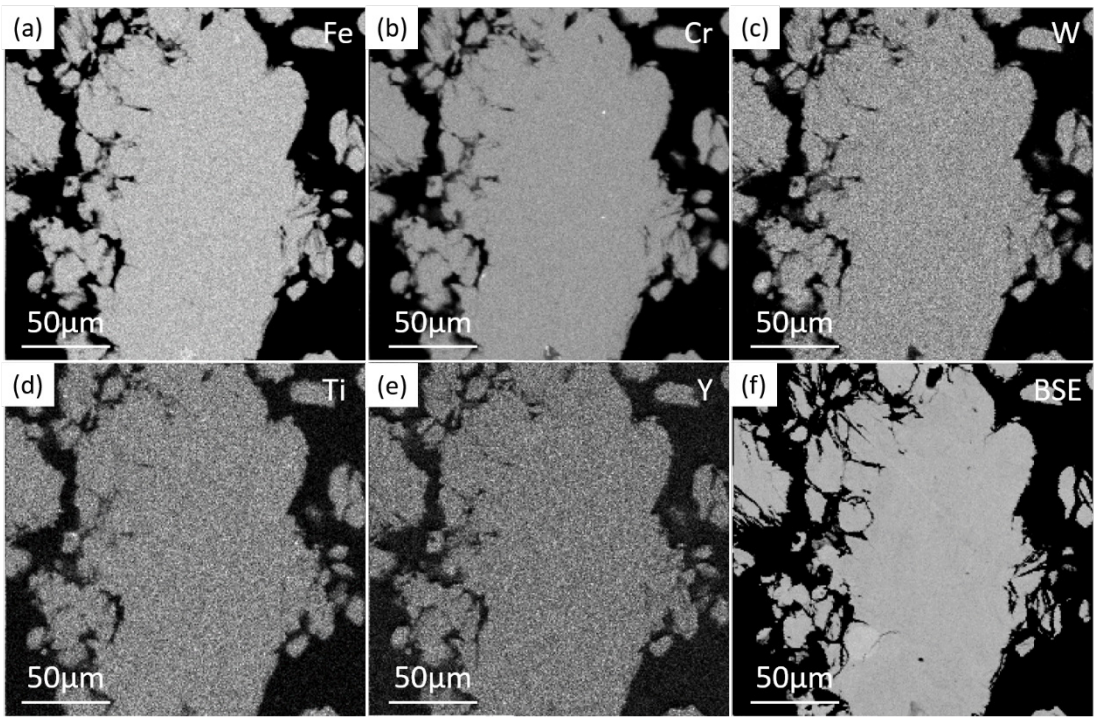

Figure 5.15: EPMA maps of 30h milled 14YWT powder showing element distributions of (a) Fe, (b) Cr, (c) W, (d) Ti, and (e) Y with the corresponding BSE SEM image in (f).

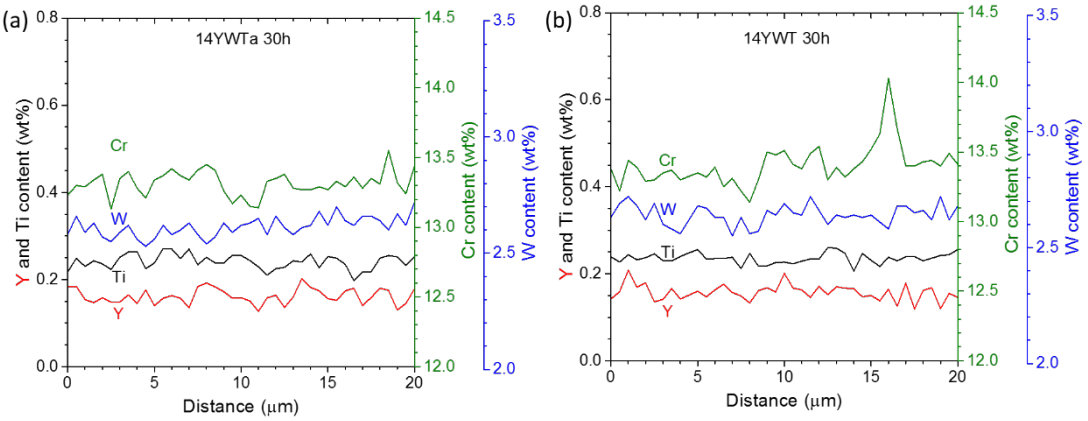

5 Figure 5.16: EPMA line scans of 30h milled (a) 14YWTa and (b) 14YWT powders showing variations of Y, Ti, Cr and W concentrations over a 20 µm line-scan.

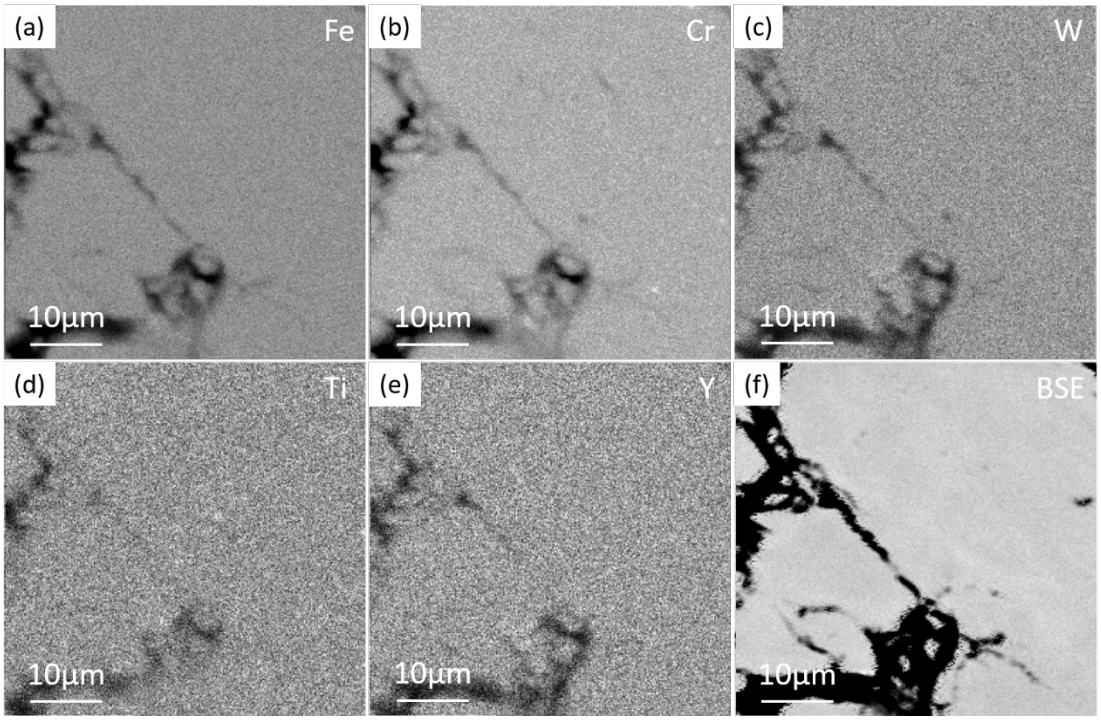

Figure 5.17: EPMA maps of 60h milled 14YWTa powder showing element distributions of (a) Fe, (b) Cr, (c) W, (d) Ti, and (e) Y with the corresponding BSE SEM image in (f).

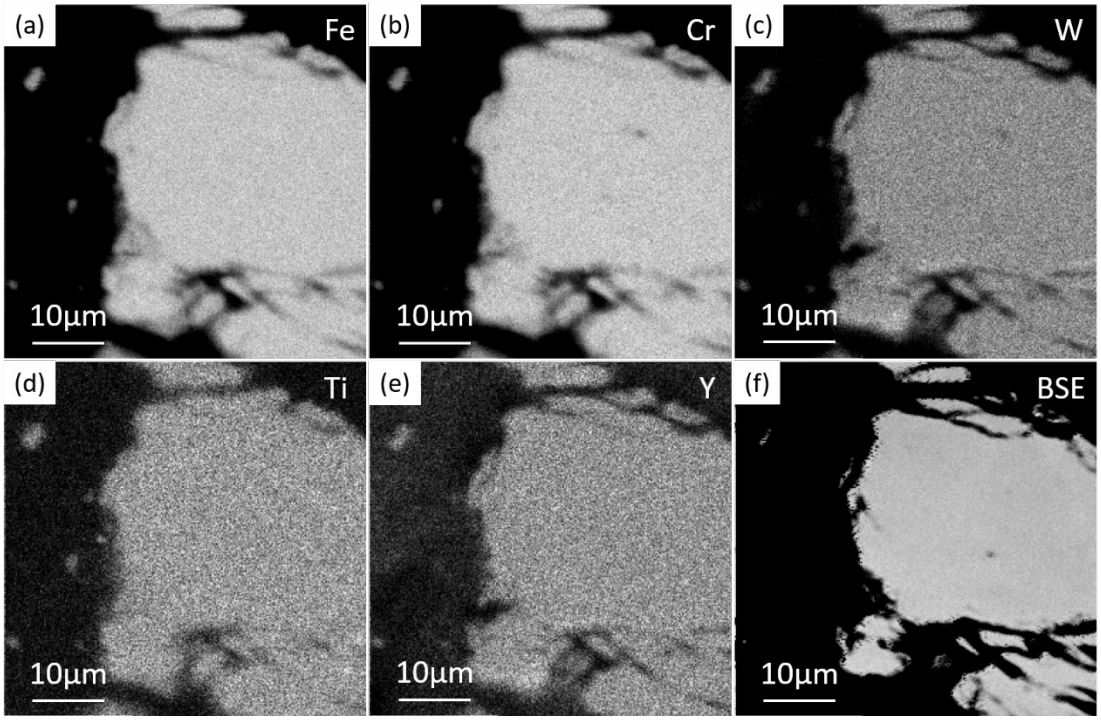

Figure 5.18: EPMA maps of 60h milled 14YWT powder showing element distributions of (a) Fe, (b) Cr, (c) W, (d) Ti, and (e) Y with the corresponding BSE SEM image in (f).

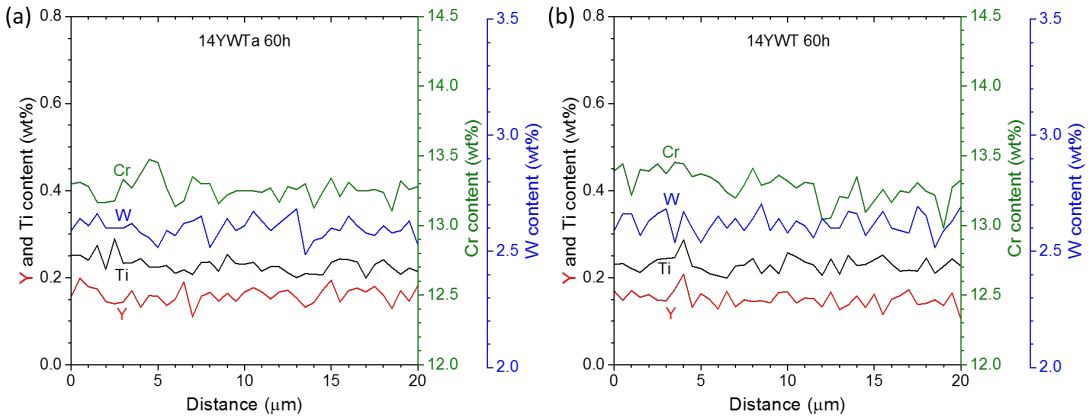

Figure 5.19: EPMA line scans of 60h milled (a) 14YWTa and (b) 14YWT powders showing variations of Y, Ti, Cr and W concentrations over a 20 μm line-scan.

The results in this section supported the potential for the use of Fe_3Y instead of Y_2O_3 as a Y source in MA, with any difference only resolved in the earliest stages. With increasing milling time, the microstructures of the two powders converged. In the steady-state condition, the two powders were virtually indistinguishable at the resolutions employed.

The following section investigates how the two as-milled powder microstructures evolved as the powders were consolidated into bulk material.

5.3 Consolidation

MA 14YWTa and 14YWT powders, together with a reference 60h milled 14WT powder, were consolidated into bulk in the same HIP run so that property variations could be directly traced back to the use of Fe_3Y or Y_2O_3 at the very beginning of the processing. Microstructures and mechanical properties of the steels were characterised using XRD, EBSD, four-point bending and Vickers microhardness tests based on procedures detailed in sections 4.1.3, 4.3, 4.5 and 4.6.

5.3.1 XRD

As shown in Figure 5.20 and as expected, the three steels comprised a bcc Fe (PDF: 00-006-0696) phase, with small peaks due to $M_{23}C_6$ (Cr15.58Fe7.42C6, PDF 01-078-1502) for 14YWTa and 14YWT. Carbide formation was probably caused by

contamination from the milling pot (2.2 wt% C in the steel) and milling balls (1.0 wt% C in the steel) during MA, due to high hardness of the two Y-containing steel powders eroding the milling media. The similar XRD traces of 14YWTa and 14YWT suggested similar phase constituents.

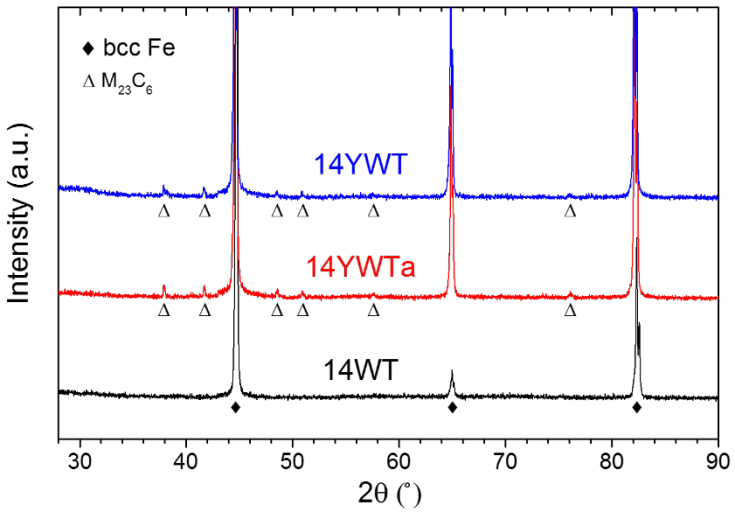

Figure 5.20: XRD measurements on 14WT, 14YWTa and 14YWT steels.

5.3.2 EBSD

EBSD scans were carried out at two spatial resolution settings in order to both ensure a sufficient analysis for a representation of the microstructure and to probe any sub-micron grains that are typically found in ODS steels [10,122–126].

EBSD coarse scans were conducted over 100 x 300 µm areas with a 500 nm step size. As shown in Figure 5.21, the reference 14WT steel had significantly larger grains than either of the Y-containing 14YWTa and 14YWT steels, indirectly suggesting some Y-containing particles acting as an effective grain size stabilizer had been formed [124,127]. Although average grain sizes of 14YWTa and 14YWT were 5.4 ± 1.7 µm and 5.7 ± 1.8 µm respectively, 14YWT had a more diverse distribution with higher fractions of both < 1 µm and > 5 µm grains (Figure 5.21d). Noticeably, the black, non-indexed, regions in EBSD maps (Figures 5.21b and c) represented areas that failed to meet the criteria of data processing, most likely due to grains being too small to fulfil requirements of

having more than three aligned pixels (misorientation < 15°) using this relatively large step size.

To further investigate the smaller grains, EBSD fine scans were conducted over 40 x 80 µm areas with an 80 nm step size. The higher spatial resolution revealed 'islands' of sub-micron grains in 14YWT (Figure 5.22b), consistent with the former non-indexed regions in the EBSD coarse scan (Figure 5.21c). In comparison, the 14YWTa (Figure 5.22a) steel had a smaller fraction of sub-micron grains, which were also distributed relatively evenly across the section. Figure 5.22c shows that 14YWT had a bi-modal grain size distribution typical for ODS steels produced by MA, while 14YWTa maintained a more uni-modal grain size distribution, similar to that seen in the EBSD coarse scan (Figure 5.21d) [10,122–126]. The smaller fraction of sub-micron grains in 14YWTa was compensated for by a reduced diameter in remaining grains, which resulted in a similar average grain size as 14YWT. The random orientations in the [001] axis inverse pole figures (IPFs) in the inset of Figures 5.21b and c and Figures 5.22a and b show both Y-containing steels had no preferred texture after HIP consolidation [108].

Although the exact reason for the bi-modal grain size distribution of ODS steels remains debateable, a relatively common argument is heterogeneous distribution of the nano-sized Y and/or Ti enriched oxides, which results in spatially varying levels of dislocation and grain boundary pinning during initial recrystallization and subsequent grain growth at elevated temperatures during consolidation [122–124]. However, it is also well-known that bi-modal grain growth always tends to occur in any alloy that relies strongly on grain boundary (Zener) pinning effects: eventually one grain breaks away and consumes all the grains around it as their higher curvature makes them comparatively soluble [128]. If it is assumed that the breadth of grain size distributions may be solely dependent on the dispersion of effective grain pinning particles, then the more converged grain size distribution of 14YWTa indicated a more uniform

distribution of these particles. Previous research has argued that a bi-modal grain size distribution could benefit mechanical properties by providing balanced ductility and strength from a combination of coarse and fine grains [129–133]. The implications of a more converged grain size distribution on the 14YWTa steel will be discussed in the following sections.

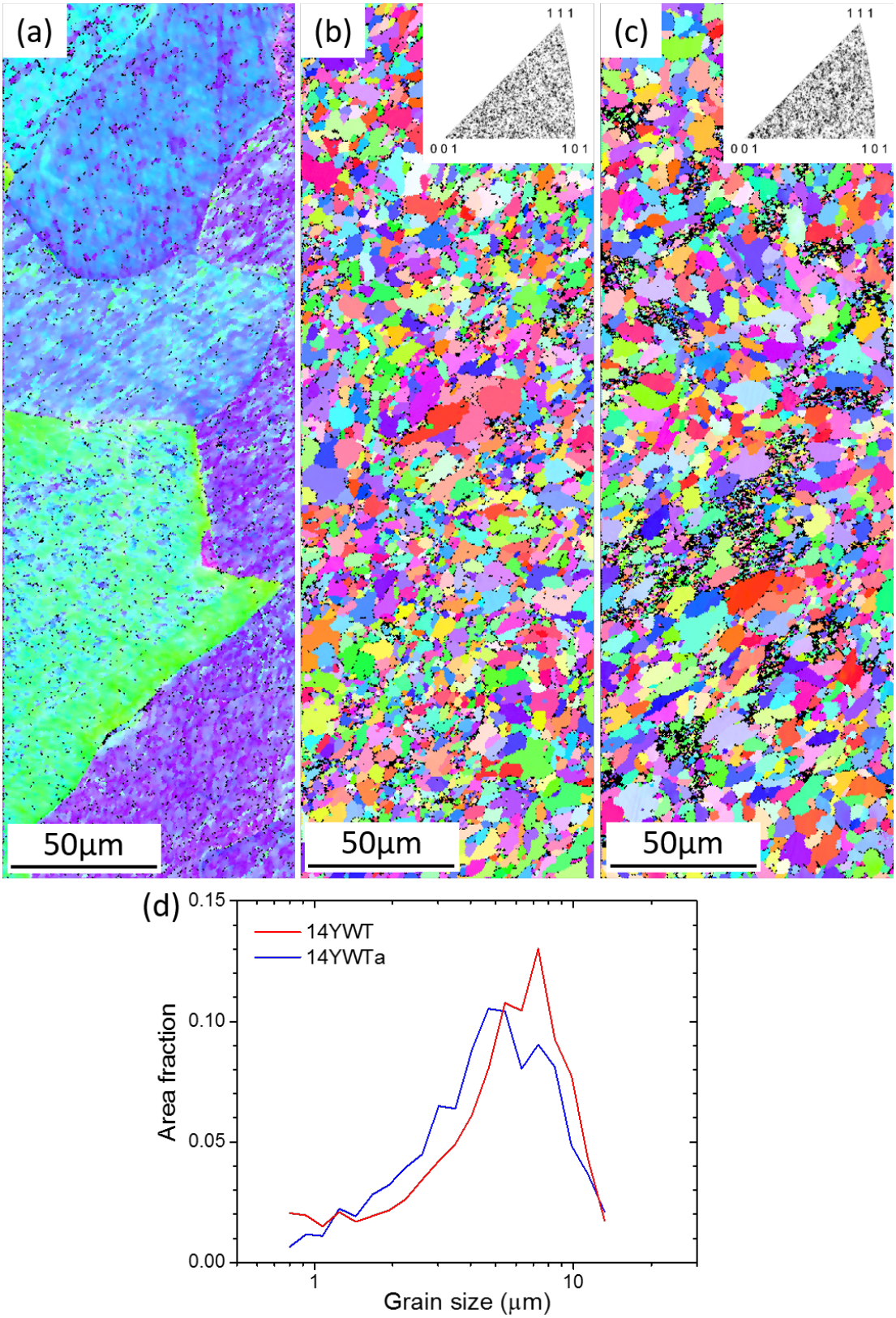

Figure 5.21: EBSD coarse scans, showing maps of (a) 14WT, (b) 14YWTa and (c) 14YWT steels with corresponding inset inverse pole figures. The grain size distributions of 14YWTa and 14YWT are summarised in (d).

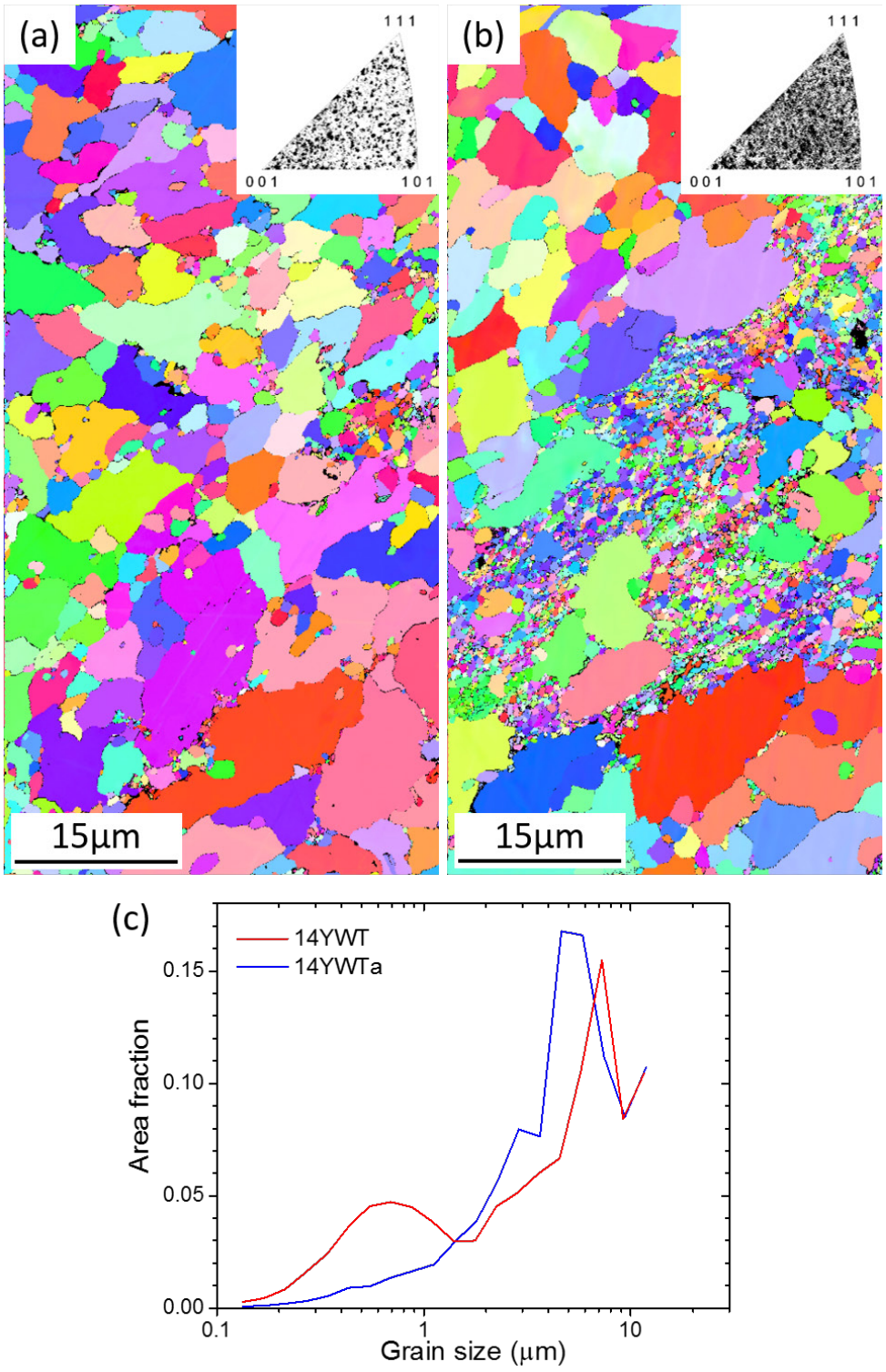

Figure 5.22: EBSD fine scans, showing maps of (a) 14YWTa and (b) 14YWT steels with corresponding inset inverse pole figures. The grain size distributions are summarised in (c).

5

5.3.3 Four-point bending

Room temperature four-point bending tests were carried out using procedures detailed in section 4.6. Three specimens each of 14YWTa and 14YWT were investigated, together with one measurement for the reference 14WT.

As shown in Figure 5.23, the stress-strain curves of 14WT had a relatively elongated plastic deformation zone. The specimen did not break by the time the displacement limit of the testing jig was reached at a strain of 0.10. In comparison, both 14YWTa and 14YWT displayed more brittle behaviour, and fractured below 5% elongation. The two Y-containing steels had a similar Young's modulus, with an average 0.2% yield strength of approximately 1000 MPa. However, 14YWTa had on average 20% more elongation before fracture compared with 14YWT, and an 8% increase in ultimate tensile strength. Comparable yield strengths and ductility results have been reported on ODS steels with similar compositions [62,134,135]. The current results are typical of the field for both alloys.

Fracture surfaces of the 14YWTa and 14YWT steels in Figure 5.24a and b were dominated by cleavage facets and river patterns typical of intergranular brittle fracture [136]. The brittle nature of the ODS steels at room temperature was in good agreement with previous studies [10,62].

A reason for the higher ductility of the 14YWTa steel may be lower fraction of sub-micron grains, as identified in section 1.3, which were suggested to possess lower dislocation storage efficiency and subsequently lower work hardening capability on deformation compared with the coarser μm-sized grains [133,137,138]. Arguably, the uni-modal grain size distribution in 14YWTa provided a better combination of strength and ductility compared with the bi-modal grain size distribution in 14YWT, but this was a relatively weak effect and overall the mechanical properties studied for the two Y-containing MAed alloys were surprisingly similar given their different starting materials.

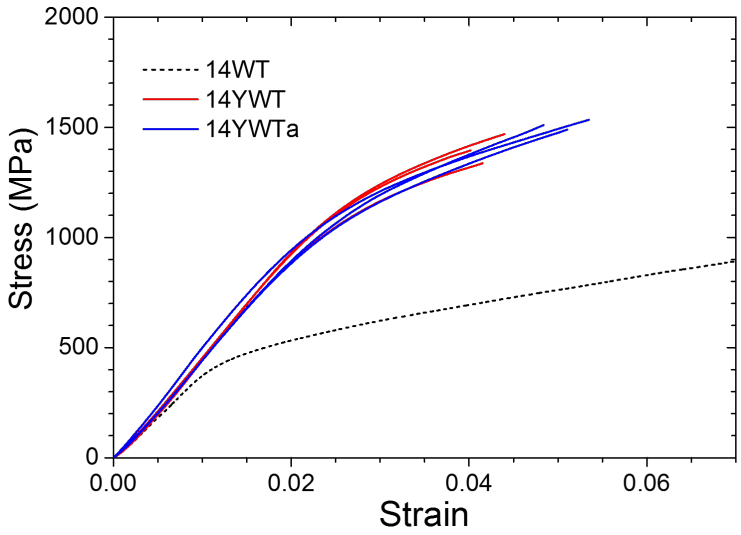

Figure 5.23: Stress-strain curves from four-point bending tests of 14YWTa (blue), 14YWT (red) and 14WT (black) steels.

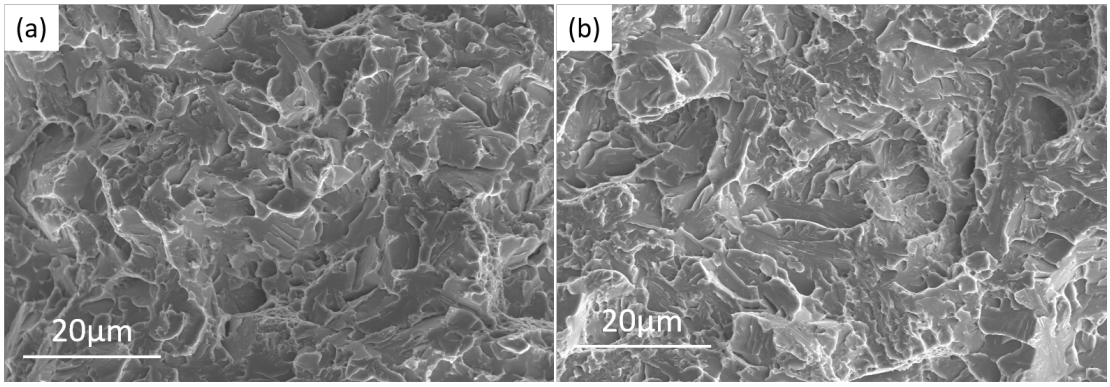

Figure 5.24: SEM images of fracture surfaces after four-point bending. (a) 14YWTa and (b) 14YWT.

5.3.4 Hot microhardness

Hot microhardness tests were carried out on 14YWTa, 14YWT and 14WT steels using procedures detailed in section 4.5.

As shown in Figure 5.25, the hardness of 14YWTa and 14YWT were typically more than four times 14WT, and were consistent with microhardness values that were reported in previous research [10,134]. 14YWT was approximately 6% harder than the 14YWTa steel at room temperature. With increasing testing temperatures, the discrepancies between the two ODS steels steadily decreased and were equal at

500 °C, at approximately 200 kg/mm^2. With further increases in temperature, the microhardness of the steels crossed, with 14YWTa approximately 20 kg/mm^2 harder than 14YWT.

The higher room temperature hardness of the 14YWT steel probably originated from a greater contribution of grain boundary strengthening due to its larger fraction of sub-micron grains compared with 14YWTa. However, since grain boundaries weaken more rapidly than grains with increasing temperature [139], 14YWT gradually lost its enhancement and became softer at temperatures above 500 °C. As summarised by Abdou [140] and Malang [141], the projected operating temperature of structural materials for first blanket wall of future fusion power plant are in the range of 470 – 700 °C depending on the exact reactor designs. Hence, 14YWTa with its higher hardness above 500 °C may be slightly better suited to those applications.

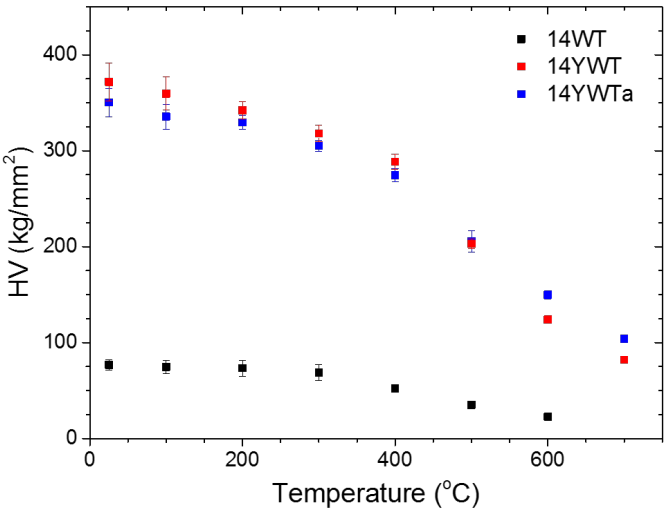

Figure 5.25: Variation in microhardness from room temperature (25°C) to 700 °C for 14YWTa (blue), 14YWT (red) and 14WT (black) steels.

5.4 Summary

14YWTa and 14YWT ODS steels were produced using identical processing parameters in MA and HIP consolidation in order to investigate microstructural and

property variations arising from the use of Fe_3Y or conventional Y_2O_3 in the starting materials. The results may be summarised as follows:

During MA:

1. 14YWTa and 14YWT powders demonstrated broadly similar evolutions of particle size distribution, microhardness, crystallite size, lattice strain and element distribution.
2. Initial major differences between 14YWTa and 14YWT powders that occurred at the early stages of milling (< 4h) quickly disappeared with increasing milling times.
3. 14YWTa and 14YWT powders approached a steady-state microstructural condition after 30h milling, with small differences in particle size, microhardness and crystallite/grain size, which then remained relatively steady up to 60h milling.

After consolidation:

1. 14YWTa and 14YWT alloys had similar XRD traces, with both showing a ferritic structure and a small amount of $M_{23}C_6$ from milling media contamination and/or interaction with consolidation materials.
2. EBSD characterisation showed 14YWTa had a narrower grain size distribution compared with 14YWT, although they had similar average grain sizes of approximately 5.5 μm.
3. Room temperature four-point bending tests showed 14YWTa had a similar yield strength to 14YWT with an approximately 20% increase in ductility.
4. Hot microhardness tests indicated a slightly higher hardness of the 14YTWa steel at temperatures > 500 °C.

Overall, the use of Fe_3Y instead of Y_2O_3 did not disrupt the standard MA approach for ODS steel powders, which was consistent with previous research [53,55]. Any enduring,

small differences may result from the likely easier refinement and dissolution of Fe_3Y than the much harder, more stable Y_2O_3.

The narrower grain size distribution of the 14YWTa steel was suggestive of a more uniform distribution of the stabilizing nano-sized Y and/or Ti enriched oxides during consolidation. A plausible reason for this relative uniformity was a better dispersion of Y originating from Fe_3Y than from Y_2O_3, although such differences might only be resolved at a spatial resolution below that of the EPMA technique used here. This then likely supported the 14YWTa steel having a higher room temperature ductility without obvious compromise on strength, as well as slightly better high temperature hardness compared with 14YWT.

Although the differences were not large, the Fe_3Y intermetallic proved to be at least as good as, or slightly better, than Y_2O_3 in terms of providing a Y source that precipitates and reacts to form Y-rich oxides during consolidation. Compared with typically nano-sized Y_2O_3 powder, the mm-sized Fe_3Y chips represent a much less demanding requirement on raw material size and morphology, which might be transferred into benefits in reduced production cost should the materials merit scaled-up manufacture.

6 Melt spun ribbon processing

6.1 Introduction

MA of a Fe based matrix and normally nano-sized (20 – 50 nm) Y_2O_3 powder is the first step in conventional ODS steel processing, which aims to promote a sufficiently uniform Y dispersion so that the precipitation of the strengthening Y enriched NPs forms with high number density during subsequent consolidation and thermo-mechanical treatments [7–12].

However, MA also presents a number of disadvantages including prolonged processing time, milling media contamination and relatively small batch process nature, which undermines its commercial viability [18,65].

Alternative fabrication routes to replace/circumvent the MA process have been investigated to achieve potentially higher throughput more suited for industrial production with reasonable compromises on microstructure and mechanical properties. A recent review article by Bergner *et. al.* summarised the latest efforts, including in-situ oxidation of a Y-containing melt during gas atomisation, oxidation of a gas atomised Y-containing powder and spray forming of a Y-containing melt [142].

As a further alternative, melt spinning is explored in this study. Melt spinning involves non-equilibrium solidification by rapid quenching of the molten metal at a cooling rate above 10^5 K/s [81]. It may therefore be capable of retaining significant amount of Y in the Fe matrix, despite its negligible equilibrium solubility. The Y may be subsequently oxidised 'internally' to form a dispersion of Y enriched oxides [63]. In principle, since materials can be produced rapidly and continuously by melt spinning, the route may provide the potential to substantially increase the production of ODS steels compared with MA. Melt spinning is a comparatively mature technology currently applied in industrial production of amorphous ferromagnetic ribbons with a global capacity exceeding 100,000 t/year [143]. Although it is unlikely that melt spinning based routes will

produce the same microstructure as MA, sufficiently useful dispersion strengthening might still be achieved and any reduction in properties offset by a big advantage in scaled-up production capability.

Reports of melt spun ODS steels could not be found in the literature. The closest related study was carried out by Nagorka *et. al.* investigating the potential of producing ODS copper alloys by internal oxidation of melt spun ribbons [60]. Nano-sized (< 100 nm) Y_2O_3 particles were successfully formed after internal oxidising Cu-0.33Y (wt%) ribbons at 750 °C for 3 h, although the particles appeared in agglomerated clusters, which was considered less than optimal to exert dispersion strengthening [60]. On the other hand, Schneibel *et. al.* demonstrated internal oxidation as a viable option to generate nano-sized Y enriched oxides from bulk Fe-Y intermetallics such as $Fe_{17}Y_2$ and $Fe_{11}TiY$ [88]. The major limiting factor in this approach was the slow diffusion rate of O, which resulted in relatively thin (< 30 μm) penetration depth from surface after internal oxidation for 3 days at 600 or 700 °C, and the Y-enriched particles were formed in mixed morphology (spherical and lamellar) and composition (Y_2O_3, $YFeO_3$, $Y_2Ti_2O_7$, Fe_2TiO_4) [88].

The following two chapters investigate the potential of ODS steel processing by (i) melt spinning of a dilute Fe-Y master alloy into Y-containing ribbons; and (ii) consolidation of ribbons into ‘bulk’ material while simultaneously internally oxidizing any retained Y in solid-solution into oxides with desirable size, morphology and distribution.

This chapter focuses on production of Y-containing melt spun ribbons, followed by internal oxidation/annealing studies. The master alloy production, melt spinning and heat treatment were carried out using procedures detailed in sections 3.3.2 to 3.3.4, with specimen designations summarised in Table 3.6.

The ribbon specimens were characterised using SEM and TEM based techniques to both examine their overall microstructure and to probe the resulting nano-sized Y enriched oxides. Detailed procedures were discussed in sections 4.1 and 4.2.

6.2 MS01 (Fe-5Y) ribbon

The MS01 ribbon was produced using the MA01 master alloy Fe-5Y (wt%) ingot to provide a relatively large contingency for the anticipated loss of reactive Y during processing.

6.2.1 Melt spun ribbons

As shown in the inset of Figure 6.1, the MS01 ribbons were 1 – 5 cm in length and 1.5 – 2.0 mm in width. The cross-section SE SEM micrograph in Figure 6.1a shows the MS01 ribbon had a typical melt spun microstructure comprising an almost featureless zone close to the cold copper wheel in which nm equiaxed grains were occasionally resolved. The cooling rate was the highest in this zone; further away heat conduction through the ribbon itself and the release of the latent heat of fusion reduced the cooling rate and columnar grains that grew along the one dimensional heat flow gradient were resolved, eventually transitioning into larger (several μm) equiaxed grains with a dendritic structure, towards the upper free surface of the ribbon [82].

The corresponding BSE SEM micrograph in Figure 6.1b displays relatively flat contrast for most of the ribbon thickness, indicating relatively uniform Y distribution, apart from some possible fine-scale inter-dendritic segregation towards the upper free surface. Area EDX measurements (red squares in Figure 6.1b) showed relatively consistent Y concentrations of 4.2 – 4.6 wt% across thickness of the ribbon. These results provided encouragement that a relatively uniform Y distribution could be achieved by melt spinning, although some Y loss was suggested.

On the other hand, O peaks were not resolved in the EDX measurements as shown in Figure 6.1c, indicating good control over O contamination during processing and

handling. However, it is worth mentioning that SEM EDX analyses had limitations on measuring O concentrations due to strong specimen absorption of the relatively low energy X-rays generated from the light element (Z < 10) and overlapping of O Kα line (0.523 keV) with Fe Lα line (0.705 keV) that could mask trace O peaks [106]. O is also a ubiquitous contaminant in vacuum systems. Hence, oxidation in the ribbons could not be eliminated. In comparison, concentrations of Fe and Y (Z > 10) were measured at higher accuracy, probably with less than ± 2% error [106].

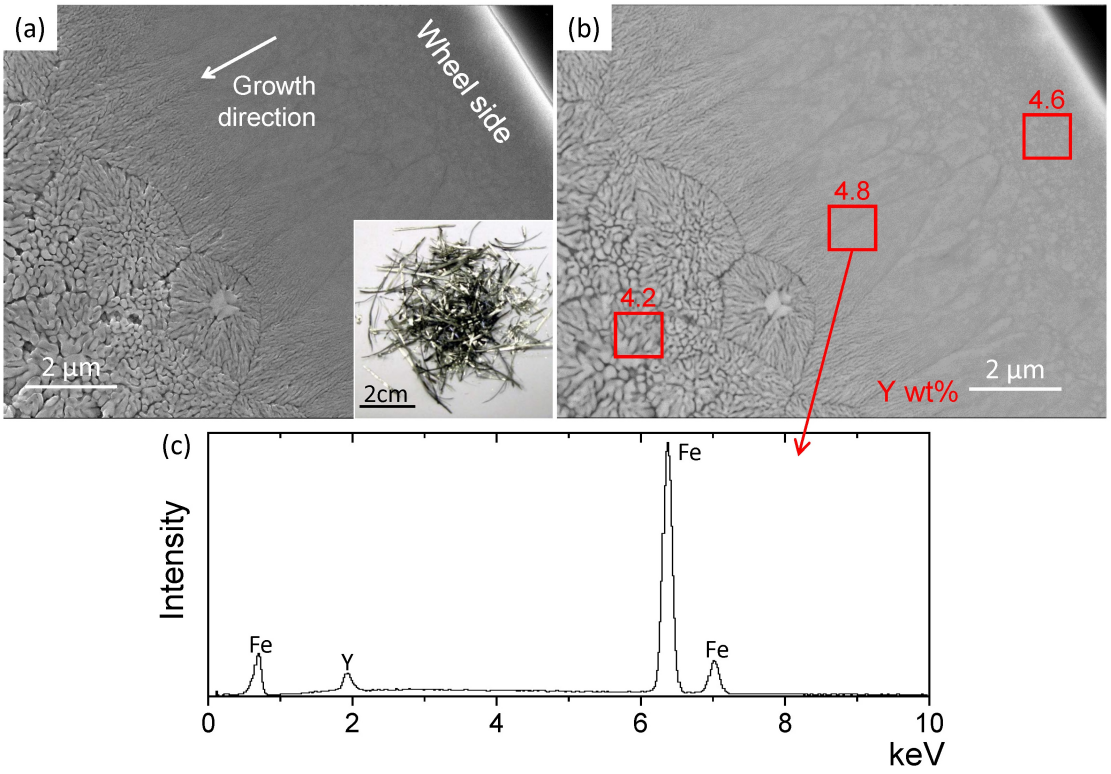

Figure 6.1: SEM characterisation of the MS01 ribbon in cross-section: (a) SE image with ribbons inset, (b) BSE image with superimposed Y concentrations (wt%) measured from EDX area analyses in the red rectangles, and (c) spectrum of one of the EDX area analyses comprising peaks corresponding to Fe and Y.

6.2.2 Internal oxidation

The as melt spun MS01 ribbons were heat treated for 4h using the Rhines pack method (section 3.3.4) at temperatures ranging from 600 to 1200 °C to investigate the potential of forming nano-sized Y oxides by internal oxidation.

Figure 6.2a shows that after 4h at 600 °C, a continuous Fe and Y-containing surface oxide layer of up to 1.5 µm thickness was formed (labelled in yellow dashed circles), indicating Y diffusion towards ribbon surface where the O partial pressure was the highest during heat treatment. The original three zone cross-section microstructure of the as-produced ribbons was largely retained with slight coarsening of the grains. EDX measurements in representative regions show Y concentrations (red, 4.6 – 4.8 wt%) were similar to the as-produced ribbons, with some introduction of O (blue, 0.5 – 0.7 wt%), noting likely inaccuracy of O quantification.

Increasing the oxidation temperature to 700 °C (Figure 6.2b) promoted homogenization of the three zone microstructure and produced darker contrast 'trails' probably due to preferential etching and pull-out of small particles along some of the grain boundaries during sample preparation. EDX measurements from typical regions of the ribbon cross-section detected Y (red, 4.6 – 4.9 wt%) and O (blue, 1.2 – 1.3 wt%), indicating faster O diffusion into the ribbon and possible formation of Y-containing oxides that could not be resolved. The Fe and Y-containing surface oxide layers were of similar thickness as the 600 °C heat treated ribbons.

There was more obvious particle formation at 800 °C in Figure 6.2c. The majority of particles in the centre of the ribbon had a spherical shape with diameters < 100 nm, while larger, rod-shaped particles were present with increasing frequency towards both edges. Nevertheless, EDX area analyses showed Y and O concentrations remained at 4.7 – 4.8 wt% and 1.3 – 1.4 wt% respectively, and similar in the centre and at the edge of the ribbon. In addition, the Fe and Y-containing surface oxide layer maintained similar thickness compared with the ribbons heat treated at 600 °C and 700 °C.

Further increases in temperatures led to significant particle coarsening up to diameters of 1 – 2 µm at 900 °C (Figure 6.2d) and up to 10 µm at 1000 °C (Figure 6.2e). EDX measurements showed the particles were enriched in Y and O, with accompanying depletion of both elements in the ribbon 'matrix', which indicated increasing Y diffusion

rate at higher heat treatment temperatures. Noticeably, some of the Y enriched oxides at the edge of the ribbons started to combine with the surface oxide layer, as highlighted by yellow dashed circles in Figures 6.2d and e.

At 1200 °C, Y diffusion became so rapid that most Y was able to migrate to the ribbon surface, react with O and form the surface oxide layer. Furthermore, the coarsened grains resulting from the relatively high heat treatment temperature reduced the number of grain boundaries that acted as fast track for O diffusion. The overall effect was an Fe 'matrix' largely free of Y and O, as shown in the EDX measurement of a typical region in Figure 6.2f. It is worth noting that most of the brittle surface oxide layer was broken up and lost during sample preparation, leaving only a small portion visible in Figure 6.2f.

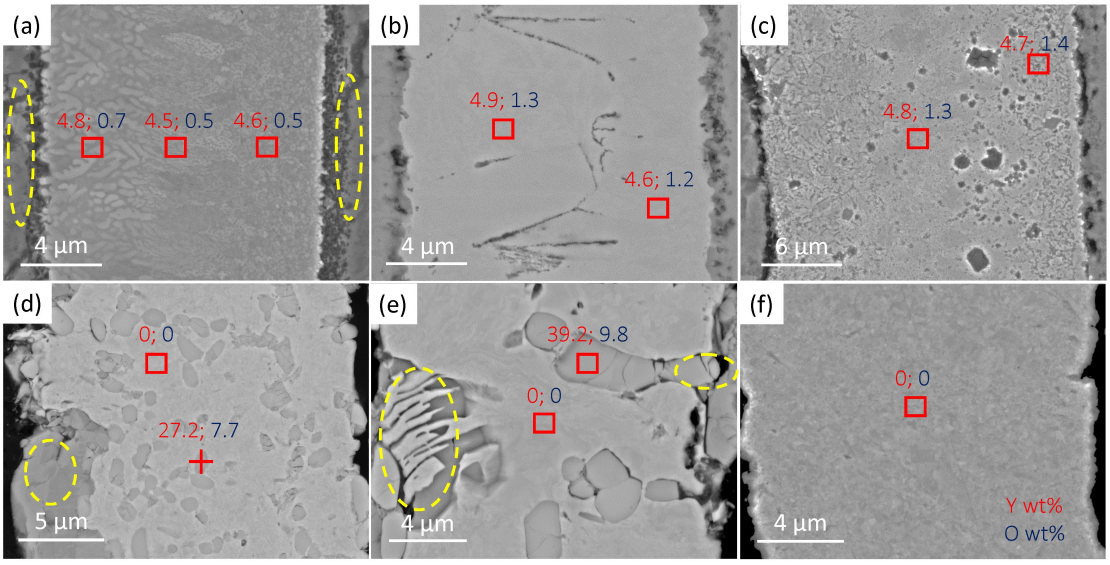

Figure 6.2: BSE SEM micrographs showing MS01 ribbon heat treated at (a) 600 °C, (b) 700 °C, (c) 800 °C, (d) 900 °C, (e) 1000 °C and (f) 1200 °C for 4h. Y (red) and O (blue) concentrations were approximated from EDX area and point analyses, and are labelled with rectangles and crosses respectively. Surface oxide layer in (a) and surface oxides in (d) and (e) were highlighted in yellow dashed circles.

TEM investigations were then carried out to study further the relatively small (< 100 nm) spherical particles in the 800 °C and 700 °C oxidised ribbons.

6.2.2.1 Ribbon heat treated at 800 °C

The low magnification STEM HAADF micrograph in Figure 6.3a shows the 800 °C internal oxidised ribbon had sub-micron grains ranging from 200 to 800 nm; a representative grain is highlighted by a superimposed yellow dashed line. Larger rod shaped (> 100 nm in length) and equiaxed (> 100 nm) particles with darker contrast were formed along grain boundaries, while there were smaller (< 20 nm) spherical particles within the grains. A higher magnification STEM HAADF micrograph in Figure 6.3b suggested that the smaller intragranular particles had a higher number density than those generated through internal oxidation of bulk Fe-Y intermetallics [88], with enrichment of Y and O according to the inset EDX elemental maps.

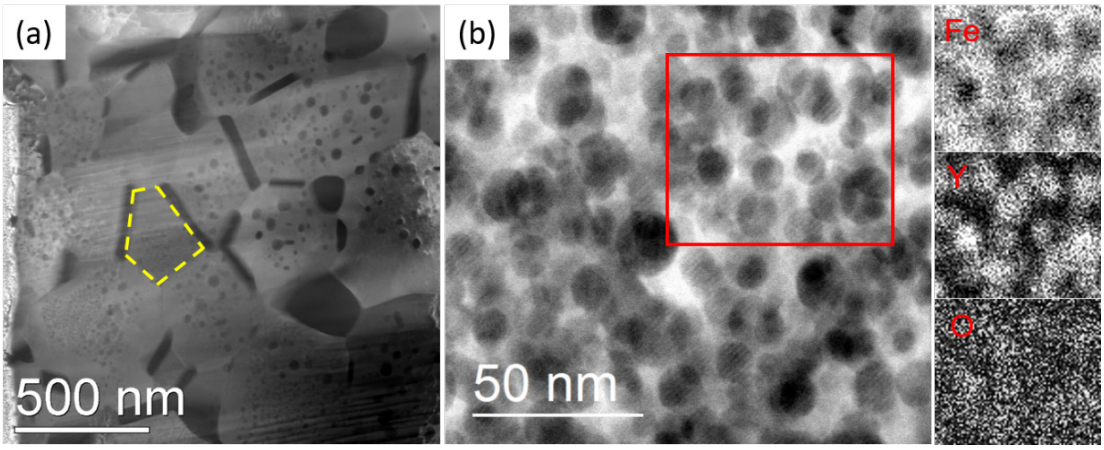

Figure 6.3: STEM microstructural analyses of MS01 ribbon heat treated at 800 °C: (a) low magnification HAADF micrograph with yellow dashed lines highlighting a grain, and (b) higher magnification HAADF micrograph with inset EDX elemental maps of Fe, Y and O.

As shown in the bright field TEM image in Figure 6.4a, SAD of the ribbon heat treated at 800 °C was performed over an area (red circle) covering both grain boundary and intragranular particles. The resulting SAD pattern in Figure 6.4b was in good agreement with simulated diffraction rings of bcc Fe (blue lines, PDF: 00-006-0696) and cubic Y_2O_3 (red lines, PDF: 01-071-0049). The HRTEM image (Figure 6.4c) and its FFT analysis (Figure 6.4d) of an approximately 20 nm diameter intragranular

particle further confirmed a cubic Y_2O_3 structure, in this case oriented along the [1 0 1] zone axis. A cubic structure of the precipitated Y oxide may have suggested the possibility for semi-coherency with the ferrite matrix, but this was not studied in detail.

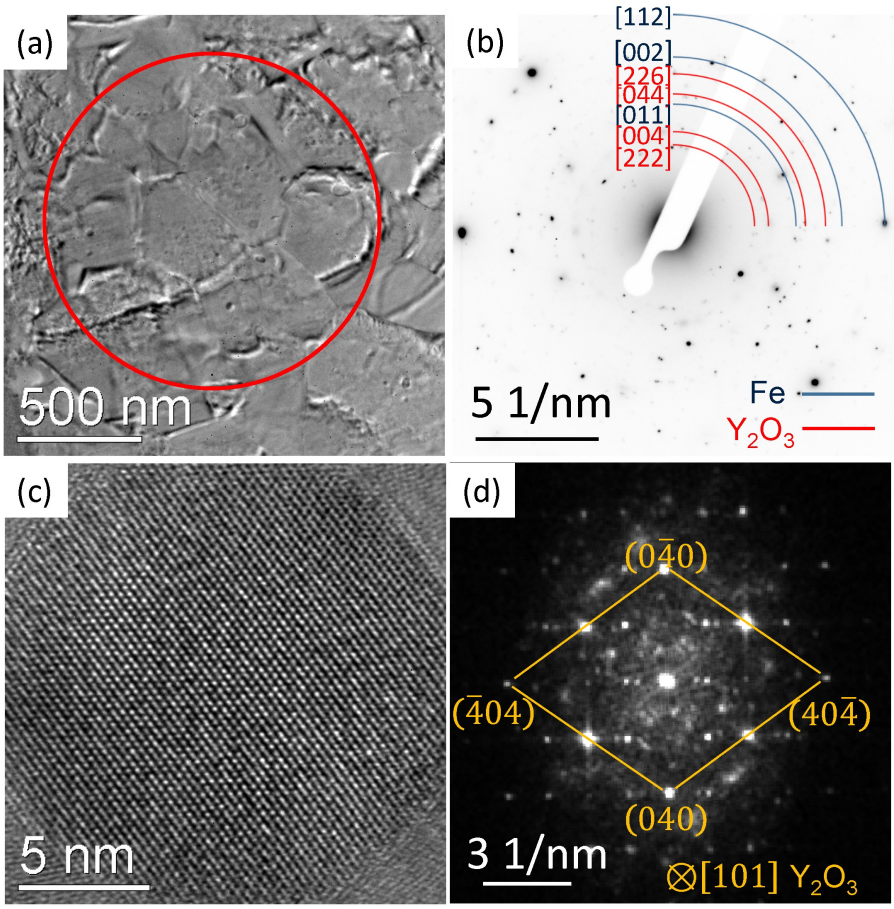

Figure 6.4: TEM microstructural analyses of MS01 ribbon heat treated at 800 °C: (a) BF TEM micrograph, (b) SAD pattern of the red circled area in (a), (c) HRTEM image of a small in-grain particle, and its corresponding (d) FFT image and crystallographic analysis.

6.2.2.2 Ribbon heat treated at 700 °C

The STEM HAADF image in Figure 6.5a of the ribbon heat treated at 700°C shows a high number density and relatively uniform distribution of < 20 nm particles that were not previously resolved by SEM imaging. A typical grain is highlighted with a superimposed yellow dashed line. The grains were < 200 nm and smaller than most of those in the ribbon heat treated at 800 °C. There was no significant size variation

between the grain boundary and intragranular particles, and the particle size histogram in Figure 6.5b based on 650 manual measurements exhibited a unimodal size distribution, with more than three quarters of the particles diameters in between 5 and 15 nm. The higher magnification STEM HAADF micrograph in Figure 6.5c further confirmed a comparatively high number density of particles, which were again enriched in Y and O.

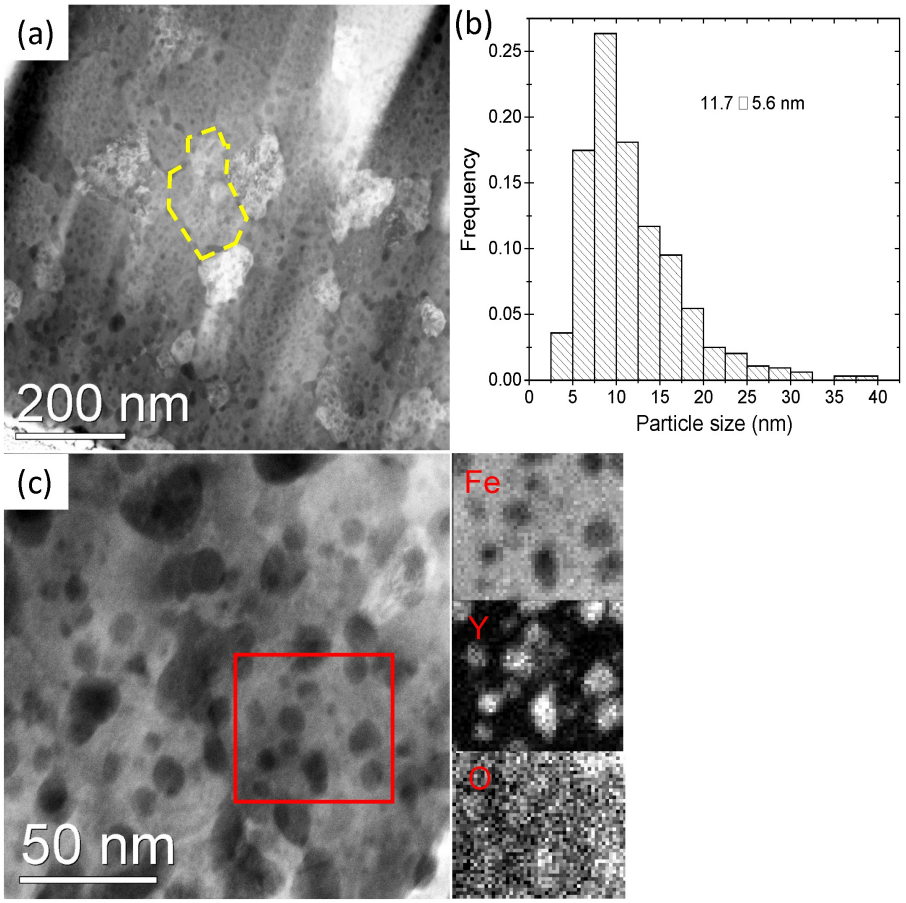

Figure 6.5: STEM microstructure analyses of MS01 ribbon heat treated at 700 °C: (a) Low magnification HAADF micrograph with yellow dashed lines highlighting a grain, (b) particle size histogram, and (c) high magnification HAADF micrograph with inset EDX elemental maps of Fe, Y and O.

To further investigate the Y and O enriched particles, SAD was performed over the area shown in Figure 6.6a (red circle) covering a large number of grains. The corresponding SAD pattern (Figure 6.6b) matched well with simulated diffraction rings

of bcc Fe (blue lines, PDF: 00-006-0696) and cubic Y_2O_3 (red lines, PDF: 01-071-0049). HRTEM image (Figure 6.6c) and its FFT analysis of a < 10 nm particle confirmed its cubic Y_2O_3 structure oriented along the [1 0 1] zone axis.

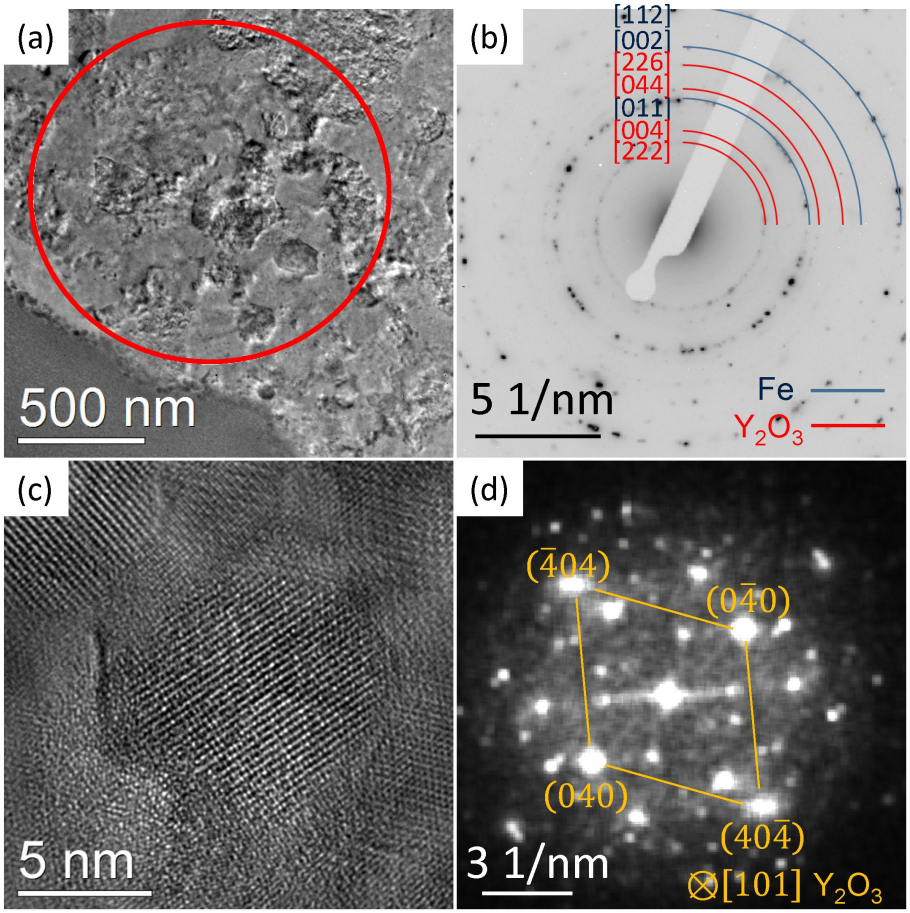

Figure 6.6: TEM microstructure analyses of MS01 ribbon heat treated at 700 °C: (a) BF TEM micrograph, (b) SAD pattern of the red circled area in (a), (c) HRTEM image of a small in-grain particle, and its corresponding (d) FFT image and crystallographic analysis.

In summary, the melt spinning followed by heat treatment to promote internal oxidation of the retained Y in the MS01 ribbon demonstrated encouragement for the formation of a high number density of < 20 nm Y_2O_3 particles. The internal oxidation temperature played a critical role in controlling the size and distribution of the O-rich particles, and the optimal temperature which promoted a large number of smaller O-rich particles was identified as approximately 700 °C. Excessive particle coarsening at temperatures

above 900 °C suggested consolidation techniques that require prolonged exposure at elevated temperatures may not be suitable for the melt spun ribbons, which unlike MA powders do not offer a very high dislocation density to promote fine scale, uniform nucleation.

6.3 MS02 (Fe-1Y-1Ti) ribbon

Based on the promising results, production of MS02 ribbon was carried out using the MA02 master alloy (Fe-1Y-1Ti, wt%) with a Y concentration closer to typical ODS steels, and with the addition of Ti that is known to produce a refining effect of Y enriched particles in MA [44,47,53].

6.3.1 Master alloy

SEM EDX measurements on the MA02 master alloy were used to examine the distribution of Y and Ti after the arc melting of the cold-pressed powder billets. Typical SE SEM images and the corresponding EDX elemental maps in Figure 6.7 show pronounced Y concentrations in 1 – 2 μm ‘spots’, without apparent coexistence of O, and a relatively uniform Ti distribution. Noticeably, the overall Y concentration from the EDX map was 0.1 ± 0.02 wt%, indicating an approximately 90% Y loss during master alloy production. Such a substantial loss of Y was primarily attributed to the use of pure Y powder, which was prone to react with oxygen even during transfer and handling of the cold pressed powder billets. Compared with the MA01 master alloy, a similar amount of absolute Y loss (up to 0.9 wt%) accounted for a much higher proportion in the MA02 master alloy because it had an 80% lower Y concentration. More positively, the added Ti was successfully retained with an overall concentration close to nominal of 1.1 ± 0.01 wt%.

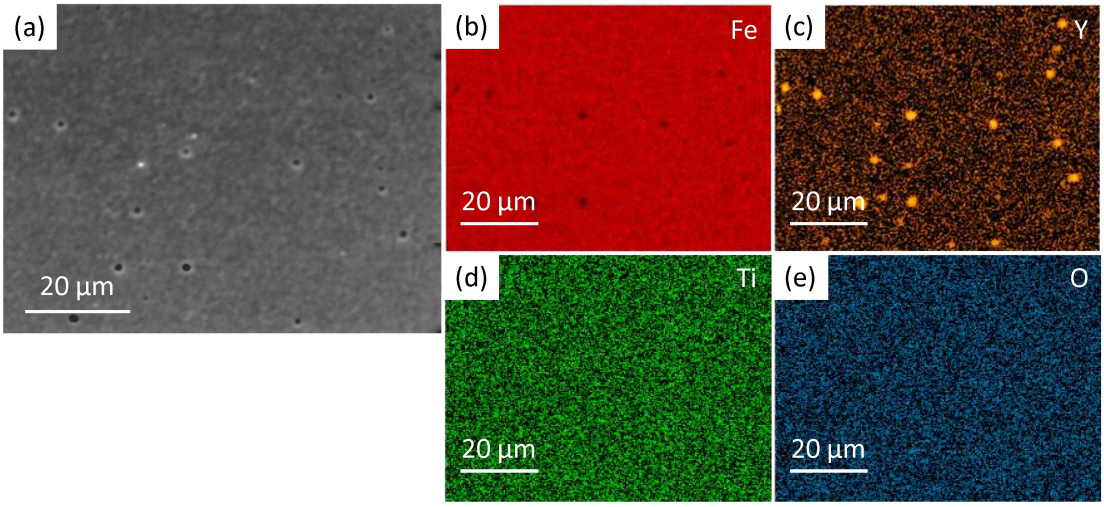

Figure 6.7: SEM characterisation of the MA02 master alloy: (a) SE SEM micrograph with corresponding EDX elemental maps of (b) Fe, (c) Y, (d) Ti, and (e) O.

6.3.2 Melt spun ribbon

The corresponding SE and BSE SEM micrographs in Figure 6.8a and b show the MS02 ribbon cross-section had a relatively featureless microstructure at this resolution, without apparent variations across the ribbon thickness. This was very different from the three zone microstructure of the MS01 ribbon and may reflect the lower Y concentration that made generation of contrast more difficult. Another effect may be a higher cooling rate generated because of switching to a different melt spinner in STJU, Shanghai, China.

EPMA line scans (labelled in red lines in Figure 6.8b) across the thickness of the ribbon confirmed the significant Y loss (Figure 6.8c) with Y showing some inter-dendritic segregation but a mean concentration of 0.07 ± 0.04 wt% Y, consistent with the MA02 master alloy. In comparison, the Ti (Figure 6.8d) was largely retained after melt spinning at an average concentration of 1.05 ± 0.03 wt% taken from the three through thickness EPMA line scans.

Although in this case master alloy formulation was problematical, there was no significant additional Y or Ti loss during melt spinning.

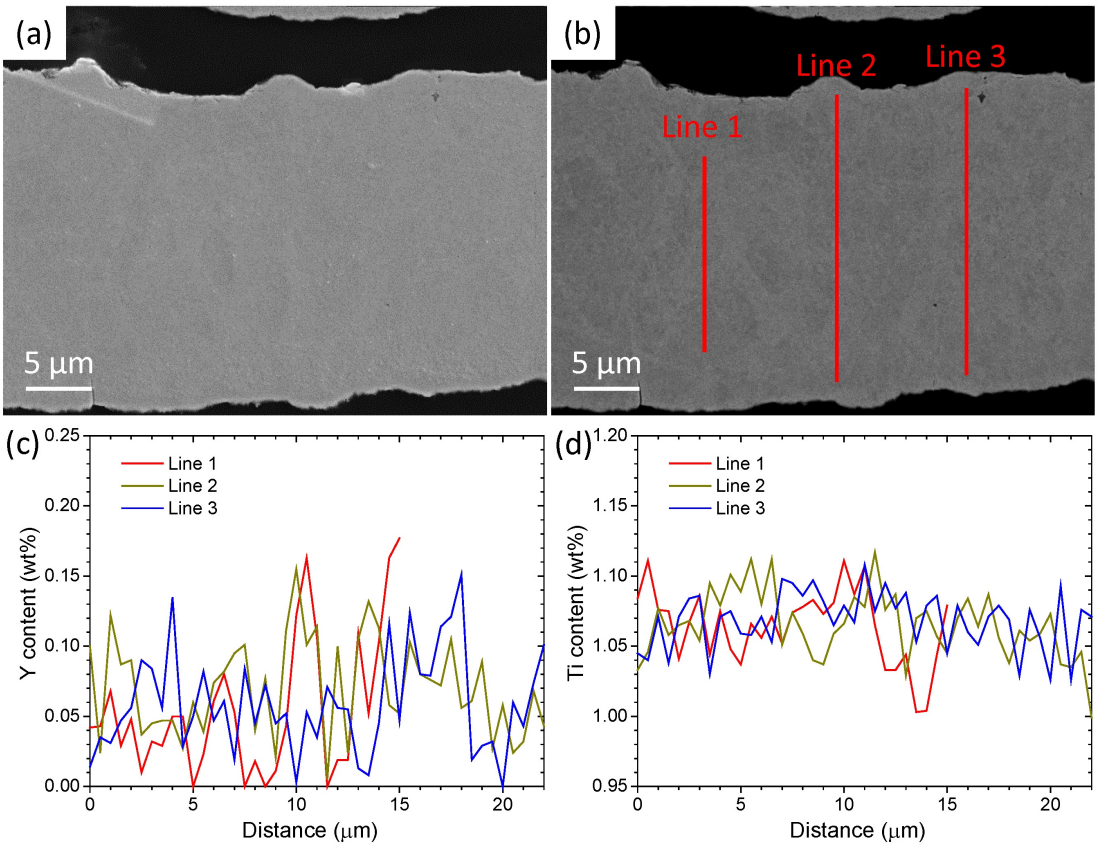

Figure 6.8: SEM characterisation of the MS02 ribbon in cross-section: (a) SE micrograph, and (b) BSE micrograph with red lines labelling EPMA line scans across the ribbon thickness, of which the Y and Ti concentrations against scanning distance are plotted in (c) and (d).

6.3.3 Vacuum annealing

With much reduced Y concentration, the MS02 ribbon was not considered worthwhile for further investigation of its oxidation response, but instead it was vacuum annealed at 1000 °C for 4h to analyse the behaviour of the Ti at this typical conventional consolidation temperature.

As shown in Figure 6.9a, < 100 nm spherical particles were formed after vacuum annealing. The corresponding EDX elemental maps in Figure 6.9b – e show the particles were enriched in Ti, with weaker Y concentrations also appearing in several cases. Compared with a Ti-rich particle in Figure 6.10b, the EDX line scan of a particle enriched in both Y and Ti (Figure 6.10c) revealed a Y-rich core surrounded by a Ti-rich shell, suggesting Ti enriched particles may have acted as preferential nucleation sites

for Y-rich particles at elevated temperatures. Since the Ti-enriched particles were capable of maintaining relatively small sizes and encouraging uniform distribution after 4h vacuum annealing at 1000 °C, the preferential association of Y onto these particles could result in refined Y and Ti enriched, complex stoichiometry particles and potentially avoid the excessive coarsening observed in the MS01 ribbon.

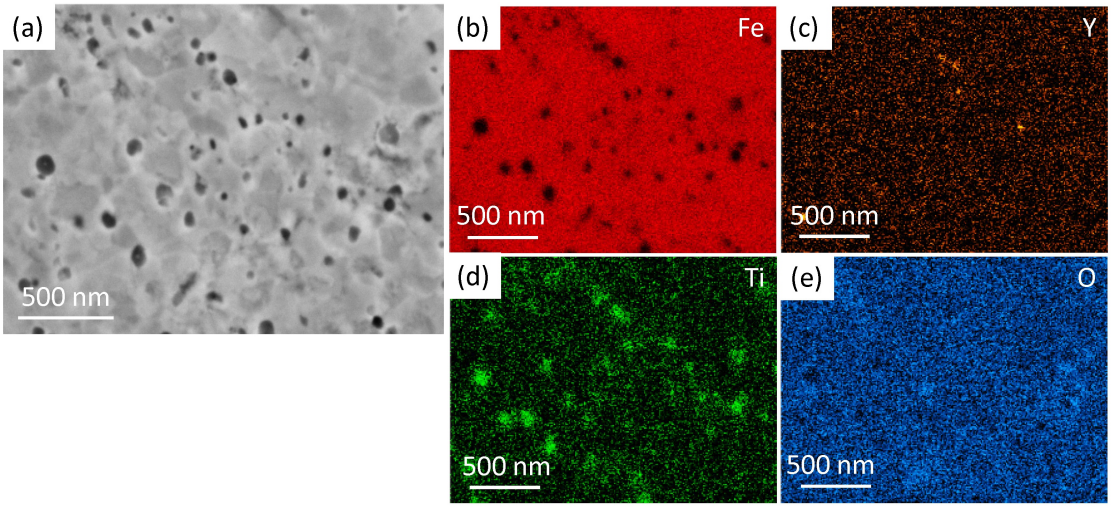

Figure 6.9: SEM characterisation of the MS02 ribbon after annealing at 1000 °C for 4h: (a) BSE SEM micrograph with corresponding EDX elemental maps for (b) Fe, (c) Y, (d) Ti, and (e) O.

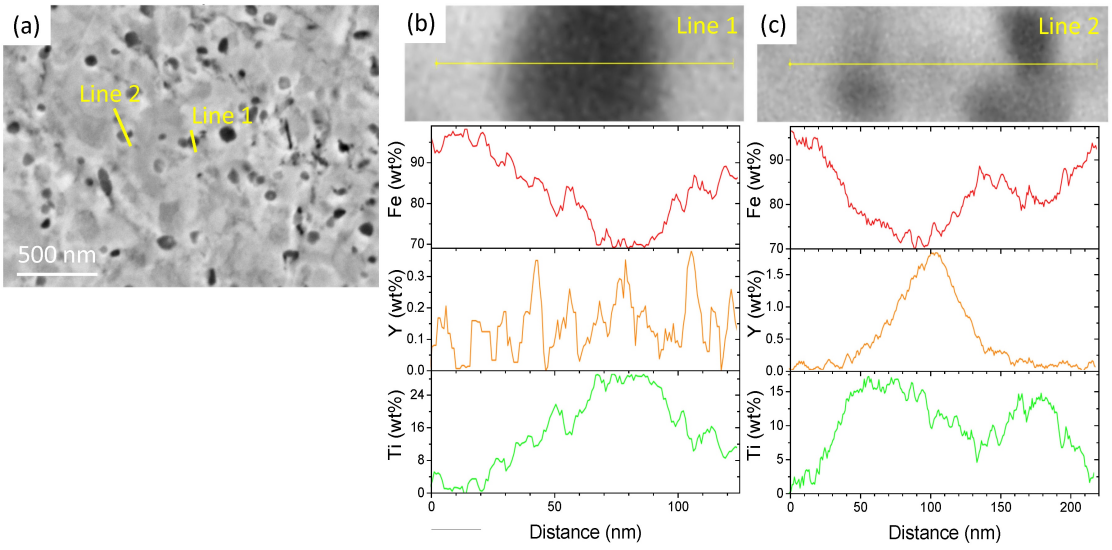

Figure 6.10: SEM characterisation of the MS02 ribbon after annealing at 1000 °C for 4h: (a) BSE SEM micrograph with yellow lines labelling EDX line scans on two typical particles, for which the Fe, Y and Ti concentrations against scan distance are plotted in (b) and (c).

The Ti enriched particles were characterised using TEM-based techniques to further understand their chemical composition and crystal structure. The BF TEM (Figure 6.11a) and STEM HAADF (Figure 6.11b) micrographs show a relatively high number density of particles. EDX elemental maps of a typical particle in Figure 6.11b confirmed enrichment with Ti, without apparent concentration of Y or O. The corresponding HRTEM image of the particle and its FFT analysis suggested the particle as Fe_2Ti (PDF: 01-075-7815) oriented along the [111] zone axis, which is one of the common types of precipitates in 18Ni maraging steels (18 wt% Ni, 3 – 5 wt% Mo, 8.5 – 12.5 wt% Co, 0.2 – 1.6 wt% Ti and 0.1 wt% Al) [144,145].

Overall, the MS02 ribbon had a relatively uniform distribution of Ti in the Fe matrix. On the other hand, Y loss was problematical and perhaps a less reactive form of Y, such as Fe-Y intermetallics, could be applied for these compositions with lower Y concentration. High temperature vacuum annealing of the MS02 ribbon formed nano-sized Fe_2Ti particles, which were suggested to act as preferential sites for Y accumulation, in conjunction with O, and may contribute to refining of Y-rich oxide particles. It may be speculated that in the decomposition of the Y-containing Fe-rich solid solution at elevated temperature, the prior formation of Fe_2Ti provides a comparatively efficient nucleation site for Y-O containing particles. With time, a Y-Ti-O containing oxide then forms.

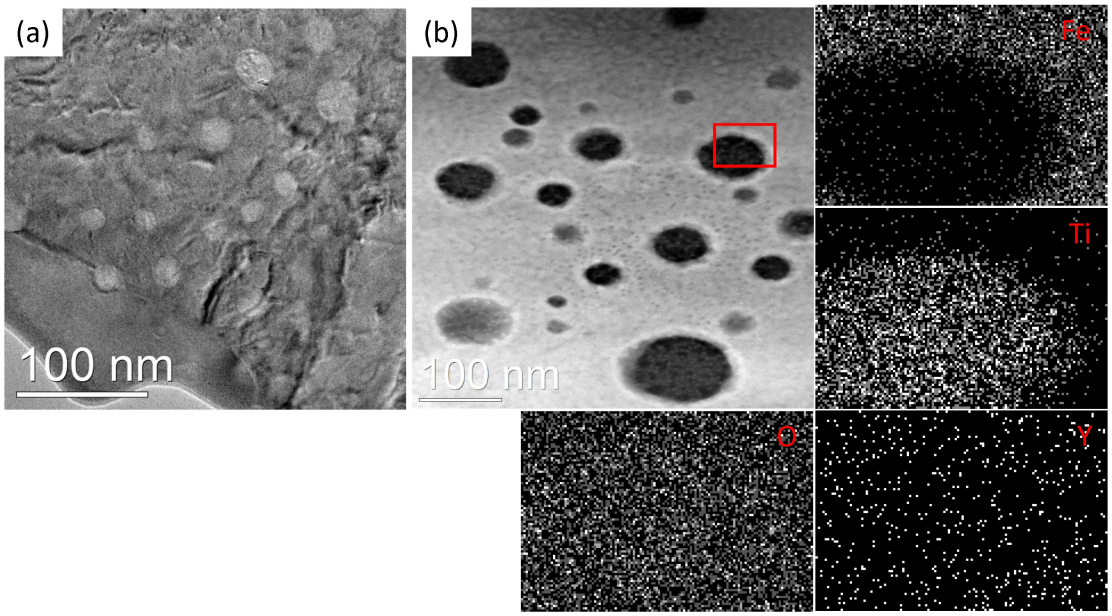

Figure 6.11: TEM characterisation of the MS02 ribbon after annealing at 1000 °C for 4h: (a) Bright field TEM image, (b) STEM HAADF image, with EDX elemental maps of Fe, Ti, Y and O taken around/over a typical particle labelled in the red rectangle.

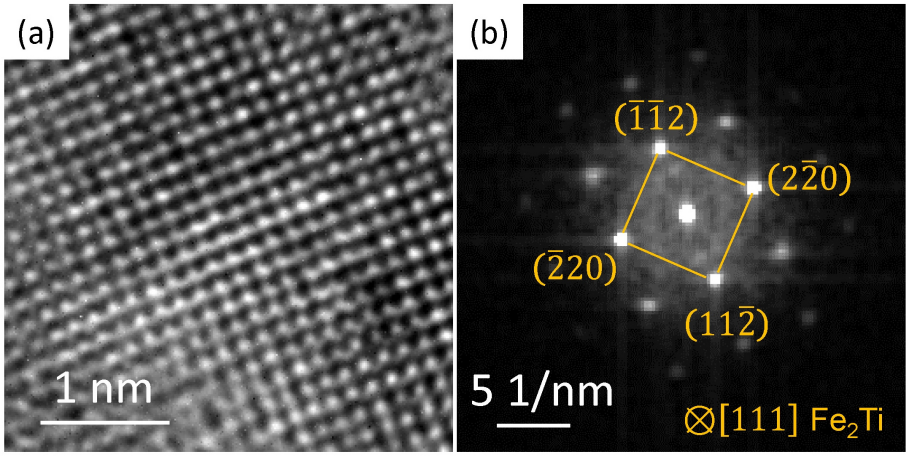

Figure 6.12: TEM characterisation of a Ti enriched particle in the MS02 ribbon after annealing at 1000 °C for 4h, showing (a) HRTEM image, and its corresponding (b) FFT image and crystallographic analysis.

6.4 MS03 (Fe-1Y-1Ti) ribbon

The MS03 ribbon was produced using the MA03 master alloy with the same Fe-1Y-1Ti (wt%) composition as the MS02 ribbon. Based on experience drawn from production of the MS02 ribbon, less reactive Fe-33.1Y (wt%) intermetallic pieces were used to replace pure Y powder in the hope of reducing Y loss during processing.

The main aim in the production of the MS03 ribbon was to validate the scalability of the melt spinning route by increasing feedstock capacity from 20 g for the MS02 ribbon to above 100 g.

6.4.1 Master alloy

The MA03 master alloy was produced by vacuum induction melting of Fe, Ti and Fe-33.1Y pieces using procedures detailed in section 3.3.2. A 1 kg ingot was produced and cut to suitably sized pieces for melt spinning.

The BSE SEM micrograph in Figure 6.13a shows the MA03 master alloy had a typical cast cellular/dendritic microstructure with darker contrast of the interdendritic region, suggesting segregation of elements lighter in molecular weight than the Fe matrix, which was consistent with the Ti concentration revealed in the corresponding EDX elemental maps in Figure 6.13b to e. Although there was relatively weak Y enrichment in the interdendritic region, Y was mostly concentrated in μm-sized particles (labelled in the red circle in Figure 6.13c) that were also comparatively enriched in O. This co-location suggested a significant fraction of the Y was tied up in the formation of probably undesirable coarser Y oxides. A likely reason was oxidation of reactive Y with Al_2O_3 used in the crucible, which was promoted by the relatively long holding time and slow cooling rate of the melting process. As previously highlighted, Y is well known in the foundry industry for its inter-reaction with almost all practical crucible materials based on oxide ceramics.

Away from the Y-rich oxides, the average Ti and Y concentrations taken from the EDX elemental maps were 1.0 ± 0.01 wt% and 0.9 ± 0.02 wt% respectively, which was considered sufficient to explore their subsequent behaviour on heat treatment.

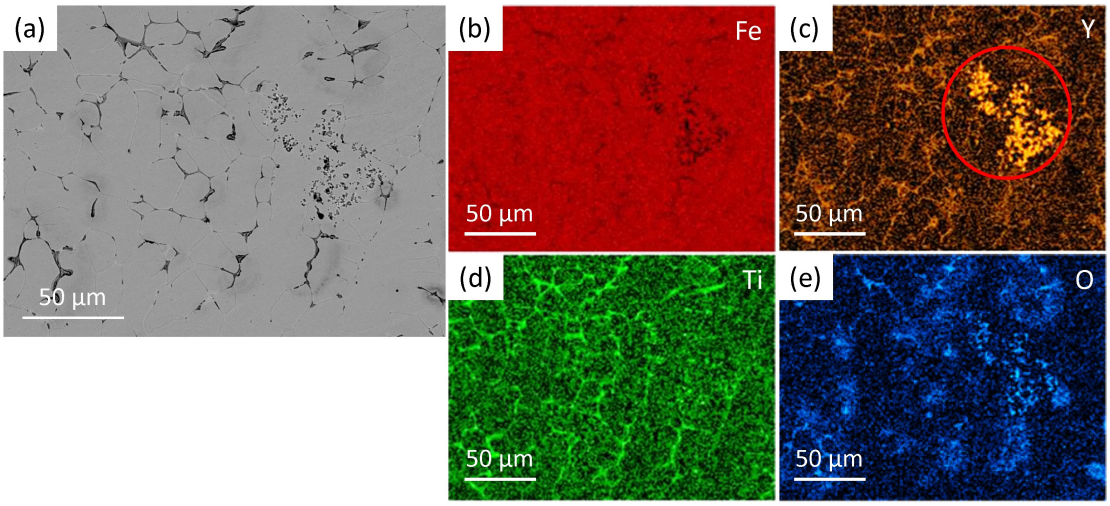

Figure 6.13: SEM characterisation of the MA03 master alloy: (a) BSE SEM micrograph with corresponding EDX elemental maps of (b) Fe, (c) Y, (d) Ti, and (e) O.

6.4.2 Melt spun ribbon

The MS03 ribbon had a thickness of approximately 25 µm, which was comparable with the earlier smaller scale MS01 and MS02 ribbons. The low magnification SE SEM micrograph in Figure 6.14a revealed the ribbon had µm-sized grains at the wheel side, which were then progressively larger until a transition into columnar grains, according the release of latent heat and increasing distance from the wheel. The smaller diameter, wheel-side grains are more clearly depicted at higher magnification in Figure 6.14b with the equiaxed polygonal grains ranging from 1 to 2 µm. These grains were still slightly coarser than those of MS01 and MS02 ribbons, and probably due to a reduced cooling ability due to the use of a larger crucible nozzle slot size so that the melt flow rate onto the wheel was increased and run times reduced. Since nano-sized (< 100 nm) Y oxides were reported to be formed from melt spun Cu-0.33Y ribbons with similar sized as-spun grains, again encouragement was inferred from this set of results [60].

However, Figure 6.14b also showed some relatively coarse grain boundary particles with relatively high Y and O concentrations, which were suggestive of Y_2O_3 stoichiometry according to EDX point measurements. Their similar size, morphology and chemical composition to the coarser Y oxides seen in the MA03 master alloy

suggested that these Y-rich oxides were carried over from the master alloy. Pores in areas such as those highlighted by the yellow circles in Figure 6.14a and b were most likely caused by particle pull-out during SEM sample preparation, and were most likely these coarser Y-rich oxides formed in the master alloy preparation.

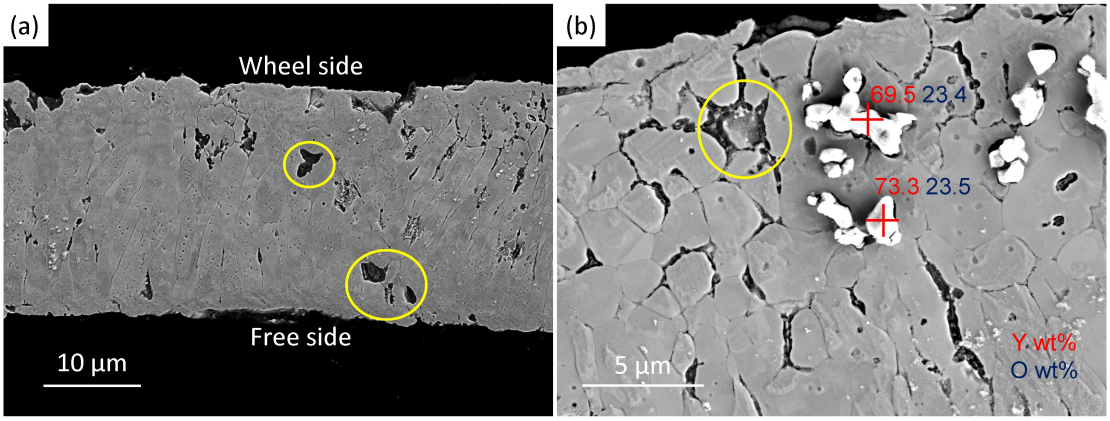

Figure 6.14: SE SEM micrographs showing the cross-section microstructure of the MS03 ribbon. (a) low magnification overview, and (b) detailed wheel side microstructure at higher magnification with Y (red) and O (blue) approximate concentrations (wt%) of EDX point analyses labelled in red crosses.

Figure 6.15 shows EDX elemental maps taken from the MS03 ribbon with Y primarily concentrated in the µm-sized oxides. In comparison, Ti was distributed relatively evenly across the ribbon, showing that the pronounced inter-dendritic segregation of Ti in the cast MA03 master alloy did not develop at the much higher solidification speeds of melt spinning.

Overall, the production of MS03 ribbon confirmed scalability of the melt spinning process to above 100 g feedstock capacity, if bulk melting of Y-containing alloys without excessive formation of the µm-sized oxides can be achieved. The use of Fe-Y intermetallics successfully reduced Y loss in master alloy production. The Y-rich oxides were formed probably by reaction with the Al_2O_3 containing crucible, which is less thermodynamically stable than Y_2O_3 at the melt temperature, as shown in the Ellingham diagram in Figure 6.16 [146]. Scale-up of the BN crucibles used with low Y-

rich oxide formation successfully at smaller scale should be feasible, but was too expensive and too time consuming to be pursed in this thesis.

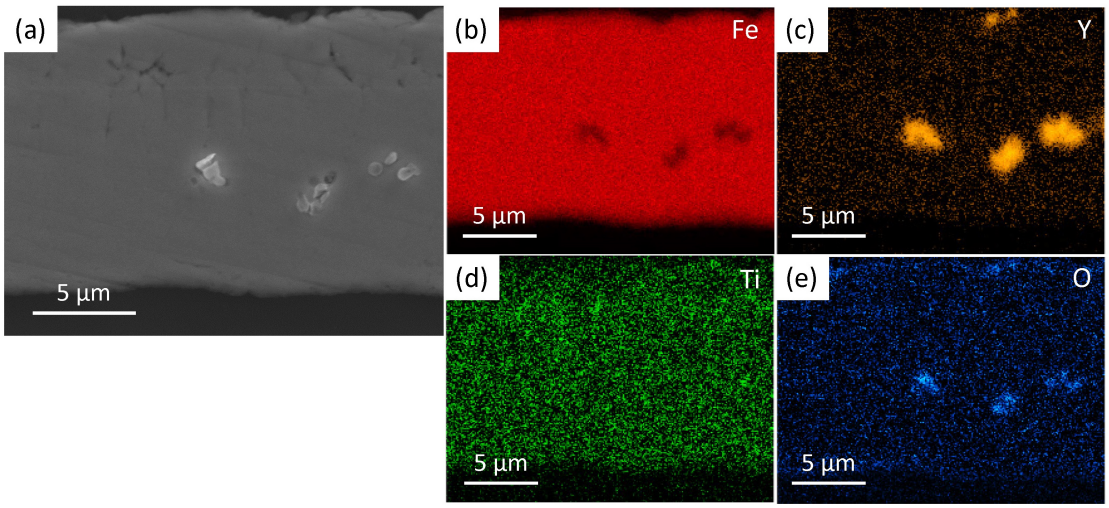

Figure 6.15: SEM characterisation of the MS03 ribbon: (a) SE SEM micrograph and its corresponding EDX elemental maps of (b) Fe, (c) Y, (d) Ti and (e) O.

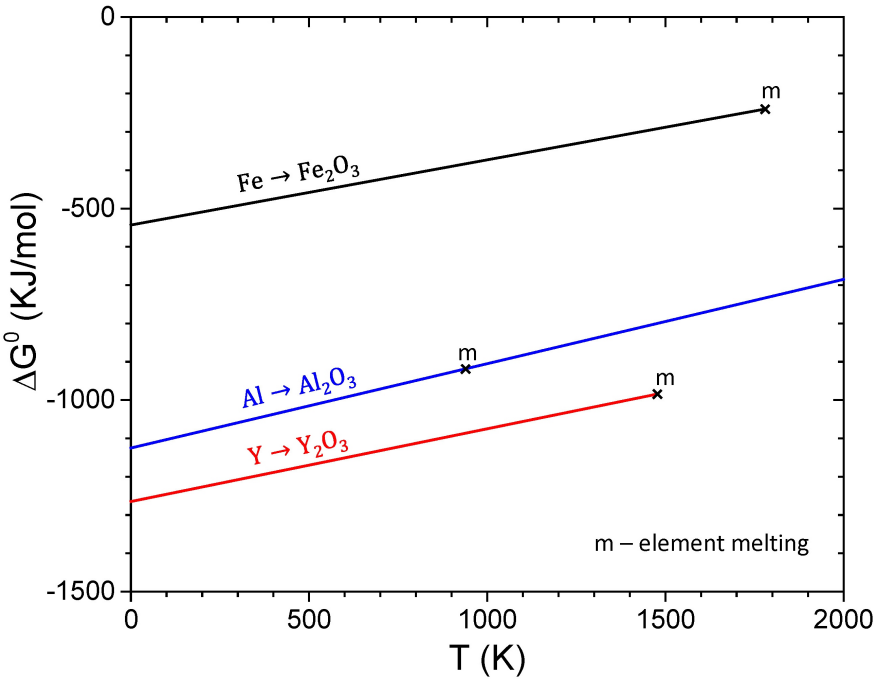

Figure 6.16: Ellingham diagram for Fe_2O_3, Al_2O_3 and Y_2O_3. Data from [146]

6.5 MS04 (Fe-1Y-1Ti) ribbon

The MS04 ribbon was produced using the same Fe-1Y-1Ti (wt%) composition and raw materials as MS03. The only difference was the use of arc melting with a water cooled

Cu die in production of the MA04 master alloy to minimise risk of Y oxidation previously occurred in production of MA03. This limited master alloy production to approximately 120 g per run.

6.5.1 Master alloy

As shown in Figure 6.17a, the MA04 master alloy displayed similar dendritic structure as MA03, although the brighter contrast of the inter-dendritic region in the BSE SEM micrograph indicated segregation of an element of higher atomic weight than the Fe matrix, which was confirmed in the corresponding EDX elemental maps (Figure 6.17b – e) as Y.

Unlike MA03, MA04 had a comparatively homogeneous Ti distribution, probably due to the higher cooling rate of the arc melting process, which used a water-cooled hearth. O concentration approximated from sum of the EDX maps were reduced from 1.3 ± 0.02 wt% for MA03 to 0.4 ± 0.02 wt% for MA04. There was much more limited O enrichment in inter-dendritic regions for MA04.

The overall, approximate Y and Ti concentrations derived from the EDX elemental maps were 0.7 ± 0.02 wt% and 1.1 ± 0.01 wt% respectively, demonstrating excellent retention of both Y and Ti. Qualitatively, it was confirmed that Y was preserved primarily in inter-dendritic segregations rather than in µm-sized oxides, proving arc melting as a more suitable technique for master alloy production.

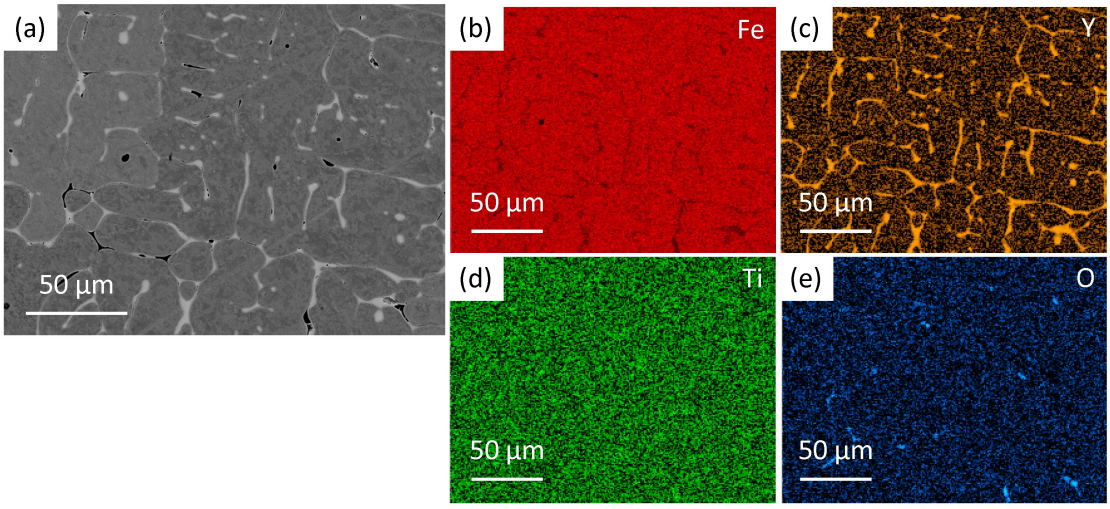

Figure 6.17: SEM characterisation of the MA04 master alloy: (a) BSE SEM micrograph and the corresponding EDX elemental maps of (b) Fe, (c) Y, (d) Ti and (e) O.

6.5.2 Melt spun ribbon

Using the improved MA04 master alloy, the MS04 ribbon was free of coarser oxides, as shown in SE and BSE SEM micrographs in Figure 6.18a and b. The ribbon had similar grain sizes as the MS03 ribbon, which comprised µm-sized grains at the wheel side, columnar grains following the heat flow and a small amount dendritic structure towards the free side.

EDX elemental maps in Figure 6.18d to f taken from a ribbon cross-section demonstrated a relatively uniform distribution of both Y and Ti, with overall concentrations measured at 0.6 ± 0.04 wt% and 1.0 ± 0.02 wt% respectively. The results were in good agreement with Y and Ti concentrations measured from the EDX line scan conducted across the thickness of the ribbon in Figure 6.18c. The EDX line scan also revealed fluctuations in Ti and Y concentrations larger than those measured in the nanocrystalline MS02 ribbon, suggesting that the larger grain sizes obtained at

longer solidification times also allowed more time for inter-dendritic segregation, as can be expected.

Overall, the production of MS04 ribbon showed that Y and Ti could be retained at useful concentrations successively, with a relatively uniform distribution in the ribbon, and without a significant population of coarse Y-rich oxides.

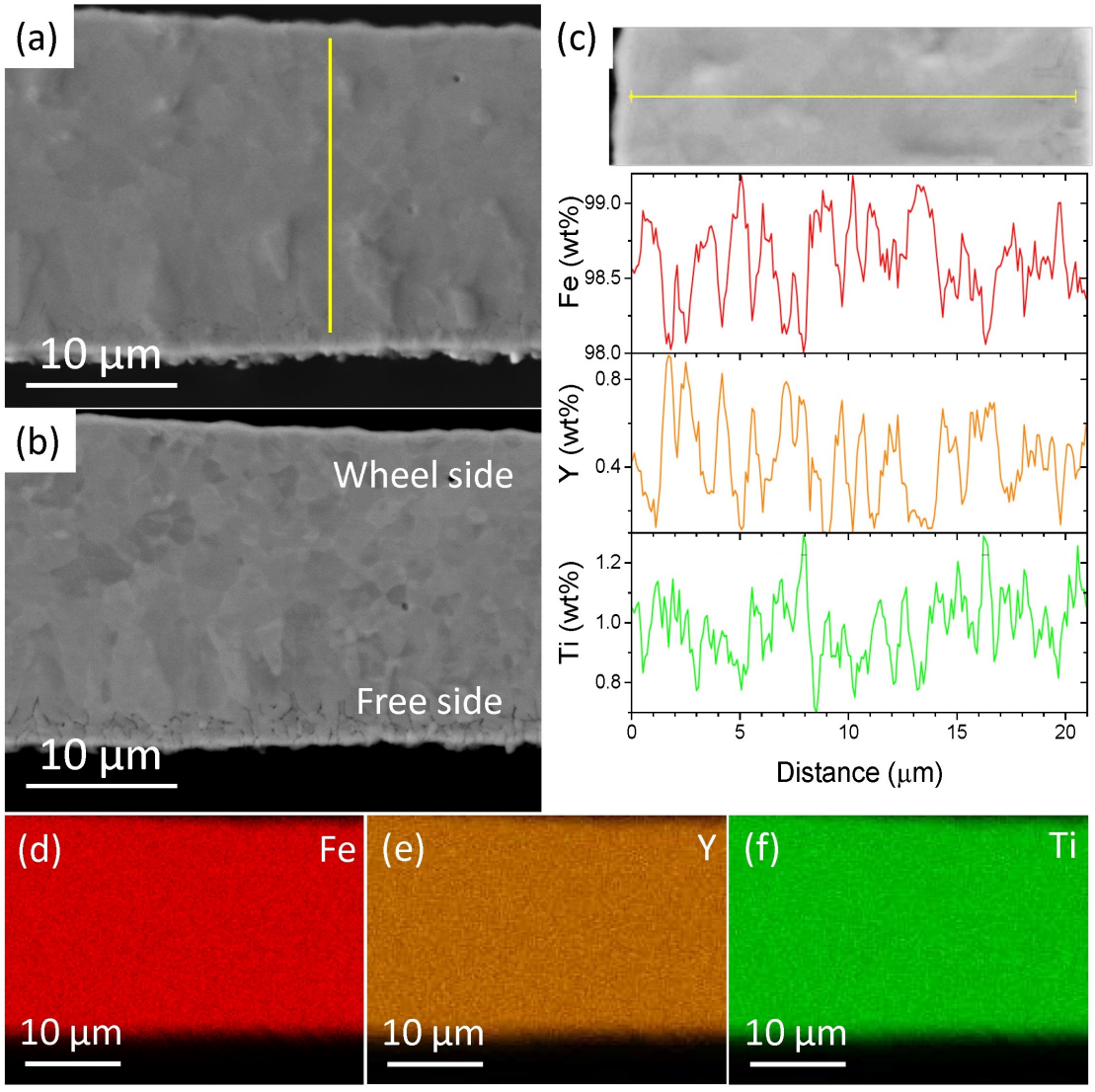

Figure 6.18: SEM characterisation of the MS04 ribbon in cross-section: (a) SE and (b) BSE SEM micrographs with corresponding EDX elemental maps showing distributions of (d) Fe, (e) Y and (f) Ti. The yellow line in (a) labels an EDX line scan across the ribbon thickness, of which the Fe, Y and Ti concentrations against scanning distance are plotted in (c).

6.6 Summary

The MS01, MS02, MS03 and MS04 ribbons were produced using master alloys with model compositions of Fe-5Y and Fe-1Y-1Ti (wt%). Microstructural characterisation of the as-spun ribbons showed a relatively uniform spatial distributions of Y and Ti in an Fe matrix, the scale of which was related to the grain size, which was qualitatively linked to the speed of solidification.

The process demonstrated good scalability and repeatability across equipment in three different institutions. The yield of master alloy to ribbon, by weight, was consistently above 60%. Melt ejection times were typically less than 10 s, showing potential of achieving significantly higher throughput compared with the conventional MA.

Internal oxidation of the MS01 ribbon validated the potential for forming nano-sized (< 20 nm) Y oxides, while annealing of the MS02 ribbon suggested the formation of nano-sized Fe_2Ti particles in the early stages of heat treatment a possible reason for particle refining effects of Ti.

The quality of the as-spun ribbon was heavily dependent on the quality of the master alloy, and issues, including loss and oxidation of Y, were significantly resolved by using arc melting and less reactive Fe-Y intermetallics in the feedstock materials.

Overall, the MS04 ribbon with a Fe-1Y-1Ti composition was produced with satisfactory properties, and the relatively large feedstock capacity ensured enough ribbon (~ 90 g) was produced for subsequent studies.

7 Bulk alloy production

7.1 Introduction

This chapter describes the production of 'bulk' alloys using the MS04 melt spun ribbons, their microstructural analyses, and their microhardness investigation.

Three alloys were produced, of which alloy BA01 was consolidated using FAST from pulverised MS04 ribbon without addition of an extra O source. This alloy was used as a reference/baseline to help understand the consolidation behaviour of the other alloys. For alloy BA02, nano-sized (15 – 20 nm) Fe_3O_4 powder as an O source analogous to the Rhines pack approach [105], was blended with the MS04 ribbons during pulverisation and consolidated using the same parameters as BA01 to investigate any simultaneous internal oxidation during consolidation. Alloy BA02 was then also vacuum annealed, and designated as BA03, to promote completion of any solid-state reactions between Y, Ti and O, and to investigate the stability of the Fe matrix and any particles formed.

Detailed processing procedures were presented in section 3.3, and the microstructure characterisation and microhardness tests were carried out according to the procedures described in sections 4.1 and 4.5.

7.2 Alloy BA01

After preliminary runs for FAST parameter optimization for pressure, temperature, current, voltage and sintering time, Figure 7.1a shows a consolidated BA01 disc or small billet of approximately 2 cm in diameter and 8 mm in thickness was achieved. The stitched low magnification BSE SEM micrograph (Figure 7.1b) of a cross-section across a diameter demonstrates apparently dense consolidation without apparent pores after 30 min at 1000 °C and 50 MPa. The sintering was conducted using a high direct current (up to 1.2 kA) at low voltage (up to 4 V). The use of a graphite die during sintering resulted in formation of darker contrast carbon diffusion layer around the surface of the billet, of up to 700 μm thickness, as highlighted by the yellow lines and

arrows in Figure 7.1b. The thickness of the carbon diffusion layer was similar to those in ODS steels produced from conventional MA powder using similar FAST parameters [147].

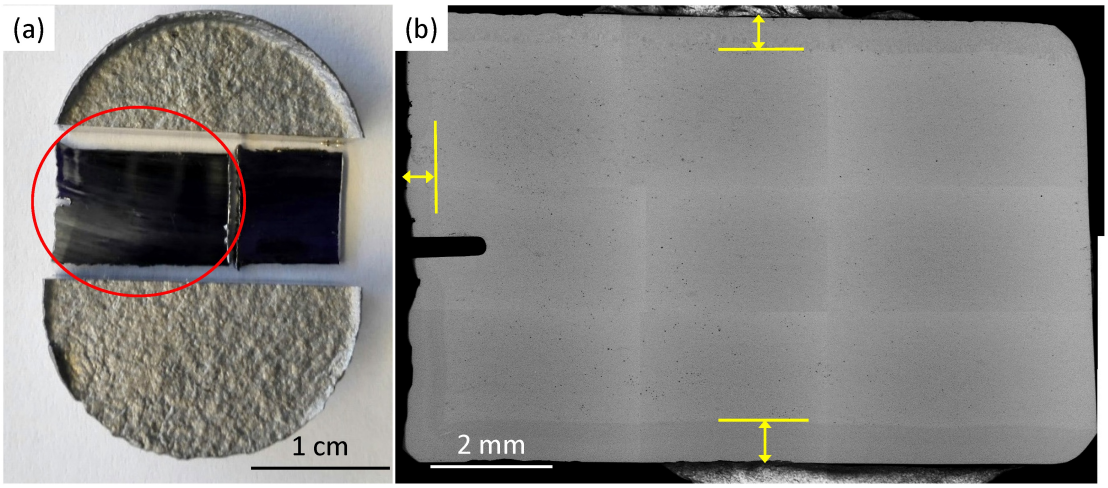

Figure 7.1: (a) Image of the BA01 billet with cross section of cut-off pieces showing its thickness. The red circle corresponded to stitched low magnification BSE SEM micrograph in (b), with yellow lines and arrows marking the approximate thickness of a carbon diffusion layer.

The BSE SEM micrograph in Figure 7.2a shows alloy BA01 contained relatively coarse (> 5 µm) particles, and a layered structure delineated by boundaries of darker contrast. Since the thickness of each layer resembled those of the MS04 ribbons, the boundaries likely reflected the prior ribbon structure. At higher magnification, Figure 7.2b shows this boundary layer comprised a series of < 500 nm particles of darker contrast, while similar sized, brighter particles were also formed inside each layer. The contrast variations are more clearly depicted in Figure 7.2c and d, indicating different compositions between the two types of particles. In addition, the channelling contrast of BSE SEM micrographs in Figure 7.2c and d indicated small grain sizes, which were barely resolvable by SEM imaging.

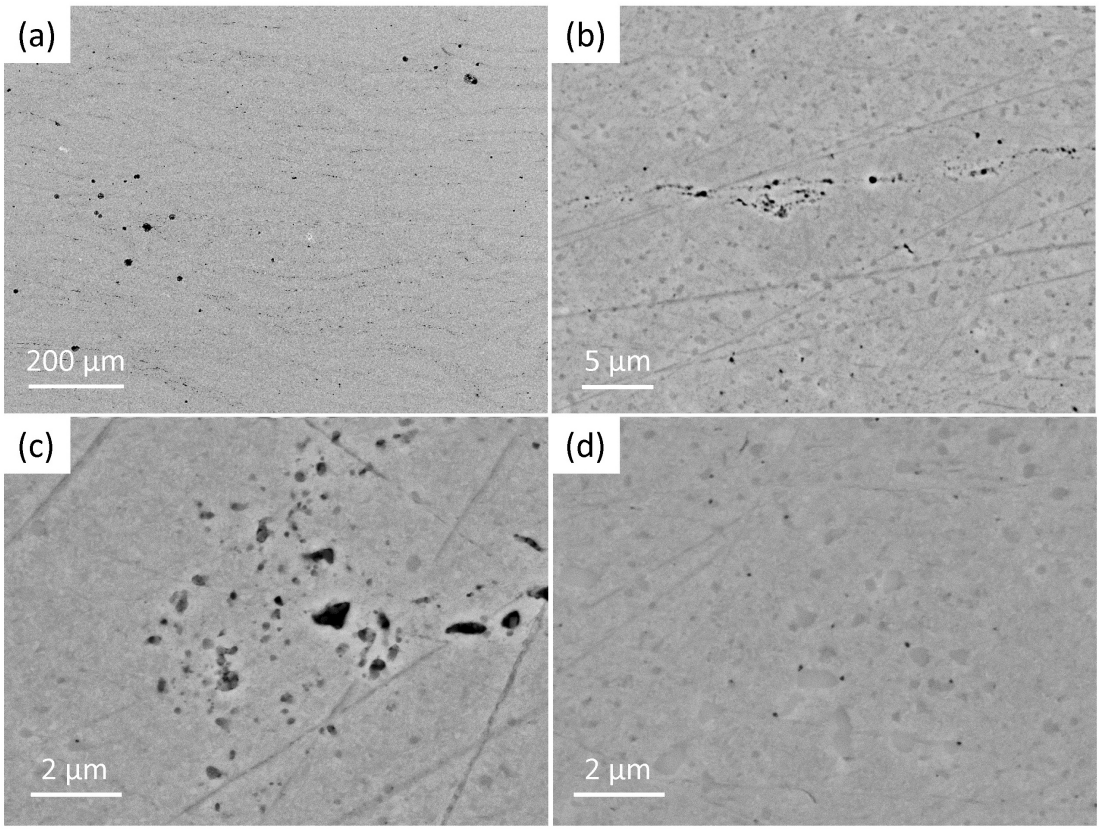

Figure 7.2: BSE SEM micrographs of alloy BA01, showing (a) coarse particles and a layered structure, (b) a layer boundary, (c) layer boundary particles and (d) in-layer particles.

The low magnification EDX elemental maps in Figure 7.3 show alloy BA01 had relatively even distributions of Y and Ti, apart from a number of concentrations into the coarse > 5 µm particles, which were confirmed as Y and Ti enriched oxides by the EDX line scans in Figure 7.4. The Y and Ti concentrations from sum spectrum of the EDX elemental maps were measured at 0.8 ± 0.04 wt% and 1.0 ± 0.02 wt% respectively, showing good retention of both elements, while the O concentration (with reduced accuracy [106]) of 0.4 ± 0.04 wt% was suggestive of O absorption during ribbon handling, pulverisation and consolidation.

The EDX line scan of representative < 500 nm particles on a prior ribbon boundary in Figure 7.5b showed they were Y and Ti enriched oxides, similar to the > 5 µm coarse particles discussed above. On the other hand, Figure 7.5c shows other particles within the prior ribbon structure were concentrated only in Y, without apparent enrichment of

Ti or O, suggesting the particles may have been Fe-Y intermetallics. The results were consistent with contrast variations between the two types of particle in the BSE SEM micrograph in Figure 7.2b, and also explained the Y concentration spikes (highlighted in the red circle) in the line-scans in Figure 7.4c, where co-location of Ti or O enrichment was not detected.

Overall, alloy BA01 showed dense consolidation could be achieved from pulverised melt spun ribbons using FAST. O was picked-up, most likely in the form of ribbon surface oxidation during handling, pulverisation and consolidation, which resulted in the formation of Y and Ti enriched oxides on prior ribbon boundaries. However, the persistence of Fe-Y intermetallic particles within prior ribbons, and the suggestion of at least some Y retained in solution, indicated that the O up-take did not lead to full oxidation of Y and Ti.

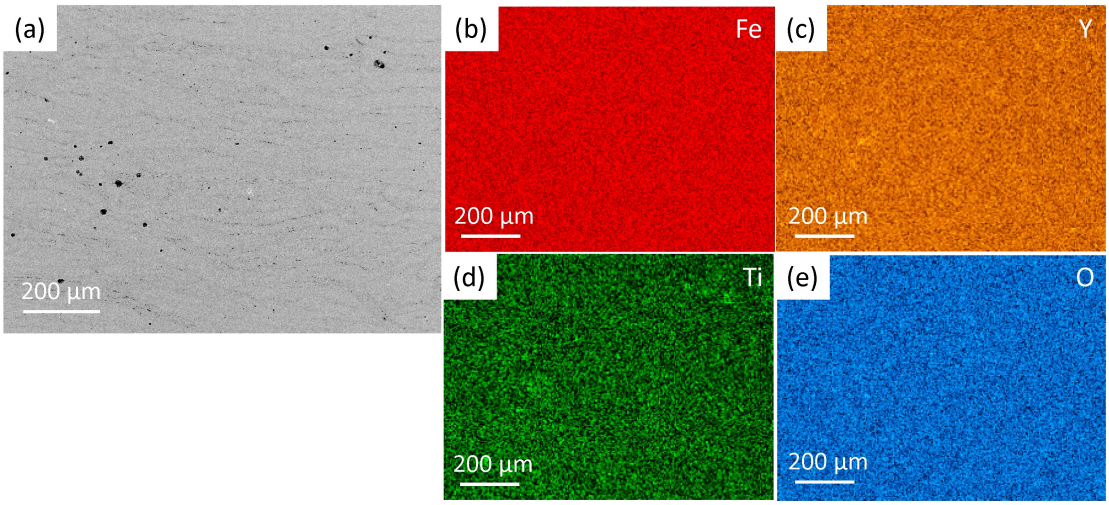

Figure 7.3: SEM characterisation of alloy BA01: (a) BSE SEM micrograph with corresponding EDX elemental maps of (b) Fe, (c) Y, (d) Ti and (e) O.

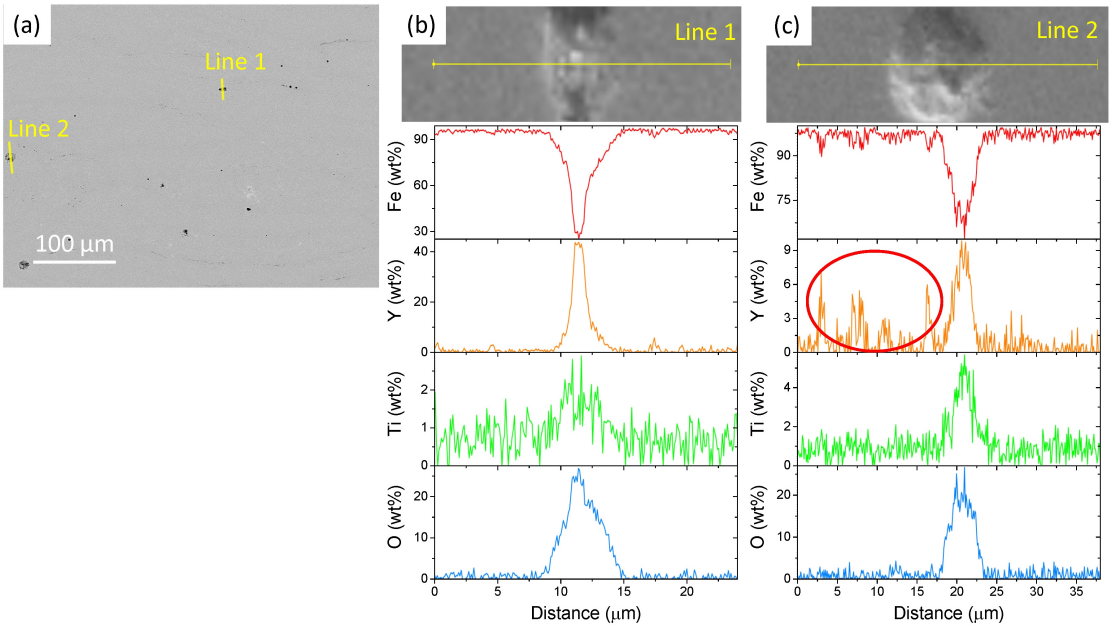

Figure 7.4: SEM characterisation of alloy BA01: (a) BSE SEM micrograph with yellow lines labelling EDX line scans of two representative coarse particles, of which the Fe, Y, Ti and O distributions are plotted against line scan distance in (b) and (c).

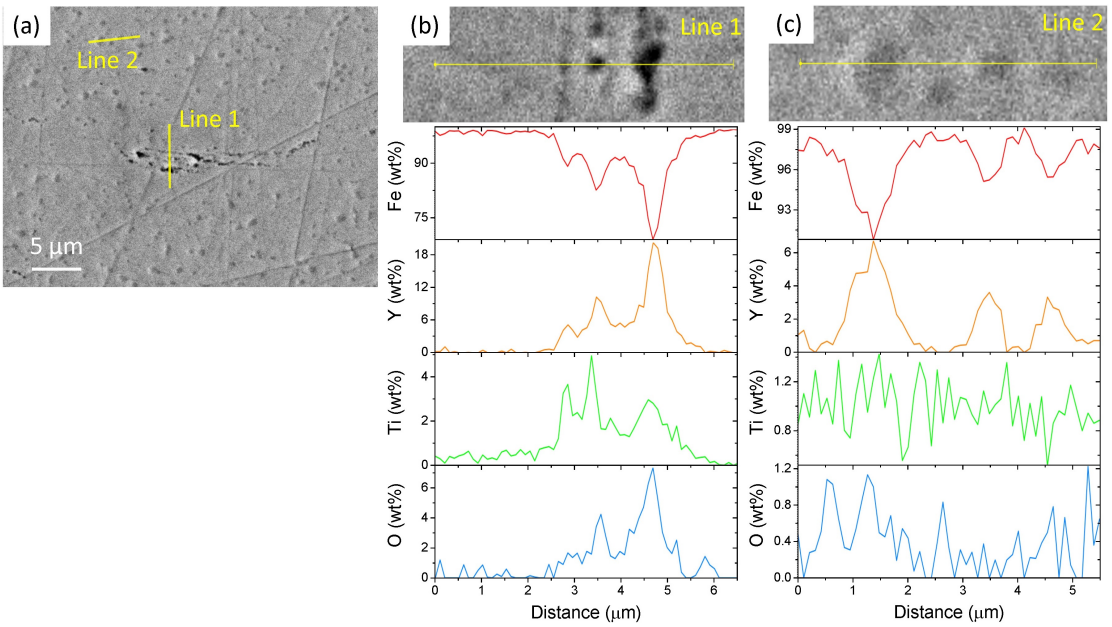

Figure 7.5: SEM characterisation of alloy BA01: (a) SE SEM micrograph with yellow lines labelling EDX line scans of representative particles on a prior ribbon boundary and within prior ribbon structure, of which the Fe, Y, Ti and O distributions are plotted against line scan distance in (b) and (c).

7.3 Alloy BA02

Figure 7.6a shows the BA02 billet had comparable dimensions with the BA01 billet. However, unlike BA01, the stitched low magnification BSE SEM micrograph in Figure 7.6b revealed > 10 μm pores, primarily concentrated towards the peripheral surface of the cylindrical billet, in layers of up to 1.7 mm thickness. Since BA02 was produced using the same MS04 ribbons and pulverisation/consolidation parameters as BA01, the 1.8 wt% nano-sized Fe_3O_4 powder added to promote the oxidation of unbound Y and Ti in solution of the MS04 ribbons may have contributed to the reduced sinterability. Although the exact reason was not clear, a possible argument might be that the added oxide particles in BA02 reduced conductivity of the powder mix and subsequently increased current 'leaks' through the graphite die under the same FAST parameters as BA01 [148]. The current going through the powder mix was therefore reduced, resulting in reduction in Joule heating effects and sinterability.

All the FAST billets suggested reduced consolidation at the periphery, and similar results are reported for other FAST materials in the group and elsewhere [149]. The inevitable carbon diffusion and possible hardening using a graphite die may have inhibited consolidation, and the reduced temperature at the periphery due to current flow and heat losses to the graphite die may have resulted in insufficient heating [150,151]. Nevertheless, most of the small billet was consolidated with only a small amount of > 10 μm pores remaining, suggesting that the addition of the Fe_3O_4 powder was generally acceptable.

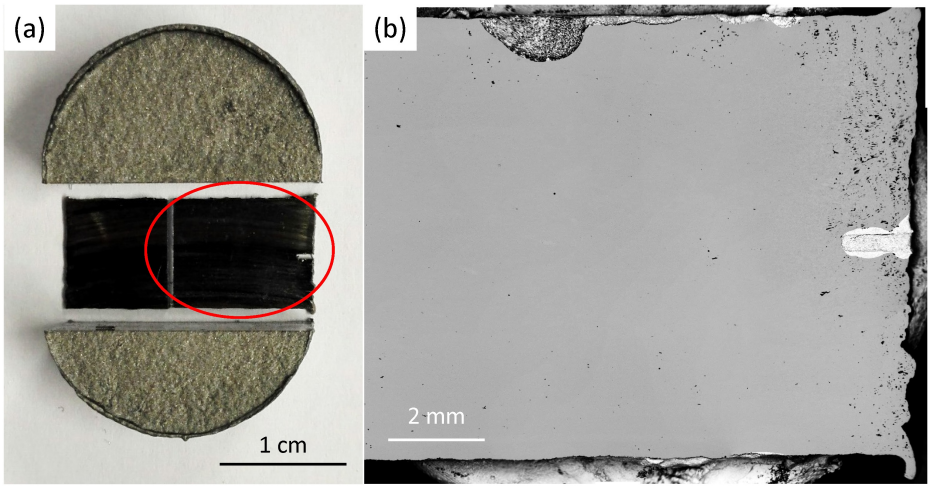

Figure 7.6: (a) Image of the BA02 billet with cross-sectioned cut-off pieces. The red circle highlights the section corresponding to the stitched low magnification BSE SEM micrograph in (b).

The BSE SEM micrograph in Figure 7.7a shows alloy BA02 retained a layered structure after consolidation, similar to alloy BA01, although the layer boundaries were now less pronounced. The higher magnification micrograph in Figure 7.7b reveals the contrast variations were primarily caused by differences in particle number density between layers. Almost all the particles were smaller than 1 μm, and a higher number of particles were formed in BA02 compared with BA01. As shown in Figure 7.7c and d, particles larger than 300 nm were particularly prevalent in the comparatively high particle number density layers, while regions of relatively low particle number density mainly contained particles smaller than 150 nm. Noticeably, the channelling contrast of BSE SEM micrographs in Figure 7.7c and d indicated alloy BA02 had a nanocrystalline grain structure, with these small grains just resolvable.

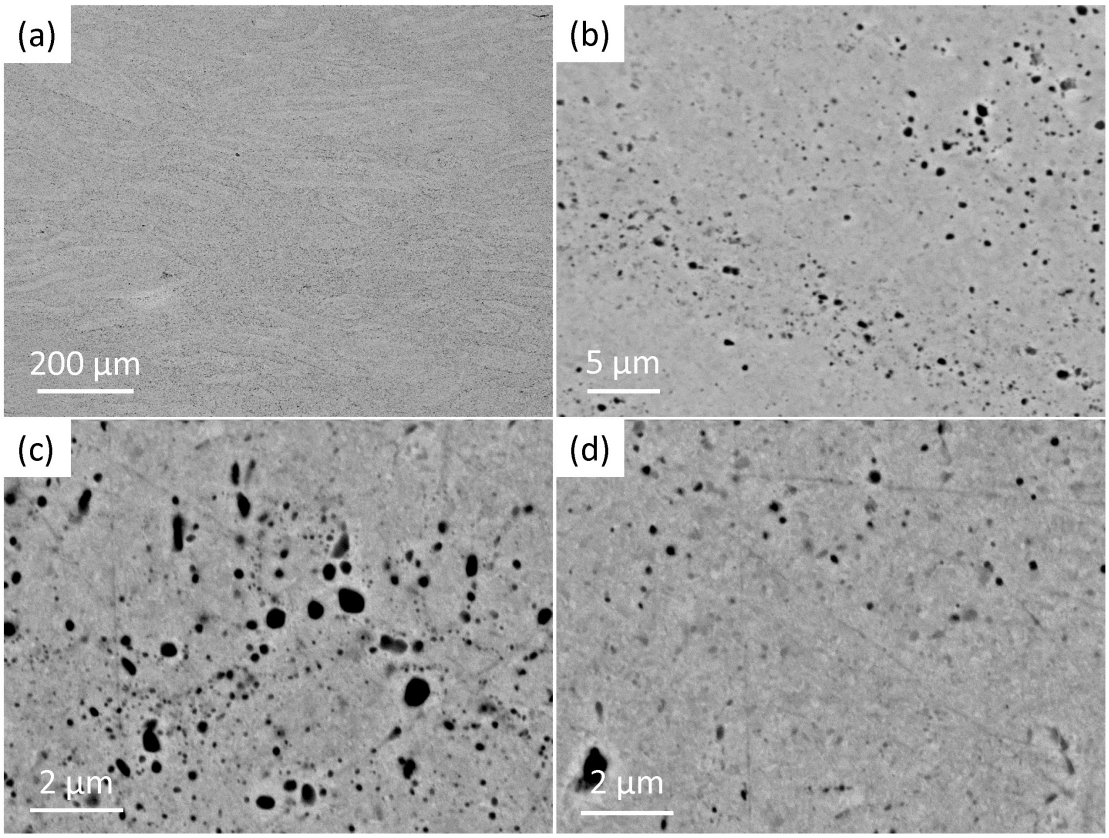

Figure 7.7: BSE SEM micrographs of alloy BA02, showing (a) layered structure, (b) variations in particle number density between layers, (c) a layer with high particle number density, and (d) a layer with low particle number density.

The low magnification EDX elemental maps from alloy BA02 in Figure 7.8 show that the layers with higher particle number density were enriched in Ti, while Y was distributed relatively homogeneously. The sum spectrum of the EDX elemental maps suggested approximate Y and Ti concentrations comparable with those of BA01, while O concentration was increased to 1.1 ± 0.05 wt% due to the added O source provided by the Fe_3O_4. At higher magnification, the EDX area measurements in Figure 7.9 strengthened evidence for Ti enrichment in areas with higher particle number density and depletion in areas sparsely populated with particles. There were similar patterns of co-located concentrations of O, which could not be reliably detected at low magnification. The Y concentration, on the other hand, was maintained approximately uniform. Because both Y and Ti in solution of the MS04 ribbons were relatively uniformly distributed (section 6.5.2), Y may have more sluggish diffusion than Ti at the

FAST consolidation temperature and conditions. An EDX line scan of a representative particle in the Ti enriched region in Figure 7.10b shows a Y and Ti enriched oxide, while Y-based oxides, without apparent Ti concentration, were found in a Ti depleted region (Figure 7.10c). Fe-Y intermetallics present in BA01 were not present in BA02, indicating Y has preferentially reacted with O. Noticeably, residual Fe_3O_4 particles were not observed in BA02 after consolidation, suggesting the O source was completely reduced or at least to a state containing much less O that could not be easily resolved by SEM BSE contrast.

Overall, production of alloy BA02 by FAST suggested that melt spun ribbons could be simultaneously internally oxidised during consolidation, and generated a high number density of sub-micron Y and/or Ti enriched oxides. Nano-sized Fe_3O_4 powder was suggested to be an effective O source, resulting in relatively even oxidation of Ti and Y. Porosity was suggested to be slightly higher when Fe_3O_4 was used and internal oxidation took place, and could likely be eradicated with re-optimised sintering parameters such as a higher temperature, pressure and longer consolidation time [11]. Nonetheless, at fine-scale, the prior ribbon structure persisted and was delineated by variations in particle number density, which were positively correlated with Ti and O enrichment. Since similar Ti concentration variations were not detected in ribbons, preferential diffusion of Ti over Y under the higher O partial pressure and FAST conditions was implied. As Ti diffused to the prior ribbon boundary, oxides were nucleated, and the larger > 300 nm oxides were thus primarily Ti rich. Growth of the Ti-rich oxides after nucleation subsequently drew Ti from adjacent regions through further diffusion, and resulted in Ti depleted zones in the layered structure. The faster diffusion of Ti than Y in alloy BA02 was consistent with studies on ODS steels produced by conventional and novel powder processing routes, where Ti enrichment was typically formed on prior particle boundaries [142,147]. Although oxides occurred with some

layered distribution, the large (> 5 µm) oxides, which characterised other ribbons (sections 6.2 and 6.3) and consolidated alloy BA01, were not present here.

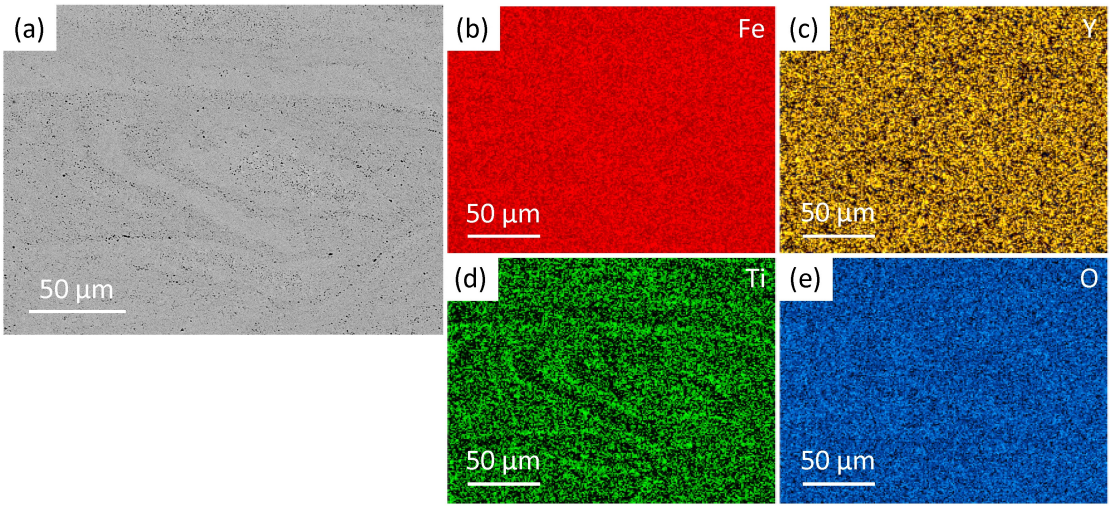

Figure 7.8: SEM characterisation of alloy BA02: (a) BSE SEM micrograph with corresponding EDX elemental maps of (b) Fe, (c) Y, (d) Ti and (e) O.

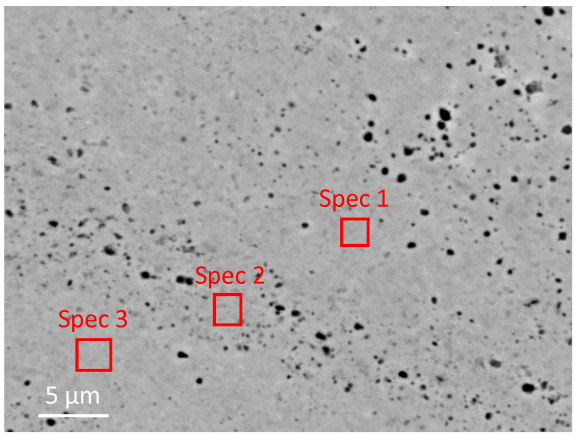

	Spec 1	Spec 2	Spec 3
Fe	98.6 ± 0.3	96.9 ± 0.3	98.8 ± 0.2
Y	0.8 ± 0.2	0.6 ± 0.2	0.6 ± 0.2
Ti	0.4 ± 0.06	1.5 ± 0.07	0.3 ± 0.06
O	0.2 ± 0.2	1.1 ± 0.2	0.3 ± 0.2

Figure 7.9: BSE SEM micrograph of alloy BA02 including regions of relatively low and high particle number density. EDX area measurements were from within the red rectangles with corresponding Fe, Y, Ti and O concentrations summarised on the right.

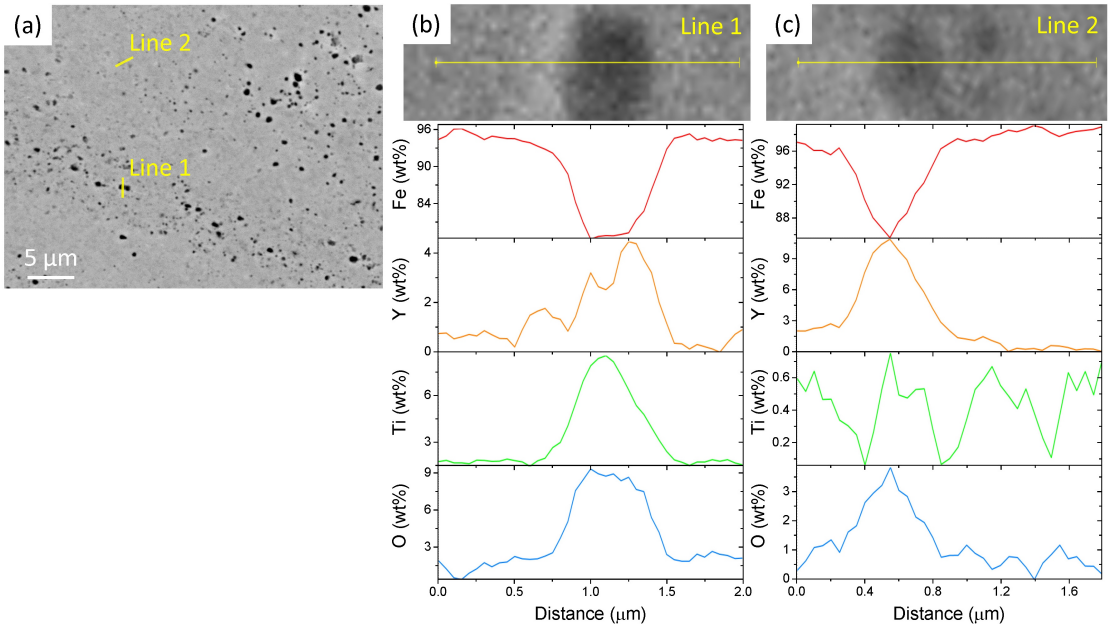

Figure 7.10: SEM characterisation of alloy BA02: (a) BSE SEM micrograph with yellow lines showing the EDX line scans across two representative particles, of which the Fe, Y, Ti and O distributions are plotted against line scan distance in (b) and (c).

7.4 Alloy BA03

A piece of alloy BA02 was vacuum annealed (< 1 x 10^{-4} mbar) at 700°C for 4h (designated as alloy BA03) to investigate any ongoing reactions between Y, Ti and O after the relatively fast sintering/internal oxidation process. The heat treatment also enabled studies on stability of the sub-micron Y and Ti enriched oxides and the nanocrystalline grain structure after exposure to elevated temperature.

As shown in Figure 7.11a, a BA02 piece adjacent to the one analysed in the previous section was used for the heat treatment. Indeed, alloy BA03 displayed a similar porosity distribution in the stitched low magnification BSE SEM micrograph (Figure 7.11b) after annealing.

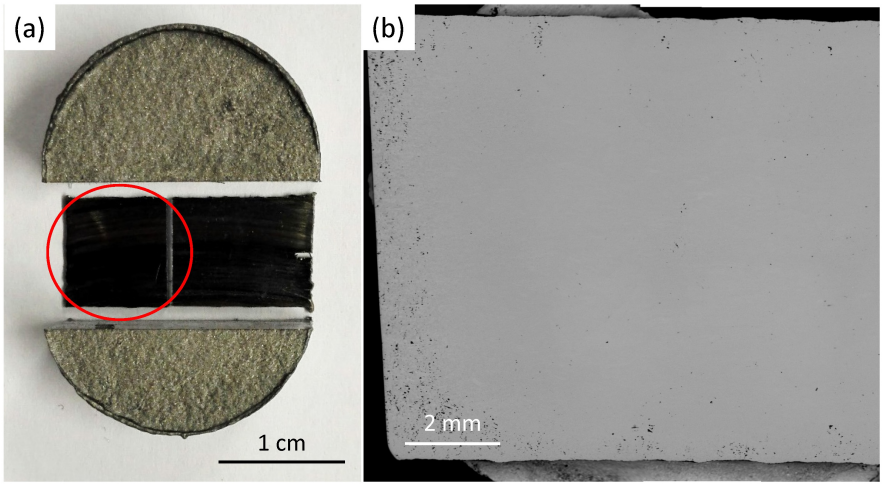

Figure 7.11: (a) Image of the BA02 billet. The red circle highlights the section that was vacuum annealed, and designated as alloy BA03, with the corresponding stitched low magnification BSE SEM micrograph in (b).

Figures 7.12a and b show the layered structure persisted in BA03, with variations in particle number density that were similar to those already described for BA02. The two types of oxide particle in BA02 appeared stable without apparent growth after annealing. At higher magnification, Figure 7.12c reveals the possible formation of a new population of < 50 nm particles (highlighted by red circle), probably due to ongoing oxidation of residual Y and Ti. However, it was hard to ensure constant imaging conditions between samples and these particles may simply have been easier to resolve in this particular specimen. In addition, the channelling contrast in Figure 7.12c shows grain sizes in hundreds of nm, which were certainly larger than those in BA02.

The sub-micron grains of BA03 were investigated further by EBSD analysis covering an area of 40 x 80 µm with a step size of 80 nm. The false coloured EBSD IPF map in Figure 7.13a suggests that the columnar, through-thickness orientation of as-spun grains (section 6.5.2) were fully recrystallized to sub-micron grains in the consolidated/annealed condition. Regions with thickness approximated to the MS02 ribbons demonstrated preferred texture in predominantly green or pink colours, suggesting texture variation in the layered prior ribbon structure. This was likely caused by strong texture in the rapid solidified ribbons that were subsequently aligned in

different orientations during pulverisation, cold pressing and FAST consolidation. Assuming near-spheroidal grains, the grain size distribution in Figure 7.13b was uni-modal with a mean of 620 nm and a standard deviation of 210 nm. Unlike ODS steels produced by conventional MA based processing, abnormal grain growth was not observed in BA03 [10,11,122,124,125]. It was not possible to confirm the exact reason for the homogeneity of grain size, but one of the factors may be the higher (up to four times) Y and Ti concentrations compared with typical ODS steels [10,11,122,124,125], which could lead to a higher fraction of the Y and/or Ti enriched oxides that pin grain growth during consolidation. This hypothesis is consistent with Cayron et al.'s [152] investigation that an increase of Y_2O_3 concentration from 0.2 wt% to 0.8 wt% in an ODS steel produced by conventional MA based processing increased the amount of pinning oxides, and approximately halved the proportion of μm-sized coarse grains, although the bi-modal grain size distribution was not fully avoided as in BA03. Since the recrystallization of ODS steels is determined by the balance between the driving force dominated by stored energy of cold work and the retarding force exerted by the Y and/or Ti enriched oxides [122,153,154], another possible factor for the relatively homogeneous grain size distribution in BA03 may be the lower amount of work hardening for the pulverised melt spun ribbons compared with conventional MA powder, which may have reduced the driving force for recrystallization at elevated temperature during consolidation.

Comparing with BA02, the EDX elemental maps in Figure 7.14 show that BA03 had similar Ti concentrations in layers of relatively high particle number density, as well as similar Y, Ti and O concentrations approximated from the sum spectrum. At higher magnification, the EDX area measurements in Figure 7.15 suggested increased Ti and O concentrations in regions of lower particle number density, as diffusion of the relatively mobile Ti continued to react with O at the annealing condition, possibly forming the < 20 nm particles previously described.

Overall, the annealed BA03 maintained a nanocrystalline structure with a uni-modal grain size distribution despite particle number density variations among different prior ribbon layers, which might indirectly suggest a relatively homogeneous distribution of grain boundary pinning particles across the alloy in sizes below detection limit of SEM imaging. Similar < 20 nm oxides were already shown in the heat treated ribbons by TEM (section 6.2), which also could not be resolved by SEM. Unfortunately, time constraints prevented TEM studies of alloy BA03, and should take the form of further work. The likely formation of < 20 nm particles across the alloy was probably due to diffusion and reaction of residual Ti and O.

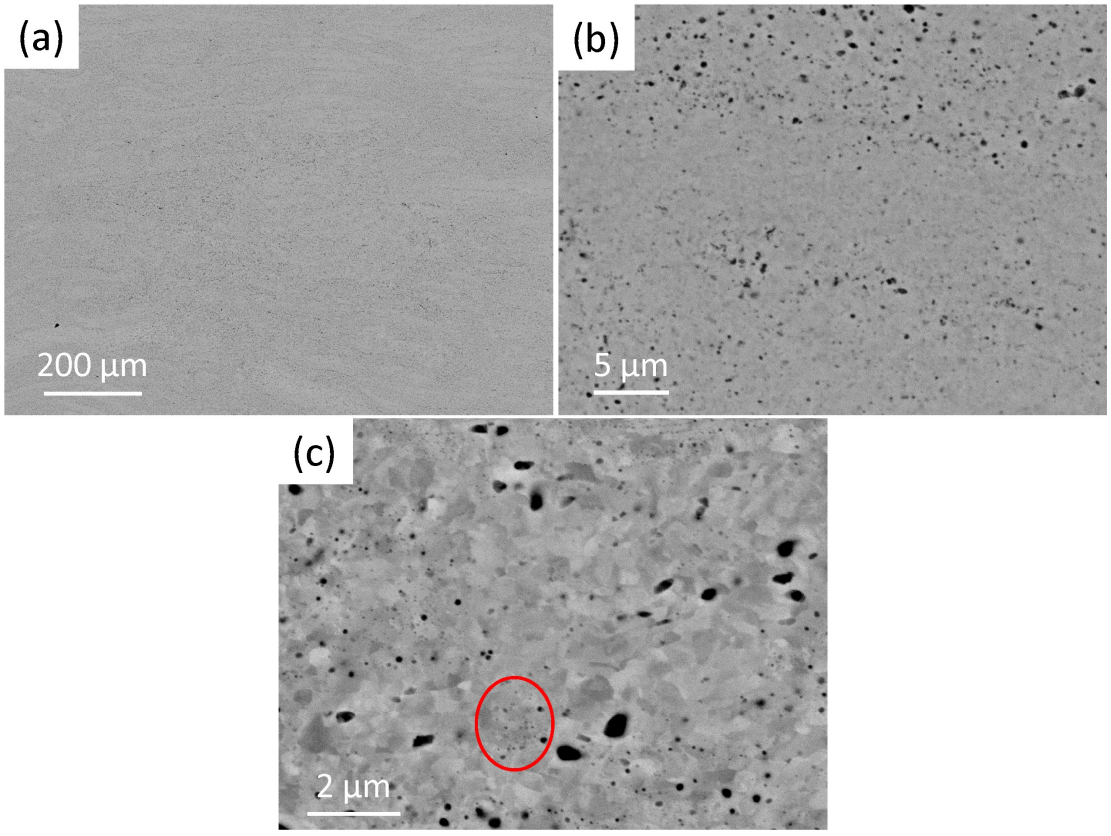

Figure 7.12: BSE SEM micrographs of alloy BA03, showing (a) residual layered structure, (b) variations in particle number density among different layers, and (c) possible regions containing the evolution of particles < 20 nm (red circle).

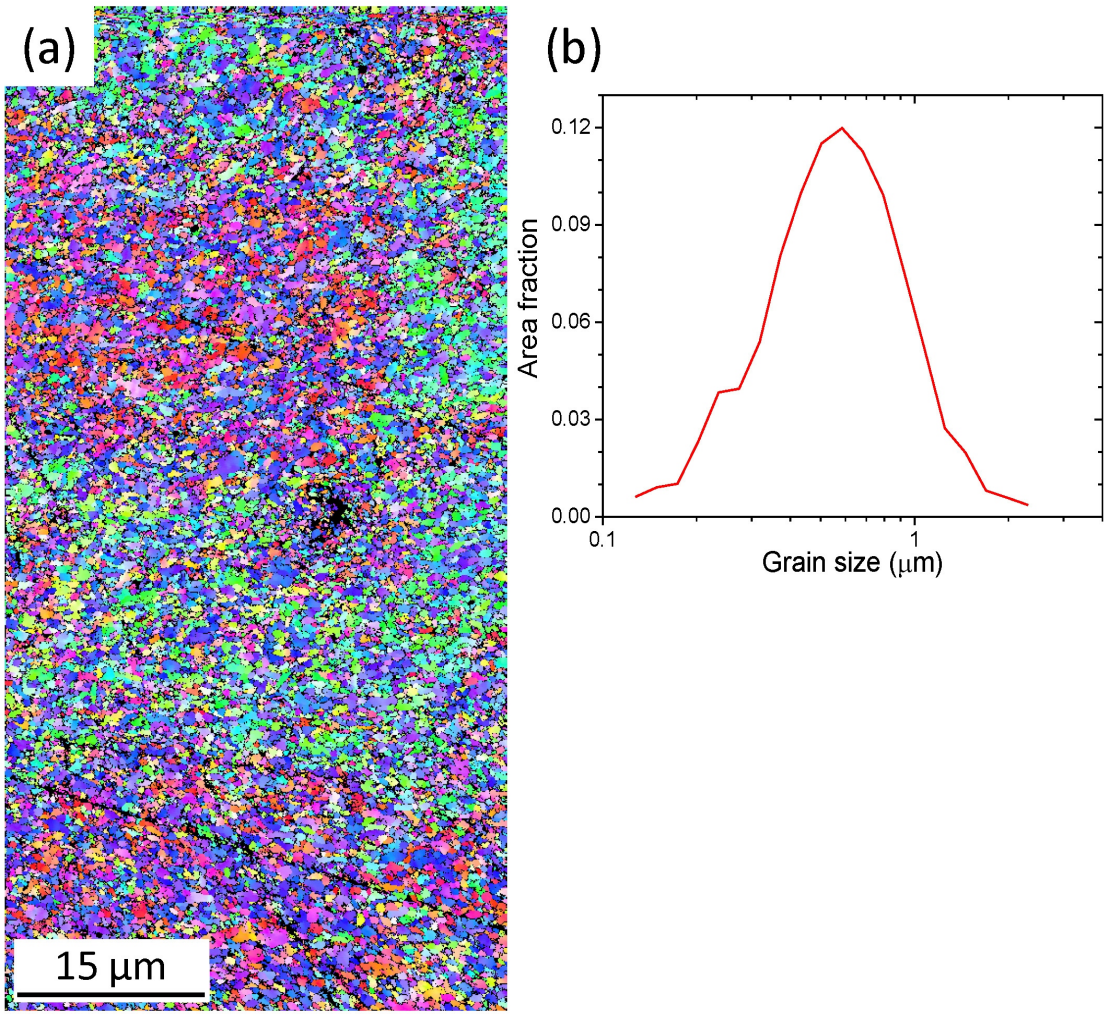

Figure 7.13: (a) EBSD IPF map showing the grains and their orientation in consolidated and annealed alloy BA03. The grain size distribution from (a), assuming spheroidal grains, is plotted in (b).

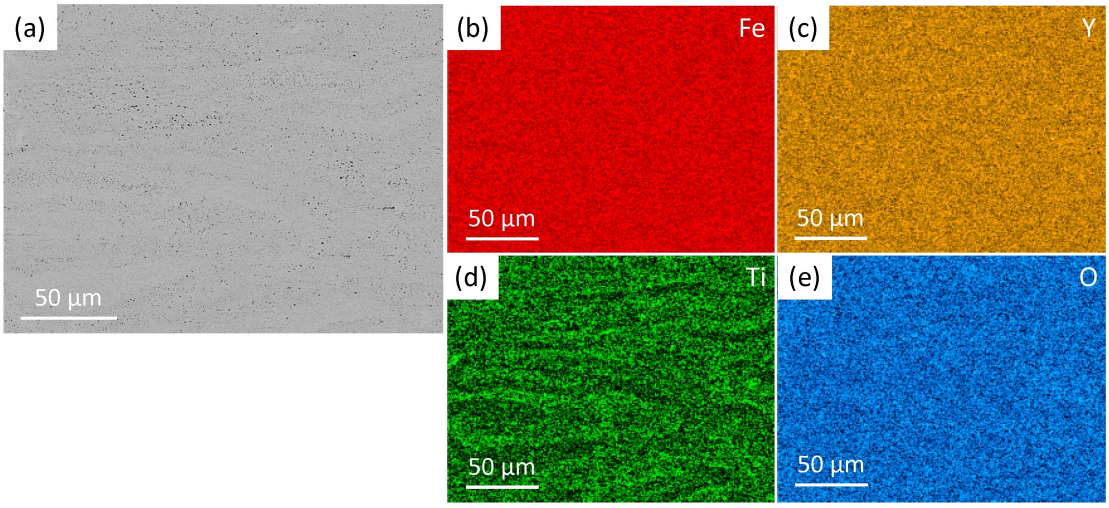

Figure 7.14: SEM characterisation of alloy BA03: (a) BSE SEM micrograph with corresponding EDX elemental maps of (b) Fe, (c) Y, (d) Ti and (e) O.

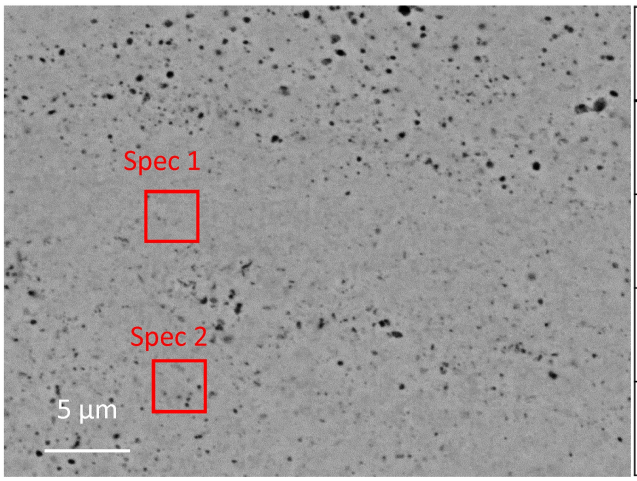

	Spec 1	Spec 2
Fe	98.0 ± 0.3	97.0 ± 0.3
Y	0.7 ± 0.2	0.8 ± 0.2
Ti	0.6 ± 0.1	1.2 ± 0.1
O	0.7 ± 0.2	1.0 ± 0.3

Figure 7.15: BSE SEM micrograph of alloy BA03 including regions of relatively low and high particle number density. EDX area measurements were conducted in the red rectangles with corresponding Fe, Y, Ti and O concentrations summarised on the right.

7.5 Hot microhardness

Hot microhardness tests were carried out on alloys BA01, BA02 and BA03 at temperatures ranging from room temperature to 500 °C, in < 1 x 10^{-4} mbar vacuum.

As shown in Figure 7.16, BA01 demonstrated the highest hardness over the range, despite containing less well developed and lower number density of sub-micron oxides, when compared with BA02 and BA03. It suggested that this higher hardness resulted from a noticeably denser consolidation and probably more mechanically coherent prior ribbon boundaries, particularly at temperatures above 400 °C, where advantage of BA01 further widened. In other words, the addition of nano-sized Fe_3O_4 particles that promote oxide formation can lead to porosity and weaker prior ribbon boundaries if consolidation parameters are not re-optimised. These pores and weak boundaries can dominate mechanical behaviour, outweighing the benefits of oxide formation – at least in hardness testing. In addition, the sub-micron Fe-Y intermetallic particles in BA01 may have also provided precipitation strengthening and contributed towards the higher hardness values measured under vacuum, although such strengthening may be less stable under a more realistic O containing environment.

Figure 7.16 also shows that the overall effect of annealing the as-consolidated BA02 was an approximately 20% increase in hardness of BA03 at temperatures below 300 °C, despite its substantially larger grain size. This may support the earlier suggestion that annealing helps complete the reactions between Y, Ti and O, and formation of the dispersion strengthening nano-sized particles. The hardness advantage of alloy BA03 disappeared at temperatures above 400 °C, which is consistent with the suggestion that porosity and weak prior ribbon boundaries can be the dominant factors in mechanical behaviour at relatively high temperatures.

Overall, the microhardness tests supported the previous suggestion that annealing can be useful to complete internal oxidation reactions. However, the adverse impact of porosity and prior ribbon boundaries on hardness was emphasised, particularly at temperatures above 400 °C.

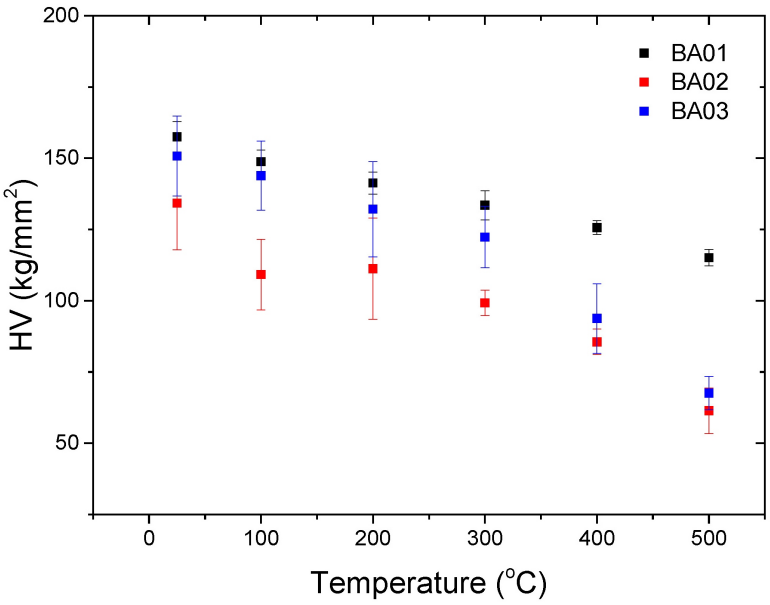

Figure 7.16 Microhardness of alloy BA01, BA02 and BA03 from room temperature (25 °C) to 500 °C.

7.6 Summary

Consolidated alloy billets were produced from the optimised MS04 ribbons. Microstructural analyses suggest that near theoretical density billets could be produced by FAST from the pulverised melt spun ribbons. With addition of the nano-sized Fe_3O_4 powder, simultaneous consolidation and internal oxidation during sintering was demonstrated, which successfully generated a high number density of sub-micron Y and/or Ti enriched oxides. Further formation of oxide particles took place during annealing, and led to an approximate 20% increase in hardness at temperatures below 300 °C.

However, introduction of the Fe_3O_4 powder reduced the sinterability of the melt spun ribbons and undermined the density of the alloy, although the precise mechanism was not identified. Restricted density and the tendency for mechanically incoherent prior ribbon boundaries due to preferred oxide formation became the predominant factors on hardness with increasing temperatures, eventually leading to a significant property drop above 400 °C.

In order to extract optimal performance from the internal oxidised alloys, the porosity identified should be eliminated by re-optimised sintering parameters. The application of a prior thermomechanical treatment of the ribbons that is more effective in inhibiting and/or breaking up surface oxides should be explored. This would aid further homogenization of particle number density distribution in the consolidated alloys.

Overall, the production of alloys BA01, BA02 and BA03 confirmed the potential of the melt spinning/FAST/internal oxidation approach for ODS steel processing.

8 Conclusions and future work

ODS steels reinforced by Y, Ti and O enriched NPs have been considered as one of the leading structural materials candidates for Generation IV fission and future fusion reactors, due to their desirable property combination of both high energy neutron irradiation resistance and high temperature mechanical properties.

Although conventional MA-based manufacturing of ODS steels has proved to be effective in generating the strengthening and stabilising NPs with desirable high number density and acceptable uniformity, problems such as prolonged processing time and scale-up limitations still remain.

This thesis has explored two alternative processing routes for the manufacture of ODS steels. In the first approach, the conventional Y source, Y_2O_3, was replaced by Fe_3Y in MA. The resulting powder and consolidated bulk materials were investigated by microstructural, microhardness, and mechanical characterisation. In the second approach, MA was replaced by melt spinning of Fe-5Y and Fe-1Y-1Ti alloys. The melt spun ribbons were investigated by microstructural analyses both in the as-spun and internal oxidised states. A Fe-1Y-1Ti ribbon was then consolidated into bulk with simultaneous internal oxidations of Y and Ti. The resulting material was studied by microstructural and microhardness investigations both in the as-consolidated and annealed states.

The main conclusions drawn from the current research are summarised as below.

8.1 Mechanical alloying based processing

During MA, the Fe_3Y containing 14YWTa and Y_2O_3 containing 14YWT powders demonstrated broadly similar evolutions of particle size distribution, microhardness, crystallite size, lattice strain and element distribution. Major differences between 14YWTa and 14YWT were only resolved at early stages of milling (< 4h), which were likely contributed by the initial size differences between the mm-sized Fe_3Y chips and

nm-sized Y_2O_3 powder. With increasing milling time, the microstructures of the two powders quickly converged, with both powders approaching steady-state conditions after 30h milling. Any enduring and small differences between the two powders towards the end of the milling (60h) may result from the likely easier refinement and dissolution of Fe_3Y compared with the much harder and more stable Y_2O_3.

After consolidation, the 14YWTa steel demonstrated a narrower grain size distribution compared with the 14YWT steel, although both steels had similar average grain sizes of approximately 5.5 μm. This result suggested a more uniform distribution of the stabilizing Y-Ti-O enriched NPs in 14YWTa, which may result from a better dispersion of Y originating from Fe_3Y than from Y_2O_3. This then likely supported the 14YWTa steel having an approximately 20% higher room temperature ductility without obvious compromise on strength, as well as slightly higher microhardness above 500 °C compared with 14YWT.

The Fe_3Y intermetallic proved to be at least as good as, or slightly better than, Y_2O_3 in terms of providing a Y source that precipitates and reacts to form Y-rich oxides during consolidation. The mm-sized Fe_3Y chips also represent a much less demanding requirement on raw material size and morphology compared with the nm-sized Y_2O_3 powder. Hence, Fe_3Y could be a replacement candidate for future development of ODS steels.

8.2 Melt spun ribbon production

Melt spun ribbons were produced using master alloys with model compositions of Fe-5Y and Fe-1Y-1Ti (wt%), and achieved relatively uniform spatial distributions of Y and Ti in an Fe matrix. The melt spinning process demonstrated good scalability (from approximately 10 g to above 100 g feedstock capacity) and repeatability across equipment in three different institutions. The yield of master alloy to ribbon, by weight, was consistently above 60%, and the melt ejection times were typically less than 10 s,

showing potential of achieving significantly higher throughput compared with conventional MA.

Internal oxidation of an Fe-5Y ribbon validated the potential for forming a dense population of < 20 nm Y oxides, while annealing of a Y depleted, Ti containing ribbon indicated formation of nano-sized Fe_2Ti particles. It was speculated that these may then transform/nucleate Y-Ti-O NPs, and may explain NP-refining action of Ti reported in MA alloys of this type.

The quality of the as-spun ribbon was heavily dependent on the quality of the master alloy, and issues, including loss and oxidation of Y, were largely resolved by using arc melting and less reactive Fe-Y intermetallic in the feedstock materials. An Fe-1Y-1Ti ribbon with satisfactory microstructure and useful quantity (~ 90 g) was successfully produced for subsequent consolidation studies.

8.3 Bulk alloy production from melt spun ribbon

FAST consolidation of the Fe-1Y-1Ti ribbon demonstrated that near theoretical density billets could be produced from pulverised melt spun ribbons. With addition of the Fe_3O_4 powder as a sacrificial O source, simultaneous consolidation and internal oxidation during sintering was achieved, which successfully generated high number density of sub-micron Y and/or Ti enriched oxides. Further formation of oxide particles took place during annealing, and led to an approximate 20% increase in hardness at temperatures below 300 °C.

However, introduction of the Fe_3O_4 powder reduced sinterability of the melt spun ribbons and undermined density of the consolidated alloys. Restricted density and the tendency for mechanically incoherent prior ribbon boundaries due to preferred oxide formation became the predominant factors on hardness with increasing temperatures, eventually leading to a significant property drop above 400 °C.

Overall, the production of bulk Fe-1Y-1Ti alloy from melt spun ribbon confirmed the potential of the melt spinning/FAST/internal oxidation approach for ODS steel manufacturing.

8.4 Future work

This work explored and advanced understanding of both the reactive MA and melt spinning-based alternative processing routes for the manufacture of ODS steels, and has shown some additional potentially beneficial lines for future enquiry. In particular, additional studies should explore in a more quantified manner the relationship between the properties and any benefits of ease or speed of production. Some of the ideas are described below.

- Further assessment of mechanical properties, particularly creep properties of the 14YWTa steel in comparison with 14YWT to understand any advantages of a narrower grain size distribution.
- Microstructural characterisation of the Y-Ti-O enriched nano-sized particles in ODS steels produced by both alternative processes using TEM and/or APT. Any variations in number density, phase and composition compared with particles in the conventional ODS steels could then be correlated to any property differences.
- Melt spinning of a master alloy with < 0.5 wt% Y and Ti concentrations, as well as additions of other common alloying elements for ODS steels such as Cr and W, should be explored so that alloys with more realistic compositions could be investigated.
- Re-optimisation of the FAST sintering parameters in the presence of a sacrificial O source (e.g. Fe_3O_4 powder), with the aim of reducing porosity and increasing homogeneity of particle number densities in the consolidated alloys.

- Exploration of thermomechanical treatment capable of inhibiting and/or breaking up of ribbon surface oxides before sintering or closing up porosity after sintering to enhance the relatively weak prior ribbon boundaries.

9 Bibliography

1. U.S. Energy Information Administration. International energy outlook 2016. (2016).

2. Zinkle, S. J. & Was, G. S. Materials challenges in nuclear energy. *Acta Mater.* **61,** 735–758 (2013).

3. International Atomic Energy Agency. *Nuclear power reactors in the world*. (IAEA, 2016).

4. Zinkle, S. J. & Busby, J. T. Structural materials for fission & fusion energy. *Mater. Today* **12,** 12–19 (2009).

5. Smith, D. L., Billone, M. C., Majumdar, S., Mattas, R. F. & Sze, D.-K. Materials integration issues for high performance fusion power systems. *J. Nucl. Mater.* **258–263,** 65–73 (1998).

6. Ohtsuka, S., Ukai, S., Fujiwara, M., Kaito, T. & Narita, T. Nano-structure control in ODS martensitic steels by means of selecting titanium and oxygen contents. *J. Phys. Chem. Solids* **66,** 571–575 (2005).

7. Odette, G. R., Alinger, M. J. & Wirth, B. D. Recent developments in irradiation-resistant steels. *Annu. Rev. Mater. Res.* **38,** 471–503 (2008).

8. Ukai, S., Nishida, T., Okuda, T. & Yoshitake, T. R&D of oxide dispersion strengthened ferritic martensitic steels for FBR. *J. Nucl. Mater.* **258–263,** 1745–1749 (1998).

9. Ukai, S. & Fujiwara, M. Perspective of ODS alloys application in nuclear environments. *J. Nucl. Mater.* **307–311,** 749–757 (2002).

10. Auger, M. A., De Castro, V., Leguey, T., Munoz, A. & Pareja, R. Microstructure and mechanical behavior of ODS and non-ODS Fe-14Cr model alloys produced

by spark plasma sintering. *J. Nucl. Mater.* **436,** 68–75 (2013).

11. Zhang, H. *et al.* Processing and microstructure characterisation of oxide dispersion strengthened Fe–14Cr–0.4Ti–0.25Y2O3 ferritic steels fabricated by spark plasma sintering. *J. Nucl. Mater.* **464,** 61–68 (2015).

12. Alinger, M. J., Odette, G. R. & Hoelzer, D. T. On the role of alloy composition and processing parameters in nanocluster formation and dispersion strengthening in nanostuctured ferritic alloys. *Acta Mater.* **57,** 392–406 (2009).

13. Heintze, C. *et al.* Nanoscale characterization of ODS Fe–9%Cr model alloys compacted by spark plasma sintering. *J. Nucl. Mater.* **428,** 139–146 (2012).

14. Narita, T., Ukai, S., Ohtsuka, S. & Inoue, M. Effect of tungsten addition on microstructure and high temperature strength of 9CrODS ferritic steel. *J. Nucl. Mater.* **417,** 158–161 (2011).

15. Vijay, R. *et al.* Strengthening Mechanisms in Mechanically Milled Oxide-Dispersed Iron Powders. *Metall. Mater. Trans. A* **44,** 1611–1620 (2012).

16. Brocq, M. *et al.* Nanoscale characterization and formation mechanism of nanoclusters in an ODS steel elaborated by reactive-inspired ball-milling and annealing. *J. Nucl. Mater.* **409,** 80–85 (2011).

17. Oksiuta, Z., Lewandowska, M., Unifantowicz, P., Baluc, N. & Kurzydlowski, K. J. Influence of Y2O3 and Fe2Y additions on the formation of nano-scale oxide particles and the mechanical properties of an ODS RAF steel. *Fusion Eng. Des.* **86,** 2417–2420 (2011).

18. Suryanarayana, C. Mechanical alloying and milling. *Prog. Mater. Sci.* **46,** 1–184 (2001).

19. Suri, A. K., Krishnamurthy, N. & Batra, I. S. Materials issues in fusion reactors. *J. Phys. Conf. Ser.* **208,** 12001 (2010).

20. Wolfer, W. G. in *Comprehensive nuclear materials Volume 1* (ed. Konings, R. J. M.) 1–46 (Elsevier, 2012).

21. McClintock, D. A., Hoelzer, D. T., Sokolov, M. A. & Nanstad, R. K. Mechanical properties of neutron irradiated nanostructured ferritic alloy 14YWT. *J. Nucl. Mater.* **386–388,** 307–311 (2009).

22. Bloom, E. E. Mechanical properties of materials in fusion reactor first-wall and blanket systems. *J. Nucl. Mater.* **85–86,** 795–804 (1979).

23. Odette, G. R. *et al.* Cleavage fracture and irradiation embrittlement of fusion reactor alloys: mechanisms, multiscale models, toughness measurements and implications to structural integrity assessment. *J. Nucl. Mater.* **323,** 313–340 (2003).

24. Maziasz, P. Formation and stability of radiation-induced phases in neutron-irradiated austenitic and ferritic steels. *J. Nucl. Mater.* **169,** 95–115 (1989).

25. Garner, F. A., Toloczko, M. B. & Sencer, B. H. Comparison of swelling and irradiation creep behavior of fcc-austenitic and bcc-ferritic/martensitic alloys at high neutron exposure. *J. Nucl. Mater.* **276,** 123–142 (2000).

26. Zinkle, S. F. in *Comprehensive nuclear materials Volume 1* (ed. Konings, R. J. M.) 65–99 (Elsevier, 2012).

27. Bloom, E. E., Zinkle, S. J. & Wiffen, F. W. Materials to deliver the promise of fusion power – progress and challenges. *J. Nucl. Mater.* **329–333,** 12–19 (2004).

28. Sublet, J.-C. & Butterworth, G. J. The neutronic basis for elemental substitution in martensitic steels. *J. Nucl. Mater.* **212–215,** 695–700 (1994).

29. Alinger, M. J. On the formation and stability of nanometer scale precipitates in ferritic alloys during processing and high temperature service. (University of California Santa Barbara, 2004).

30. Kim, I., Hunn, J. & Hashimoto, N. Defect and void evolution in oxide dispersion strengthened ferritic steels under 3.2 MeV Fe+ ion irradiation with simultaneous helium injection. *J. Nucl. Mater.* **280,** 264–274 (2000).

31. Heald, P. The preferential trapping of interstitials at dislocations. *Philos. Mag.* **31,** 551–558 (1975).

32. Ukai, S. in *Comprehensive nuclear materials Volume 4* (ed. Konings, R. J. M.) 242–270 (Elsevier, 2012).

33. McClintock, D. A., Sokolov, M. A., Hoelzer, D. T. & Nanstad, R. K. Mechanical properties of irradiated ODS-EUROFER and nanocluster strengthened 14YWT. *J. Nucl. Mater.* **392,** 353–359 (2009).

34. Smallman, R. E. & Ngan, A. H. W. *Physical metallurgy and advanced materials*. (Elsevier, 2007).

35. Bhadeshia, H. K. D. H. & Honeycombe, R. W. K. *Steels microstructure and properties*. (Elsevier, 2006).

36. Callister, W. D. *Fundamentals of materials science and engineering*. (John Wiley & Sons, Inc., 2001).

37. Meetham, G. W. & Van de Voorde, M. H. *Materials for high temperature engineering applications*. (Springer, 2000).

38. Ijiri, Y. *et al.* Consideration of the oxide particle – dislocation interaction in 9Cr-ODS steel. *Philos. Mag.* **6435,** 1–10 (2017).

39. Ijiri, Y. *et al.* Oxide particle-dislocation interaction in 9Cr-ODS steel. *Nucl. Mater. Energy* **9,** 378–382 (2016).

40. ASM International. *Powder metal technologies and applications*. (ASM International, 1998).

41. Klueh, R. L., Shingledecker, J. P., Swindeman, R. W. & Hoelzer, D. T. Oxide dispersion-strengthened steels: A comparison of some commercial and experimental alloys. *J. Nucl. Mater.* **341,** 103–114 (2005).

42. Soni, P. R. *Mechanical alloying fundamentals and applications*. (Cambridge International Science Publishing, 2001).

43. Lindau, R. *et al.* Present development status of EUROFER and ODS-EUROFER for application in blanket concepts. *Fusion Eng. Des.* **75–79,** 989–996 (2005).

44. Klueh, R., Maziasz, P. & Kim, I. Tensile and creep properties of an oxide dispersion-strengthened ferritic steel. *J. Nucl. Mater.* **311,** 773–777 (2002).

45. Miller, M. K., Hoelzer, D. T., Kenik, E. A. & Russell, K. F. Stability of ferritic MA/ODS alloys at high temperatures. *Intermetallics* **13,** 387–392 (2005).

46. Larson, D., Maziasz, P., Kim, I. & Miyahara, K. Three-dimensional atom probe observation of nanoscale titanium-oxygen clustering in an oxide-dispersion-strengthened Fe-12Cr-3W-0.4 Ti+ Y2O3 ferritic alloy. *Scr. Mater.* **44,** 359–364 (2001).

47. Ohtsuka, S., Ukai, S., Fujiwara, M., Kaito, T. & Narita, T. Improvement of 9Cr-ODS martensitic steel properties by controlling excess oxygen and titanium contents. *J. Nucl. Mater.* **329–333,** 372–376 (2004).

48. Williams, C. A., Marquis, E. A., Cerezo, A. & Smith, G. D. W. Nanoscale characterisation of ODS–Eurofer 97 steel: An atom-probe tomography study. *J. Nucl. Mater.* **400,** 37–45 (2010).

49. Ehrlich, K. & Hishinuma, A. low activation ferritic and martensitic steels for fusion application. *J. Nucl. Mater.* **233–237,** 138–147 (1996).

50. Matijasevic, M. & Almazouzi, a. Effect of Cr on the mechanical properties and

microstructure of Fe–Cr model alloys after n-irradiation. *J. Nucl. Mater.* **377,** 147–154 (2008).

51. Miyahara, K., Kobayashi, Y. & Hosoi, Y. Effects of W and Mn on the mechanical properties, microstructure and aging behaviors of 10% Cr ferritic steels considered as reduced radio-activation materials. *J. Nucl. Mater.* **179–181,** 667–670 (1991).

52. Sakasegawa, H. *et al.* Correlation between chemical composition and size of very small oxide particles in the MA957 ODS ferritic alloy. *J. Nucl. Mater.* **384,** 115–118 (2009).

53. Williams, C. A., Unifantowicz, P., Baluc, N., Smith, G. D. W. & Marquis, E. A. The formation and evolution of oxide particles in oxide-dispersion-strengthened ferritic steels during processing. *Acta Mater.* **61,** 2219–2235 (2013).

54. Ukai, S. *et al.* Characterization of High Temperature Creep Properties in Recrystallized 12Cr-ODS Ferritic Steel Claddings. *J. Nucl. Sci. Technol.* **39,** 872–879 (2002).

55. Laurent-Brocq, M. *et al.* Influence of ball-milling and annealing conditions on nanocluster characteristics in oxide dispersion strengthened steels. *Acta Mater.* **60,** 7150–7159 (2012).

56. Sakasegawa, H. *et al.* Stability of non-stoichiometric clusters in the MA957 ODS ferrtic alloy. *J. Nucl. Mater.* **417,** 229–232 (2011).

57. Alinger, M. J., Odette, G. R. & Lucas, G. E. Tensile and fracture toughness properties of MA957: implications to the development of nanocomposited ferritic alloys. *J. Nucl. Mater.* **307–311,** 484–489 (2002).

58. Sakasegawa, H. *et al.* Precipitation behavior of oxide particles in mechanically alloyed powder of oxide-dispersion-strengthened steel. *J. Alloys Compd.* **452,**

2–6 (2008).

59. Karak, S. K., Chudoba, T., Witczak, Z., Lojkowski, W. & Manna, I. Development of ultra high strength nano-Y2O3 dispersed ferritic steel by mechanical alloying and hot isostatic pressing. *Mater. Sci. Eng. A* **528,** 7475–7483 (2011).

60. Nagorka, M. S., Levi, C. G. & Lucas, G. E. Novel oxide-dispersion-strengthened copper alloys from rapidly solidified precursors: Part 1. Microstructural development. *Metall. Mater. Trans. A* **26A,** 860–871 (1995).

61. Nagorka, M. S., Levi, C. G., Lucas, G. E. & Ridder, S. D. The potential of rapid solidification in oxide-dispersion-strengthened copper alloy development. *Mater. Sci. Eng. A* **142,** 277–289 (1991).

62. Gorley, M. J. Powder processing of oxide dispersion strengthened alloys for nuclear applications. (University of Oxford, 2014).

63. Zhang, B. W., Liu, G. & Han, K. The Fe-Y (iron-yttrium) system. *J. Phase Equilibria* **13,** 304–308 (1992).

64. Benjamin, J. Dispersion strengthened superalloys by mechanical alloying. *Metall. Trans.* **1,** 2943–2951 (1970).

65. Suryanarayana, C., Ivanov, E. & Boldyrev, V. . The science and technology of mechanical alloying. *Mater. Sci. Eng. A* **304–306,** 151–158 (2001).

66. Ramar, a., Oksiuta, Z., Baluc, N. & Schäublin, R. Effect of mechanical alloying on the mechanical and microstructural properties of ODS EUROFER 97. *Fusion Eng. Des.* **82,** 2543–2549 (2007).

67. Iwata, N. Y. *et al.* Characterization of mechanically alloyed powders for high-Cr oxide dispersion strengthened ferritic steel. *ISIJ Int.* **49,** 1914–1919 (2009).

68. Reed, S. J. B. *Electron microprobe microanalysis*. (Cambridge University Press,

1993).

69. Ohtsuka, S., Ukai, S. & Fujiwara, M. Nano-mesoscopic structural control in 9CrODS ferritic/martensitic steels. *J. Nucl. Mater.* **351,** 241–246 (2006).

70. Yamada, K. & Koch, C. C. The influence of mill energy and temperature on the structure of the TiNi intermetallic after mechanical attrition. *J. Mater. Res.* **8,** 1317–1326 (2011).

71. Klimenkov, M. Quantitative measurement of argon inside of nano-sized bubbles in ODS steels. *J. Nucl. Mater.* **411,** 160–162 (2011).

72. Toualbi, L., Ratti, M., André, G., Onimus, F. & de Carlan, Y. Use of neutron and X-ray diffraction to study the precipitation mechanisms of oxides in ODS materials. *J. Nucl. Mater.* **417,** 225–228 (2011).

73. Zhang, H. *et al.* An in situ powder neutron diffraction study of nano-precipitate formation during processing of oxide-dispersion-strengthened ferritic steels. *J. Alloys Compd.* **582,** 769–773 (2014).

74. Brocq, M. *et al.* Nanoscale characterisation and clustering mechanism in an Fe–Y2O3 model ODS alloy processed by reactive ball milling and annealing. *Acta Mater.* **58,** 1806–1814 (2010).

75. Legendre, F., Poissonnet, S. & Bonnaillie, P. Synthesis of nanostructured SnO2 materials by reactive ball-milling. *J. Alloys Compd.* **434–435,** 400–404 (2007).

76. Lorrain, N., Chaffron, L., Carry, C., Delcroix, P. & Caër, G. L. Kinetics and formation mechanisms of the nanocomposite powder Ag–SnO2 prepared by reactive milling. *Mater. Sci. Eng. A* **367,** 1–8 (2004).

77. McCormick, P. Application of mechanical alloying to chemical refining (Overview). *Mater. Trans.* **36,** 161–169(1995).

78. McCormick, P., Wharton, V. & Schaffer, G. *Physical Chemistry of Powder Metals Production and Processing*. (TMS, 1989).

79. Wen, Y. *et al.* Innovative processing of high-strength and low-cost ferritic steels strengthened by Y–Ti–O nanoclusters. *Mater. Sci. Eng. A* **544,** 59–69 (2012).

80. Hoelzer, D. T. *et al.* Influence of particle dispersions on the high-temperature strength of ferritic alloys. *J. Nucl. Mater.* **367–370,** 166–172 (2007).

81. Rajiv Asthana, Ashok Kumar, N. B. D. *Materials processing and manufacturing science*. (Academic Press, 2006).

82. Liebermann, H. H. Rapidly solidified alloys made by chill block melt-spinning processes. *J. Cryst. Growth* **70,** 497–506 (1984).

83. Chen, H., Leamy, H. & Miller, C. Preparation of glassy metals. *Annu. Rev. Mater.* **10,** 363–392 (1980).

84. Douglass, D. L. Anomalous Behaviour during Internal oxidation and Nitridation. *JOM-JOURNAL Miner. Met. Mater. Soc.* **43,** 74–79 (1991).

85. Rhines, F. N. A metallographic study of internal oxidation in the alpha solid solutions of copper. *Trans. AIME* **137,** 246–289 (1940).

86. Combe, A. & Cabane, J. Mechanism of internal oxidation in silver alloys. *Oxid. Met.* **21,** 21–37 (1984).

87. Troxell, J. GlidCop dispersion strengthened copper, potential application in fusion power generators. *IEEE Thirteen. Symp. Fusion Eng.* **2,** 761–764 (1989).

88. Schneibel, J. H. & Shim, S. Nano-scale oxide dispersoids by internal oxidation of Fe–Ti–Y intermetallics. *Mater. Sci. Eng. A* **488,** 134–138 (2008).

89. Nagorka, M. S., Levi, C. G., Lucas, G. E. & Ridder, S. D. The potential of rapid solidification in oxide-dispersion-strengthened copper alloy development. *Mater.*

Sci. **142,** 277–289 (1991).

90. de Carlan, Y. *et al.* CEA developments of new ferritic ODS alloys for nuclear applications. *J. Nucl. Mater.* **386–388,** 430–432 (2009).

91. Hoffmann, J. Ferritische ODS-Stahle-Herstellung, Umformung und Struktur analyse. (Karlsruher Institut fur Technologie (KIT), 2013).

92. Cunningham, N. J. *et al.* Effect of bulk oxygen on 14YWT nanostructured ferritic alloys. *J. Nucl. Mater.* **444,** 35–38 (2014).

93. Krauss, G. *Steels: heat treatment and processing principles*. (ASM International, 2001).

94. ASM International. *ASM handbook, Volume 3, Alloy phase diagram*. (ASM International, 1992).

95. Sakasegawa, H. *et al.* Report of IEA workshop on reduced activation ferritic/martensitic steels. in *JAERI-Conference* 494

96. Kim, S.-B., Paik, K.-W. & Kim, Y.-G. Effect of Mo substitution by W on high temperature embrittlement characteristics in duplex stainless steels. *Mater. Sci. Eng. A* **247,** 67–74 (1998).

97. Ukai, S. *et al.* Alloying design of oxide dispersion for long life FBRs core materials strengthened ferritic steel. *J. Nucl. Mater.* **204,** 5–73 (1993).

98. Klimiankou, M., Lindau, R. & Moslang, A. TEM characterization of structure and composition of nanosized ODS particles in reduced activation ferritic-martensitic steels. *J. Nucl. Mater.* **329–333,** 347–351 (2004).

99. Klimiankou, M., Lindau, R. & Moslang, A. Energy-filtered TEM imaging and EELS study of ODS particles and Argon-filled cavities in ferritic-martensitic steels. *Micron* **36,** 1–8 (2005).

100. Ohnuma, M. *et al.* A new method for the quantitative analysis of the scale and composition of nanosized oxide in 9Cr-ODS steel. *Acta Mater.* **57,** 5571–5581 (2009).

101. Aubert & Duval. *Inspection certificate*. (2011).

102. Fritsch GmbH. Operating manual planetary mill pulverisette 5 classic line. (2011).

103. Acton Bight Steels Ltd. Inspection certificate. (2011).

104. Nagorka, M., Lucas, G. & Levi, C. Novel oxide-dispersion-strengthened copper alloys from rapidly solidified precursors: Part 2. Creep behavior. *Metall. Mater. Trans. A* (1995).

105. Rhines, F. N., Johnson, W. A. & Anderson, W. A. Rates of High-Temperature Oxidation of Dilute Copper Alloys. *Trans. AIME* **147,** 205–221 (1942).

106. Goldstein, J. *et al. Scanning electron microscopy and X-ray microanalysis*. (Springer, 2003).

107. Friel, J. J. *X-ray and image analysis in electron microscopy*. (Princton Gamma-Tech, 1995).

108. Hwang, J.-Y. *et al. Characterization of Minerals, Metals and Materials*. (John Wiley & Sons, Inc., 2012).

109. Williams, D. B. & Carter, C. B. *Transmission electron microscopy: a textbook for materials science*. (Springer, 2009).

110. Reimer, L. *Transmission electron microscopy: physics of image formation and microanalysis*. (Springer, 1997).

111. Klinger, M. & Jäger, A. Crystallographic Tool Box (CrysTBox): Automated tools for transmission electron microscopists and crystallographers. *J. Appl.*

Crystallogr. **48,** 2012–2018 (2015).

112. Lutterotti, L. Total pattern fitting for the combined size-strain-stress-texture determination in thin film diffraction. *Nucl. Instruments Methods Phys. Res. Sect. B Beam Interact. with Mater. Atoms* **268,** 334–340 (2010).

113. Hergert, W. & Wriedt, T. *The Mie theory: basics and applications*. (Springer, 2012).

114. Malvern instruments Ltd. Mastersizer 2000 user manual. (2007).

115. Chandler, H. *Hardness testing*. (ASM International, 1999).

116. Hammant, B. The use of 4-point loading tests to determine mechanical properties. *Composites* **2,** 246–249 (1971).

117. Gilman, P. S. & Benjamin, J. S. Mechanical alloying. 279–300 (1998).

118. Xu, H., Lu, Z., Wang, D. & Liu, C. Microstructural evolution in a new Fe based ODS alloy processed by mechanical alloying. *Nucl. Mater. Energy* **7,** 1–4 (2016).

119. Sallez, N. *et al.* On ball-milled ODS ferritic steel recrystallization: From as-milled powder particles to consolidated state. *J. Mater. Sci.* **50,** 2202–2217 (2015).

120. Balzar, D. *et al.* Size-strain line-broadening analysis of the ceria round-robin sample. *J. Appl. Crystallogr.* **37,** 911–924 (2004).

121. Langford, J. I. & Wilson, A. J. C. Scherrer after sixty years: A survey and some new results in the determination of crystallite size. *J. Appl. Crystallogr.* **11,** 102–113 (1978).

122. Hilger, I., Bergner, F. & Weissgarber, T. Bimodal grain size distribution of nanostructured ferritic ODS Fe-Cr alloys. *J. Am. Ceram. Soc.* **98,** 3576–3581 (2015).

123. Boulnat, X., Fabregue, D., Perez, M., Mathon, M. H. & De Carlan, Y. High-

temperature tensile properties of nano-oxide dispersion strengthened ferritic steels produced by mechanical alloying and spark plasma sintering. *Metall. Mater. Trans. A Phys. Metall. Mater. Sci.* **44,** 2461–2465 (2013).

124. Boulnat, X. *et al.* Microstructure evolution in nano-reinforced ferritic steel processed by mechanical alloying and spark plasma sintering. *Metall. Mater. Trans. A Phys. Metall. Mater. Sci.* **45,** 1485–1497 (2014).

125. Eiselt, C. C. *et al.* High-resolution transmission electron microscopy and electron backscatter diffraction in nanoscaled ferritic and ferritic-martensitic oxide dispersion strengthened-steels. *J. Nucl. Mater.* **385,** 231–235 (2009).

126. Wang, X. L. *et al.* Unusual thermal stability of nano-structured ferritic alloys. *J. Alloys Compd.* **529,** 96–101 (2012).

127. Hilger, I. *et al.* The structural changes of Y2O3 in ferritic ODS alloys during milling. *J. Nucl. Mater.* **447,** 242–247 (2014).

128. McFadden, S. X., Zhilyaev, A. P., Mishra, R. S. & Mukherjee, A. K. Observations of low-temperature superplasticity in electrodeposited ultrafine grained nickel. *Mater. Lett.* **45,** 345–349 (2000).

129. Patra, S., Hasan, S. M., Narasaiah, N. & Chakrabarti, D. Effect of bimodal distribution in ferrite grain sizes on the tensile properties of low-carbon steels. *Mater. Sci. Eng. A* **538,** 145–155 (2012).

130. Wang, Y. M. & Ma, E. Three strategies to achieve uniform tensile deformation in a nanostructured metal. *Acta Mater.* **52,** 1699–1709 (2004).

131. Garcia-Junceda, A., Campos, M., Garcia-Rodriguez, N. & Torralba, J. M. On the role of alloy composition and sintering parameters in the bimodal grain size distribution and mechanical properties of ODS ferritic steels. *Metall. Mater. Trans. A* **47,** 5325–5333 (2016).

132. Koch, C. C. Optimization of strength and ductility in nanocrystalline and ultrafine grained metals. *Scr. Mater.* **49,** 657–662 (2003).

133. Wang, Y., Chen, M., Zhou, F. & Ma, E. High tensile ductility in a nanostructured metal. *Nature* **419,** 912–915 (2002).

134. Auger, M. A. *et al.* Microstructure and mechanical properties of ultrafine-grained Fe-14Cr and ODS Fe-14Cr model alloys. *J. Nucl. Mater.* **417,** 213–216 (2011).

135. Auger, M. A. *et al.* Microstructure and tensile properties of oxide dispersion strengthened Fe–14Cr–0.3Y2O3 and Fe–14Cr–2W–0.3Ti–0.3Y2O3. *J. Nucl. Mater.* **442,** S142–S147 (2013).

136. Liu, A. F. *Mechanics and mechanism of fracture: an introduction*. (ASM International, 2005).

137. Wang, Y. M. & Ma, E. Strain hardening, strain rate sensitivity, and ductility of nanostructured metals. *Mater. Sci. Eng. A* **375–377,** 46–52 (2004).

138. Oskooie, M. S. *et al.* Strength and ductility enhancement in nanostructured Al6063 with a bimodal grain size distribution. *IOP Conf. Ser. Mater. Sci. Eng.* **63,** 12022 (2014).

139. Gilmore, C. *Materials science and engineering properties*. (Timothy Anderson, 2015).

140. Abdou, M. *et al.* Blanket/first wall challenges and required R&D on the pathway to DEMO. *Fusion Eng. Des.* **100,** 2–43 (2015).

141. Malang, S., Tillack, M., Wong, C. P. C., Morley, N. & Smolentsev, S. Development of the Lead Lithium (DCLL) Blanket Concept. *Fusion Sci. Technol.* **60,** 249–256 (2011).

142. Bergner, F. *et al.* Alternative fabrication routes toward Oxide-Dispersion-

Strengthened steels and model alloys. *Metall. Mater. Trans. A Phys. Metall. Mater. Sci.* **47,** 5313–5324 (2016).

143. Ryan, P. C. *Comments from Hitachi Metals America Ltd. and Metglas Inc. regarding the ENERGY STAR transformer program*. (2015).

144. Sha, W. & Guo, Z. *Maraging steels: Modelling of microstructure, properties and applications*. (CRC Press, 2009).

145. Davis, J. R. *ASM specialty handbook: tool materials*. (ASM International, 1995).

146. Reed, T. B. *Free energy of formation of binary compounds: an atlas of charts for high temperature chemical calculations*. (MIT Press, 1972).

147. Boulnat, X. *et al.* Assessment of consolidation of oxide dispersion strengthened ferritic steels by spark plasma sintering: from laboratory scale to industrial products. *Powder Metall.* **57,** 204–211 (2014).

148. Chennoufi, N., Majkic, G., Chen, Y. C. & Salama, K. Temperature, current, and heat loss distributions in reduced electrothermal loss spark plasma sintering. *Metall. Mater. Trans. A Phys. Metall. Mater. Sci.* **40,** 2401–2409 (2009).

149. Nanko, M., Sato, M., Matsumaru, K. & Ishizaki, K. Homogeneity of porous metals prepared by pulse electric current pressure sintering. in *Novel materials processing by advanced electromagnetic energy sources* 281–284 (Elsevier Ltd, 2005).

150. Yucheng, W. & Zhengyi, F. Study of temperature field in spark plasma sintering. *Mater. Sci. Eng. B* **90,** 34–37 (2002).

151. Kim, H., Kawahara, M. & Tokita, M. Specimen Temperature and Sinterability of Ni Powder by Spark Plasma Sintering. *J. Japan Soc. powder Powder Metall.* **47,** 887–891 (2000).

152. Cayron, C., Rath, E., Chu, I. & Launois, S. Microstructural evolution of Y2O3 and MgAl2O4 ODS EUROFER steels during their elaboration by mechanical milling and hot isostatic pressing. *J. Nucl. Mater.* **335,** 83–102 (2004).

153. Sallez, N. *et al.* In situ characterization of microstructural instabilities: Recovery, recrystallization and abnormal growth in nanoreinforced steel powder. *Acta Mater.* **87,** 377–389 (2015).

154. Humphreys, F. J. & Hatherly, M. *Recrystallization and related annealing phenomena*. (Elsevier Science Ltd, 1995).